Analysis of DC-DC Converters for Integrated Photovoltaic Solar-Powered Electric Bus Charging Systems

Paula Wassão Forigo

Work oriented by:

Prof. Orlando Soares

Prof. Gerson Tiepolo

Bragança

2024-2025

Analysis of DC-DC Converters for Integrated Photovoltaic Solar-Powered Electric Bus Charging Systems

Paula Wassão Forigo

Dissertation presented to the School of Technology and Management of Bragança to obtain the Master's Degree in Renewable energy and Energy efficiency under the scope of the Double Degree agreement with Federal University of Technology - Paraná.

Bragança

2024-2025

Dedication

I dedicate this work to my family, whose unwavering love, support, and encouragement have been my foundation throughout this journey. To my parents, for instilling in me the values of perseverance and curiosity, and for always believing in my potential. To my friends and colleagues, who stood by my side, providing inspiration, motivation, and moments of joy that lightened the path. This work is also dedicated to all those who dream of pushing boundaries and contributing to a more sustainable world. May this be a small step toward that shared vision. As Walt Disney once said, "We keep moving forward, opening up new doors and doing new things, because we're curious...and curiosity keeps leading us down new paths." This dedication is a testament to that spirit of curiosity and discovery, which has guided me through every challenge and triumph along the way.

Acknowledgement

First and foremost, I extend my gratitude to my advisor, Prof. Orlando Soares, for their invaluable guidance, patience, and encouragement throughout the course of this research. Your expertise and insights have been pivotal in shaping this work, and I am deeply thankful for the opportunities to learn and grow under your mentorship. I would like to thank my committee members, for their thoughtful feedback, challenging questions, and commitment to improving the quality of this research. Your contributions have been invaluable to the refinement of this work. I am profoundly grateful to my family for their unwavering love, steadfast belief in me, and the invaluable lessons they have imparted about perseverance and the importance of education. Thank you for your patience, understanding, and for being my unwavering pillars of strength throughout this journey. This thesis is not just a culmination of my efforts but also a reflection of the collective support, wisdom, and inspiration I have received from everyone around me. To all who have been a part of this journey—thank you.

Abstract

This dissertation aims to conduct a theoretical study and corresponding validation of the feasibility of using integrated photovoltaic systems for charging electric vehicles, specifically focusing on an electric bus as the model of study. The work begins with a theoretical analysis of photovoltaic systems, selecting the most suitable solar cells for application in an electric vehicle, considering performance, technical, and physical characteristics. This study includes the development of a mathematical model of the photovoltaic cells and their numerical simulation.

Next, the design of an energy conversion system is addressed, using DC-DC converters. Different types of converters and their combinations are studied to maximize charging efficiency. The most appropriate topologies and control methods for the converters are discussed, aiming to optimize system performance.

Finally, the proposed models are validated through simulations in Matlab/Simulink software, using lithium-ion batteries as the storage system. The dissertation seeks to demonstrate how the integration of photovoltaic solar energy can serve as a complementary and eco-friendly solution for charging electric buses, contributing to sustainability in transportation.

Keywords: Photovoltaic Energy, Electric Buses, DC-DC Converters, MPPT

Resumo

Esta dissertação tem como objetivo realizar um estudo teórico e a correspondente comprovação da viabilidade de utilização de sistemas fotovoltaicos integrados para o carregamento de veículos elétricos, focando-se especificamente em um autocarro elétrico como modelo de estudo. O trabalho começa com a análise teórica de sistemas fotovoltaicos, selecionando as células solares mais adequadas para aplicação em um veículo elétrico, considerando rendimento, características técnicas e físicas. Este estudo inclui o desenvolvimento de um modelo matemático das células fotovoltaicas e sua simulação numérica.

Em seguida, aborda-se o projeto de um sistema de conversão de energia, utilizando conversores DC-DC. Diferentes tipos de conversores e suas combinações são estudados para maximizar a eficiência do carregamento. As topologias e métodos de controle mais apropriados para os conversores são discutidos, visando otimizar o desempenho do sistema.

Por fim, os modelos propostos são validados por meio de simulações no software Matlab/Simulink, utilizando baterias de íons de lítio como sistema de armazenamento. A dissertação busca demonstrar como a integração de energia solar fotovoltaica pode servir como uma solução complementar e ecológica para o carregamento de ônibus elétricos, contribuindo para a sustentabilidade no transporte.

Palavras-chave: Energia Fotovoltaica, Autocarros elétricos, Conversores DC-DC, MPPT

Contents

List of Tables

List of Figures

List of Acronyms

a-Si Amorphous Silicon.

AC Alternating Current.

BEVs Battery Electric Vehicles.

BIPV Building-Integrated Photovoltaics.

c-Si Silicon Solar Cells.

CAN Controller Area Network.

CdTe Cadmium Telluride.

CIGS Copper Indium Gallium Selenide.

D Fixed Duty Cycle.

DC Direct Current.

DSSC Dye-Sensitized Solar Cells.

EV Electric Vehicles.

GaAs Gallium Arsenide.

HEVs Hybrid Electric Vehicles.

IC Incremental Conductance.

IEC International Electrotechnical Commission.

KCL Kirchhoff's current law.

LFP Lithium Iron Phosphate.

LTO Lithium Titanate Oxide.

MPPT Maximum Power Point Tracking.

NCA Lithium Nickel Cobalt Aluminum Oxide.

NMC Lithium Nickel Manganese Cobalt.

NOCT Nominal Operating Cell Temperature.

OPV Organic Photovoltaics.

p-Si Polycrystalline Cells.

P&O Perturb and Observe.

PHEVs Plug-in Hybrid Electric Vehicles.

PV Photovoltaic.

PWM Pulse Width Modulation.

SCR Silicon Controlled Rectifier.

SoC State of Charge.

V2G Vehicle-to-Grid.

Vcte Constant Voltage.

Chapter 1

Introduction

1.1 Motivation

The global shift towards sustainable transportation solutions has led to increased interest in Electric Vehicles (EV), particularly as a means to reduce greenhouse gas emissions and dependence on fossil fuels. Among various EV applications, electric buses play a significant role in reducing the environmental impact of public transportation systems. However, one of the main challenges associated with electric buses is the need for efficient and reliable charging systems to ensure operational continuity and minimize downtime.

Photovoltaic (PV) solar energy offers a promising solution to address this challenge by providing a renewable and clean energy source for charging electric buses. Integrating PV systems into EV charging infrastructure can not only reduce operational costs but also contribute to energy independence and environmental sustainability. This thesis focuses on studying the feasibility and optimization of using integrated photovoltaic systems for charging electric buses.

The research begins with an in-depth analysis of photovoltaic technologies, selecting the most suitable solar cells for use in electric vehicles based on their efficiency, technical specifications, and physical characteristics. Additionally, it explores the design of energy

conversion systems, employing DC-DC converters to maximize the efficiency of the charging process. By analyzing various converter topologies and control strategies, this study aims to develop an efficient system for charging electric buses using solar energy.

Through the use of simulations, particularly in Matlab/Simulink, this work validates the proposed models, using lithium-ion batteries as the primary storage system. Ultimately, this research seeks to demonstrate the potential of photovoltaic solar energy as a complementary solution for electric bus charging, contributing to a more sustainable and eco-friendly public transportation network.

1.2 Objectives

The primary goal of this thesis is to explore the integration of photovoltaic solar energy as a complementary charging solution for electric buses. To achieve this, the research will focus on several key objectives. First, it aims to analyze various photovoltaic technologies to identify the most suitable solar cells for application in electric buses, taking into consideration factors such as efficiency, technical specifications, and physical characteristics. Additionally, the research seeks to design an energy conversion system using DC-DC converters, with a focus on optimizing the charging process through the selection of appropriate topologies and control strategies. Finally, the study will validate the proposed models through simulations in Matlab/Simulink, using lithium-ion batteries as the energy storage system. Ultimately, the thesis aims to demonstrate the feasibility of using photovoltaic energy to enhance the sustainability and operational efficiency of electric buses.

1.3 Structure of the Document

The thesis is organized into several chapters, each addressing different aspects of the research. The first chapter introduces the topic, outlining the motivation behind the study

and presenting the research objectives. Following this, the second chapter provides a theoretical overview of photovoltaic systems, with a detailed analysis of solar cell selection for electric vehicle applications. The third chapter focuses on the design of the energy conversion system, specifically the use of DC-DC converters and associated control strategies to improve charging efficiency. The fourth chapter presents the simulation models developed using Matlab/Simulink, validating the performance of the integrated photovoltaic charging system, with lithium-ion batteries as the storage medium. In the fifth chapter, the results of the simulations are discussed, evaluating the system's effectiveness in charging electric buses. The final chapter concludes the thesis, summarizing the main findings, discussing potential limitations, and offering recommendations for future research.

Chapter 2

State of Art

In this chapter, a brief overview of the key technologies relevant to the subject of this dissertation will be presented, consolidating their theoretical components. The technologies covered include solar energy, electric buses, electric vehicle chargers, and DC-DC converters.

2.1 Solar Energy

2.1.1 History

Solar energy, as one of the most promising sources of renewable energy, has garnered significant interest due to its abundance and sustainability. As a virtually inexhaustible natural resource, its exploration has led to substantial technological advancements in harnessing solar radiation for electricity generation through the photovoltaic effect. This phenomenon was initially discovered in 1839 by Edmond Becquerel, who observed that metal plates immersed in an electrolyte produced a small potential difference when exposed to light. However, it was not until 1883 that Charles Fritts created the first practical photovoltaic cell using selenium semiconductor coated with gold, although it had very low efficiency, below 1% [1][2].

Since then, the development of photovoltaic technology has been exponential, especially in recent decades. Advances in semiconductor materials, particularly silicon, have enabled the production of photovoltaic cells with much higher efficiencies, reaching over 22% in some commercial panels. The search for alternative materials and the development of technologies such as perovskite cells are expected to further enhance this efficiency in the future [3]. Additionally, the cost of producing photovoltaic modules has decreased significantly, making solar energy a competitive alternative to conventional energy sources such as coal and natural gas [4].

However, one of the major limitations of solar energy is its temporal intermittency and spatial variability. Solar power generation depends on local weather conditions, such as cloud cover, atmospheric gas concentrations, and synoptic systems, as well as astronomical factors like the Earth's rotation and orbit. Therefore, the potential for solar power generation is not constant throughout the day or year, which can pose challenges for the reliability of the electrical system. Detailed and accurate information about the variability and temporal behavior of solar resources is crucial for the technical viability of solar projects and for ensuring the stability and security of electrical grids that integrate this energy source [5][6].

Brazil, for instance, has emerged as one of the countries with the highest solar energy potential due to its favorable geographic location and high solar incidence throughout the year. According to the Brazilian Atlas of Solar Energy, developed by the National Institute for Space Research (INPE), almost the entire Brazilian territory receives solar radiation exceeding 4.5 kWh/m^2 per day, which is very competitive for the installation of photovoltaic systems [7]. Assessing solar resource potential involves understanding the spatial distribution of solar radiation, its temporal variability, and the associated uncertainties. This knowledge is essential for developing application scenarios and preliminary feasibility studies to maximize solar energy utilization and contribute to the sustainable development of the energy sector [8].

In addition to climatic and astronomical factors, the performance of photovoltaic systems is also subject to uncertainties related to shading losses, temperature, dirt, and

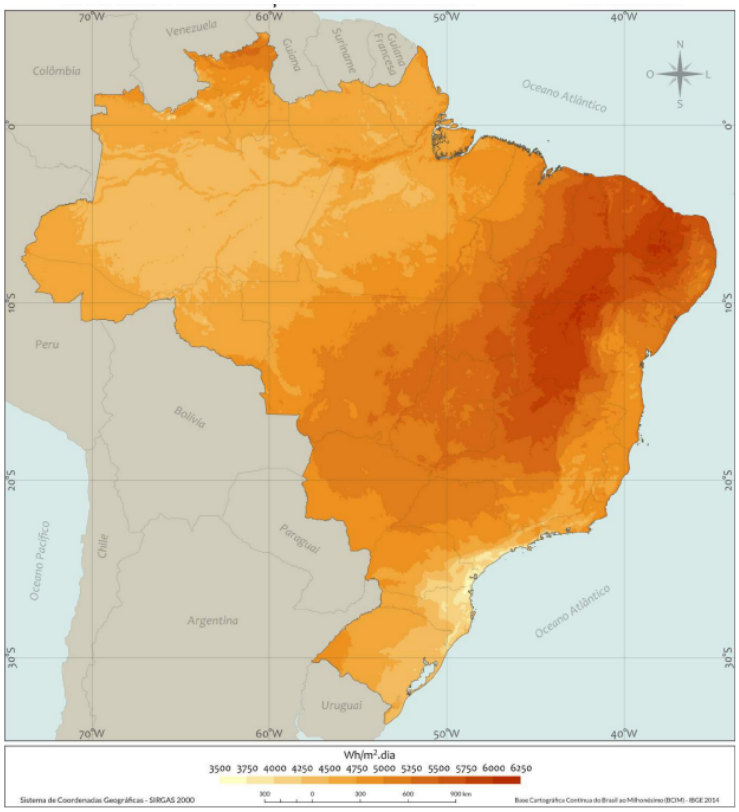

Figure 2.1: Daily Total of Horizontal Global Irradiance - Brasil
Source: [5]

module degradation over time. These uncertainties highlight the importance of conducting detailed feasibility studies and computational simulations that account for these factors to estimate the annual energy production of a photovoltaic system [9]. Technologies such as remote monitoring and string optimization systems are increasingly being implemented to mitigate these losses and improve the overall efficiency of solar systems [10].

Thus, the development of solar projects requires a careful analysis of available resources, solar potential variability, and the integration of innovative technologies to maximize the utilization of this clean and renewable energy source. Transitioning to an energy system based on renewable sources, such as solar energy, is a crucial step in reducing greenhouse gas emissions and mitigating climate change.

2.1.2 Global and Local Solar Landscape - Paraná

The state of Paraná, Brazil, has significant potential for solar energy generation, with an annual average of global horizontal irradiation of 1,705 kWh/m².yr. Within the state, irradiation extremes range from 1,365 kWh/m².yr in the municipality of Guaratuba to 1,938 kWh/m².yr in Itaguajé and Santa Inês. The state's mesoregions also show important differences, with the highest annual average found in the Northwest mesoregion at 1,802 kWh/m².yr, while the lowest is in the Curitiba Metropolitan mesoregion at 1,492 kWh/m².yr [11].

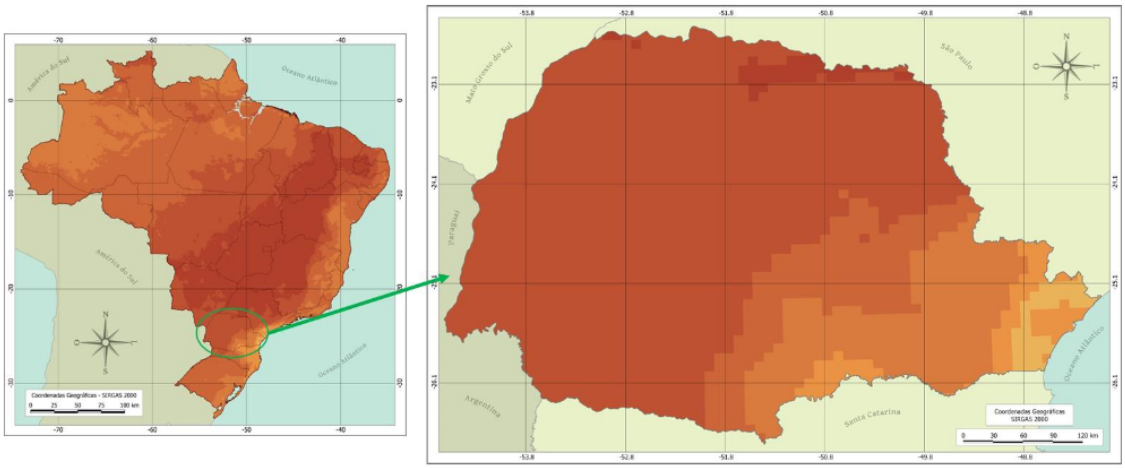

Figure 2.2: Brazilian Photovoltaic Map and Photovoltaic Map of the State of Paraná - Total Annual (Inclined Plane - HTOT)
Source: Adapted from [12]

Seasonally, Paraná experiences higher irradiation levels during the summer, with a daily average of 5.88 kWh/m².day, and lower levels in winter, averaging 3.47 kWh/m².day. These variations have a direct impact on photovoltaic productivity, especially in regions like the Northwest, where consistently high irradiation makes it ideal for large-scale solar energy projects.

When comparing Paraná's solar potential to European countries, where solar photovoltaic energy is widely adopted, the state demonstrates a notable advantage. With an average annual irradiation of 1,789 kWh/m².year and an estimated productivity of 1,342

kWh/kWp.year (considering a performance rate of 75%), Paraná surpasses most European nations. Table A.1 located in Appendix A highlights this comparison, showing that only six European countries, including Cyprus (1,663 kWh/kWp.year) and Malta (1,617 kWh/kWp.year), achieve higher productivity than Paraná.

Portugal serves as an important benchmark due to its climatic similarities and well-established solar energy policies. Although Portugal's productivity of 1,497 kWh/kWp.year is 10.38% higher than Paraná's, the state's superior irradiation highlights its significant untapped potential. By adopting strategic investments and supportive policies similar to those implemented in Portugal, Paraná could position itself as a leading player in solar energy production.

Conversely, countries like Germany, recognized globally for its solar energy leadership, demonstrate much lower irradiation and productivity. Germany's productivity, at 938 kWh/kWp.year, is 43% lower than Paraná's. This stark contrast emphasizes the potential for Paraná to excel, even when compared to regions with advanced solar infrastructure.

Overall, Paraná's solar potential is exceptional, surpassing many global benchmarks in photovoltaic energy use. With targeted investments and policy support, the state can capitalize on its favorable irradiation conditions to become a major contributor to renewable energy production.

2.1.3 Operating Principles of Photovoltaic Systems

Photovoltaic (PV) systems operate based on the photovoltaic effect, a process through which solar energy is converted directly into electrical energy. When sunlight strikes a PV cell, which is typically made of semiconductor materials like silicon, photons from the light knock electrons loose from their atoms. This movement of electrons creates an electrical current, which can then be captured and used to power electrical devices.

The efficiency of PV systems depends on several factors, including the material used in the cells, the quality of sunlight, and the angle of incidence of the sunlight on the panels. Silicon-based solar cells remain the most commonly used, due to their relatively

high efficiency and durability [13]. When photons hit the semiconductor material, they excite the electrons in the valence band, causing them to jump to the conduction band and create electron-hole pairs. These pairs are then separated by an internal electric field, generating a Direct Current (DC).

PV cells are typically organized into modules and arrays to generate higher amounts of electricity. The electrical output of a PV system is proportional to the intensity of sunlight and the area of the panel exposed to sunlight. In large-scale applications, such as solar farms or integrated rooftop systems, this ability to scale allows PV systems to meet substantial portions of energy demand. However, the intermittency of solar energy due to weather conditions and the day-night cycle remains a challenge. This is where the integration of energy storage systems, such as lithium-ion batteries, becomes essential, as they store excess energy produced during peak sunlight hours for use when sunlight is unavailable [14].

2.1.4 Photovoltaic Technologies

Photovoltaic (PV) technologies can be broadly categorized into three generations, each representing different materials, designs, and levels of efficiency. These generations reflect the evolution of solar technology, with improvements in efficiency, cost-effectiveness, and application flexibility.

Currently, there are numerous photovoltaic technologies under development, some of which hold great promise for revolutionizing the price-to-efficiency ratio. Broadly speaking, the existing technologies can be classified into three categories, known as generations, as illustrated in figure 2.3.

- First-Generation: Silicon Solar Cells (c-Si) is based on crystalline silicon solar cells, which remain the most widely used and commercially available. These cells are predominantly made from either monocrystalline or polycrystalline silicon. Monocrystalline cells are known for their higher efficiency, as they are made from a single,

Figure 2.3: Diagram of the main existing photovoltaic cell technologies

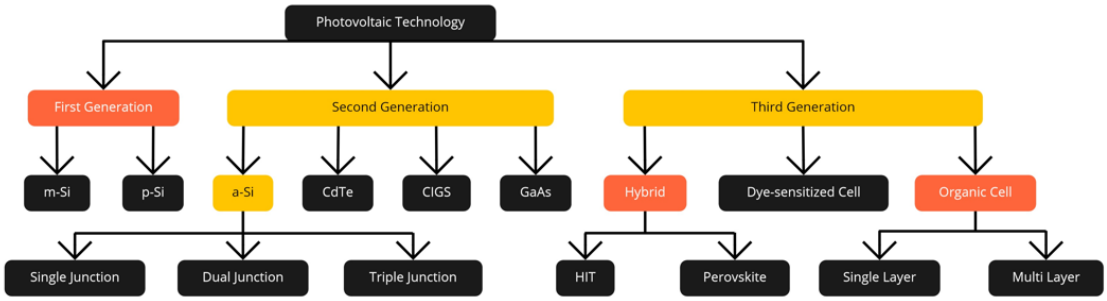

Source: Adapted from [15]

continuous crystal structure, offering efficiencies between 18% and 22%. Polycrystalline Cells (p-Si), while less efficient (around 15% to 18%), are cheaper to produce because they are made from silicon crystals that are melted and poured into molds before being sliced into wafers [16]. The popularity of silicon-based cells stems from the abundance of silicon as a material and the maturity of manufacturing processes that have been optimized over decades. However, the production of these cells involves high energy consumption and cost, primarily due to the need to purify silicon to a high degree and the energy-intensive processes of cutting and shaping wafers.

- Second-Generation: Thin-Film Solar Cells are made by depositing thin layers of photovoltaic materials, such as Cadmium Telluride (CdTe), Amorphous Silicon (a-Si), or Copper Indium Gallium Selenide (CIGS) or Gallium Arsenide (GaAs), onto a substrate. Thin-film cells are generally less efficient than crystalline silicon cells, with efficiencies ranging from 10% to 16%. However, their lower cost and flexibility make them appealing for applications where space and weight are concerns [13].

  Thin-film technologies have the advantage of being applied to various surfaces, including flexible and curved ones, making them suitable for Building-Integrated Photovoltaics (BIPV) and portable solar products. Additionally, thin-film cells typically require less material and energy to manufacture compared to first-generation technologies, reducing the overall cost per watt of solar energy produced.

- Third-Generation: Emerging Photovoltaic Technologies focus on improving the limitations of previous generations by exploring new materials and cell architectures. These include Organic Photovoltaics (OPV), Dye-Sensitized Solar Cells (DSSC), and multi-junction cells (Hybrid).

  Perovskite solar cells, in particular, have garnered significant attention due to their rapidly increasing efficiencies and the potential for low-cost production. Perovskite cells are made from materials with a crystal structure similar to the mineral perovskite, which allows for broad light absorption and simpler manufacturing processes. However, their long-term stability and scalability remain challenges.

  Multi-junction solar cells are another promising third-generation technology, designed to capture a broader spectrum of sunlight by layering multiple semiconductor materials, each tuned to a different portion of the solar spectrum. This approach has resulted in the highest efficiencies achieved to date, with some multi-junction cells exceeding 40% efficiency under concentrated sunlight [17]. However, these cells are still very expensive and are mainly used in specialized applications like space technology.

2.1.5 Comparison of Existing Photovoltaic Cells

The comparison of photovoltaic technologies can be categorized into three generations, each with distinct characteristics in terms of weight, substrate flexibility, material usage, manufacturing complexity, and efficiency. These differences highlight the trade-offs between cost, performance, and applicability across various solar energy solutions. The table below summarizes these key aspects for each generation of photovoltaic cells.

The table comparing photovoltaic technologies highlights key differences across the three generations of solar cells. First-generation cells, primarily based on silicon (Si), are heavy and rigid, utilizing abundant raw materials but with some toxic substances in their production process. Despite their complex and costly manufacturing, they offer high efficiency and long lifespan, making them dominant in the current market. However, they

Table 2.1: Comparison of Photovoltaic Technologies

	1st Generation	2nd Generation	3rd Generation
Weight	Heavy	Light	Light
Substrate	Rigid	Flexible	Flexible
Raw Material	Abundant	Scarce	Abundant
Toxic Substances	Some	Many	Mostly Non-toxic
Transparency	Opaque	Semi-transparent	Semi-transparent
Manufacturing Complexity	Complex	Simple	Simple
Manufacturing Cost	High	Low Prospect	Low Prospect
Raw Material Cost	High	High	Low Prospect
Efficiency	High	High	Low
Lifespan	Long	Long	Short
Efficiency Loss due to Heat	Significant	Insignificant	Insignificant

Source: Adapted from [18]

experience significant efficiency loss due to heat, which is a drawback in certain climates.

Second-generation technologies, including thin-film cells like CdTe, a-Si, and CIGS, are lighter and more flexible, making them suitable for applications requiring portability or integration into buildings. However, they rely on scarcer raw materials and involve more toxic substances. These technologies are generally easier and cheaper to manufacture than first-generation cells, although their efficiency is still high, and their performance is more stable under heat.

Third-generation technologies, such as organic photovoltaic cells (OPVs), are notable for their use of abundant and mostly non-toxic materials. These cells are light and flexible but have low efficiency and short lifespans, which currently limit their market potential. Despite their lower performance, they show promise due to the simplicity of their manufacturing and the prospect of significant cost reductions in the future.

According to the conclusions drawn by Pérez, although there have been substantial advances in photovoltaic technology, first-generation silicon-based cells will continue to dominate due to their efficiency, cost, and material abundance. While thin-film technologies like OPVs show great potential for future development, their current limitations, such as low efficiency and short lifespan, prevent them from replacing existing technologies.

Ongoing research aims to mitigate these disadvantages, but OPVs are still primarily in experimental use, with their commercial viability yet to be proven [18].

2.2 Electric Buses

2.2.1 Evolution of Electric Buses

Public transportation was first established in 1661 with the creation of the "Pascal public transport" system. Later, in 1826, "Omnibuses" were introduced—large vehicles that ran on fixed routes and could carry up to 15 passengers, using either horse-drawn or rickshaw power. This innovation was introduced in Philadelphia in 1830.

In the early 19th century, technological advancements in electrochemical batteries, pioneered by Alessandro Volta, demonstrated that energy could be stored through chemical processes. In 1821, Michael Faraday used Volta's batteries in experiments to demonstrate the principles of electric motors and generators. These breakthroughs marked the beginning of the first phase of electric vehicles and generators.

Subsequent improvements in battery technology and charging systems led to the development of regenerative braking, a key innovation that allows an electric motor to function as a generator to recharge the battery while the vehicle is in motion [19].

In public transportation, trams running on fixed rails were introduced by Siemens in 1882, along with trolleybuses, which used rubber tires for movement. Both types of electric buses were powered by overhead electric cables. The "Electromote", a public transportation bus powered by electricity supplied through roof-mounted cables, became a milestone in electric transport technology [20].

Over time, public buses evolved into more advanced forms, such as battery-electric buses, plug-in hybrid buses, and fuel cell electric buses [21]. This technological evolution demonstrates the crucial role electric public transport has played in advancing sustainable urban mobility over the centuries.

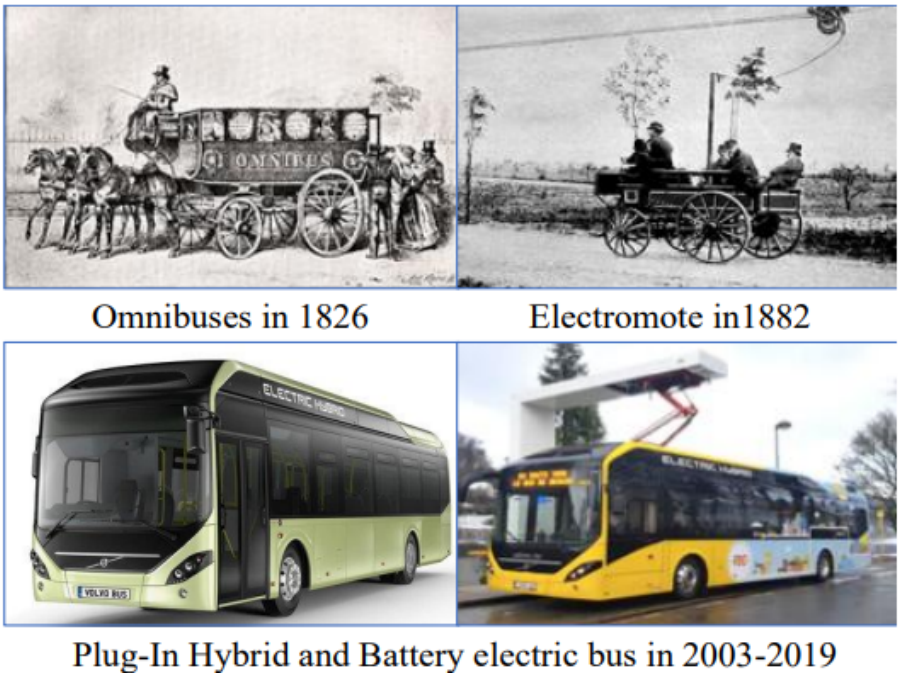

Figure 2.4: History of the electric buses
Source: [21]

2.2.2 Types of Electric Vehicles

The current state of the global automotive industry is characterized by the production and commercialization of three primary categories of electric vehicles:

- Hybrid Electric Vehicles (HEVs): These vehicles integrate an electric motor powered by a battery pack alongside a traditional internal combustion engine. HEVs can be configured in either a series or parallel system. In the series configuration, the electric motor can charge the batteries and/or drive the vehicle, while in parallel systems, both motors can operate simultaneously. The main benefit of HEVs compared to conventional gasoline vehicles is the improved fuel efficiency. However, their higher upfront cost often poses a challenge for potential consumers.

- Plug-in Hybrid Electric Vehicles (PHEVs): PHEVs combine an internal combustion engine with an electric propulsion system that can be recharged from an external source. This setup allows for flexibility in operation, ranging from running solely on

gasoline to using only electric power. While PHEVs offer better energy efficiency than standard vehicles, they typically fall short of the performance metrics achieved by fully electric vehicles. Thus, they represent a middle ground between traditional combustion engines and fully electric options.

- Battery Electric Vehicles (BEVs): The focus of this study, BEVs are entirely electric and depend solely on external charging. They are propelled by energy stored in large battery packs and often feature regenerative braking systems to recapture energy during deceleration. BEVs are recognized for their high energy efficiency and lower operational costs per kilometer traveled. However, the substantial size of the battery can reduce available cargo space. Despite the variety of batteries available, all BEVs share a common drawback: their driving range typically does not match that of conventional vehicles. This limitation is frequently identified as a significant barrier to broader adoption, indicating a need for adjustments to current transportation infrastructure [22].

2.2.3 Urban electric bus technologies

The development of urban electric bus technologies encompasses a diverse array of configurations and choices tailored to meet the specific needs of different environments. As highlighted by Göhlich et al. (2018) [23] , several critical factors influence the design of these systems, including energy sources, charging strategies, refueling interfaces, and the types of onboard energy storage systems employed.

The table presented in their study categorizes these options into distinct functions, illustrating the multifaceted nature of urban electric bus systems. For instance, energy sources can vary between grid connections—ranging from low to high voltage—and local storage solutions like hydrogen tanks or stationary batteries. Charging and refueling strategies also present various methodologies, such as opportunity charging, depot charging, and dynamic in-motion charging, each offering unique advantages and challenges.

Onboard energy sources can include Lithium Nickel Manganese Cobalt (NMC), Lithium

Function	Options					
	grid				local storage	
energy source	low voltage	medium voltage	high voltage	rail	stationary battery	H_2 tank
charging/ refueling strategy	opportunity	in motion	depot			
charging/ refueling interface	manual (plug, pump nozzle)	pantograph	induction	trolleybus current collector	battery swapping	
on-board energy source	battery: NMC	battery: LFP	battery: LTO	capacitor	H_2 tank (+ fuel cell)	none
drive motor	permanent magnet synchronous	electrically excited synchronous	asynchronous	switched reluctance		
drive topology	central motor	wheel hub motor				
body type	12 m single-deck	18 m articulated	24 m bi-articulated	double-deck		
cooling	electric air-conditioning	none				
heating	electric resistance heating	electric heat pump	fuel heating			

Figure 2.5: Morphological matrix of available technology options in electric bus systems Source: [23]

Iron Phosphate (LFP), Lithium Titanate Oxide (LTO), and even capacitors, reflecting the trade-offs between energy density, cost, and operational requirements. The type of drive motor—whether permanent magnet synchronous, asynchronous, or switched reluctance—affects the overall efficiency and performance of the bus, while the drive topology can dictate vehicle design, such as central motors versus wheel hub motors.

Furthermore, considerations regarding body type, including single-deck, articulated, and double-deck buses, as well as climate control systems, play a vital role in the practical application of electric buses in urban settings. These various elements come together to form an adaptable and efficient transportation solution that can significantly contribute to sustainable urban mobility.

The technological landscape for urban electric buses offers a wide range of solutions, each designed to address specific operational requirements and infrastructure conditions. The choice of energy sources, charging methods, drive systems, and bus configurations

must be carefully aligned with the needs of the city and its public transport system. As cities move towards more sustainable transit options, the integration of these technologies will be key to reducing emissions and operational costs, while also improving the overall efficiency of public transportation. The future of electric urban buses lies in continuous innovation and adaptation, ensuring they meet the growing demand for cleaner and smarter urban mobility solutions.

2.2.4 Electric Bus Characteristics for Public Transportation

This section presents a comparative overview of various electric bus models relevant to the city of Curitiba, focusing on their key specifications and operational features. The selected manufacturers — Volvo, BYD, Mercedes, and Higer — represent a range of technologies being implemented or considered for public transportation in Brazil.

Volvo and BYD already operate in Curitiba with the models mentioned in the following Table 2.2. Higer, though not yet in regular operation, is currently testing its 12-meter model in several Brazilian cities, including Curitiba. Mercedes, on the other hand, has entered the electric bus market in Brazil with its model slated for production in São Bernardo do Campo (SP). While its primary market is expected to be São Paulo, it was included in this study to provide a broader comparison. The table below highlights the essential characteristics of each bus, including dimensions, passenger capacity, battery technology, and electric motor power.

The catalogs for the buses under study are available in appendix B for further reference.

Table 2.2: Comparison of Electric Bus Specifications

	Volvo	BYD	Mercedes	Higer
Model	VOLVO BZL ELECTRIC	D9W	eO500 U 2134/59	AZURE PADRON
Length	12 m	12,265 m	up to 13,2 m	12,5 m
Weight	19,500 Kg	20,500 Kg	21,200 Kg	21,000 Kg
Passenger Capacity	80 people	80 people	80 people	80 people
Battery Technology	Lithium-ion, NCA	BYD LifePO4	Lithium-ion, NMC	Lithium Iron Phosphate
Electric Motor	200/400 kW	150 kW*2	250 kW	260 kW
Battery Capacity	470 kWh	344 kWh	up to 588 kWh	385 kWh
System Voltage	600 V	380 V	665 V	637.56 V

Source: Provided Data

Volvo, one of the most prominent manufacturers in the electric bus market, has introduced the Volvo BZL Electric model. This bus is 12 meters long and weighs 19,500 kg, with a passenger capacity of 80 people, matching the capacity of the other models compared. Its battery technology is based on Lithium-ion NCA (Nickel-Cobalt-Aluminum), which offers high energy density and a total battery capacity of 470 kWh. This ensures an extended operational range, reducing the need for frequent recharging, which is advantageous in a city like Curitiba, where buses operate for long hours on extensive routes.

BYD, a major Chinese bus manufacturer, offers the D9W model, which has a slightly longer length of 12.265 meters and weighs 20,500 kg. Its battery capacity of 344 kWh, supported by BYD's LifePO4 (Lithium Iron Phosphate) battery technology, is lower compared to the Volvo model but provides sufficient range for urban operations. The electric motor is divided into two units of 150 kW, giving it a combined power output of 300 kW.

Mercedes provides the eO500 U 2134/59 model, with a length that can extend up to 13.2 meters, making it the longest bus in the comparison. Its battery technology is based on Lithium-ion NMC (Nickel-Manganese-Cobalt), which is known for balancing energy density and safety. The battery capacity can reach up to 588 kWh, allowing for longer operational times, but the passenger capacity remains at 80 people, similar to the BYD and Higer models.

The Higer Azure Padron model, which has a length of 12.5 meters and a weight of 21,000 kg, also operates in Curitiba. It uses Lithium Iron Phosphate (LFP) battery technology, with a total capacity of 385 kWh. This model is powered by a 260 kW electric motor and operates at a system voltage of 637.56 V, similar to the voltage ranges of the other models.

Overall, while all these models contribute to Curitiba's electric bus fleet analysis, the focus of this thesis will be on the Volvo BZL Electric, as it combines robust battery technology with sufficient passenger capacity and range, making it a key player in the city's efforts to enhance sustainable public transportation.

2.2.5 Conventional Buses vs. Electric Buses

The use of buses as a mode of mass transit has long been one of the most successful public transportation solutions worldwide. Buses are widely deployed across the globe, boasting advantages such as ease of implementation, route flexibility, high passenger capacity, low infrastructure costs, and an abundant labor force. However, recent years have seen the rise of electric buses as strong competitors to traditional diesel-powered buses, particularly due to their potential for reducing infrastructure costs and addressing issues like excessive noise, pollutant emissions, and particulate matter production.

Electric buses, which run solely on the energy stored in their battery banks—usually located at the rear or on the roof of the vehicle—are increasingly being introduced in major cities. Early challenges related to limited range are now being addressed as technology advances. For instance, data from electric buses operating in São Paulo show a driving range of up to 200 km, allowing them to be charged once during idle periods or using fast intermediate charging stations, which may reduce battery size. Among the key advantages of electric buses are the near-silent operation of the motor, zero emissions during operation, higher torque at low speeds compared to diesel buses, and lower maintenance and fuel costs than other bus types available on the market [22] [24] .

Moreover, electric motors are notably efficient, with operational efficiencies exceeding 90%, far surpassing the average 30% efficiency of internal combustion engines. This higher efficiency not only makes electric buses more energy-effective but also extends the lifespan of their motors, which typically have only one moving part—the rotor. As a result, electric buses require less frequent and simpler maintenance, providing further cost advantages over conventional buses [24].

2.3 Charging Systems for Electric Buses

2.3.1 Battery Technologies for Electric Buses

In recent years, lithium-ion batteries have gained significant attention as a key energy storage technology, particularly in electric vehicles (EVs). Their high energy density, efficiency, and relatively low self-discharge rate have made them a preferred choice for modern applications. This section focuses on lithium-ion batteries and explores different models, highlighting their advantages, challenges, and specific characteristics. We will delve into key lithium battery types, including lithium iron phosphate (LiFePO4), nickel-manganese-cobalt oxide (LiNiMnCoO2), and lithium nickel cobalt aluminum oxide (LiNiCoAlO2), providing a comparative analysis of their features and suitability for electric vehicle applications.

Lithium Iron Phosphate (LiFePO4)

Discovered by the University of Texas in 1996, lithium iron phosphate (LiFePO4) emerged as a promising cathode material for lithium-ion batteries. It offers remarkable thermal stability and safety, especially under conditions of overcharging, as well as a wide operating temperature range between -30°C and +60°C [25]. Despite its lower energy density compared to other lithium battery chemistries, LiFePO4 excels in long-term reliability, capable of over 1,000 charge/discharge cycles while maintaining a stable output voltage of around 3.4V.

The key to its safety lies in its structural stability. The olivine crystal structure of LiFePO4 provides robust chemical bonds, allowing the material to withstand high temperatures without decomposing, making it particularly reliable for electric vehicles. This stability also contributes to its resistance to thermal runaway, a critical concern in lithium-ion batteries [26]. Moreover, it presents a lower environmental risk and is more easily recyclable compared to other battery materials, such as those based on cobalt [27].

Nickel-Manganese-Cobalt Oxide (LiNiMnCoO2 or NMC)

Another popular type of lithium-ion battery is the nickel-manganese-cobalt oxide battery (LiNiMnCoO2), commonly referred to as NMC. This battery combines the strengths of nickel (high energy density), manganese (low resistance), and cobalt (stability) to optimize overall performance. The typical composition for NMC batteries is 33% nickel, 33% manganese, and 34% cobalt, providing a balance between high energy density and low self-discharge rates, making them highly suitable for EV applications [25].

One of the most notable advantages of NMC batteries is their versatility. Depending on the blend of materials, manufacturers can prioritize either power density or energy density, tailoring the battery for specific applications, such as high-performance electric vehicles or energy storage systems. However, the presence of cobalt increases both the environmental impact and cost of production, which poses challenges for large-scale adoption [28]. Despite these issues, NMC batteries remain widely used in EVs due to their balance of performance, energy density, and lifespan.

Lithium Nickel Cobalt Aluminum Oxide (NCA)

The lithium nickel cobalt aluminum oxide battery (LiNiCoAlO2 or NCA) represents a more specialized form of lithium-ion technology, primarily used in high-performance applications such as electric vehicles. NCA batteries offer high specific energy and long life cycles, making them particularly attractive to automotive manufacturers [25]. The addition of aluminum enhances the thermal stability of the battery, which is crucial for preventing overheating and extending its operational life, especially in demanding environments [29].

While NCA batteries are known for their high energy and power densities, they also come with some drawbacks. Similar to NMC batteries, the cobalt content in NCA batteries increases their production costs and environmental footprint. However, their performance characteristics—particularly their ability to deliver high current and long life

cycles—make them ideal for electric vehicles that demand high energy efficiency and minimal maintenance [30].

Comparative Analysis of Lithium Battery Models

Each lithium battery model offers unique advantages and trade-offs:

- LiFePO4: Known for its safety, thermal stability, and longevity, LiFePO4 batteries are well-suited for applications where safety and cycle life are prioritized over energy density. They are less likely to experience thermal runaway and are environmentally friendlier.

- NMC: Offers a good balance of energy density and cost, making it a versatile option for both EVs and stationary energy storage. However, its reliance on cobalt increases production costs and environmental concerns.

- NCA: Provides the highest energy density and long life cycles, making it the go-to choice for high-performance electric vehicles. Its stability and efficiency are key strengths, though it shares the environmental and cost challenges posed by cobalt.

2.3.2 Types of Electric Vehicle Chargers

Battery chargers come in various forms and functionalities, primarily aimed at efficiently charging batteries while optimizing charging rates and determining when the charging process should be completed. As technology has advanced, chargers have evolved to incorporate sophisticated monitoring and control systems, which enhance battery longevity and ensure the safety of both the battery and surrounding individuals [2].

Chargers can connect to the electrical grid through magnetic coupling or physical connections, with the latter being more prevalent in commercial settings due to its simplicity and cost-effectiveness. Notably, Vehicle-to-Grid (V2G) systems have emerged, allowing for bidirectional energy flow—enabling batteries to draw power from the grid or supply it back when needed [31].

In terms of configuration, chargers are classified as either off-board, which are standalone units installed at charging locations, or on-board, which are integrated within the vehicle. Additionally, chargers can be categorized based on their internal construction into various types:

- Switch Mode Regulators utilize an AC-DC rectifier followed by a DC-DC converter, where output voltage is managed via Pulse Width Modulation (PWM). These systems require larger filters for low-frequency operations but can reduce size at higher frequencies, albeit with increased noise.

- Parallel Chargers involve a semiconductor-controlled converter that is placed in parallel with the power source and the load. Although this configuration is economical and straightforward, it is less common in traction applications.

- Series Chargers, or linear chargers, regulate charging current through linear components, which can lead to inefficiencies.

- Pulsed Chargers, or Silicon Controlled Rectifier (SCR) chargers, use switchable semiconductors to provide high initial currents and then taper off to maintain a lower voltage during the final charging phase.

- Bridge Chargers employ diode or controlled semiconductor bridges linked to an Alternating Current (AC) supply.

- Inductive Charging systems utilize transformers for galvanic isolation between the grid and the battery, often in conjunction with other charger types.

- Ferrous Resonant Chargers feature a transformer designed to lower grid voltage and control charging current, aided by a capacitor linked to the transformer terminals and complemented by a rectifier for AC to DC conversion.

These configurations allow chargers to be classified as either isolated or non-isolated, depending on whether they are directly connected to the grid or involve a transformer for

connection. The majority of chargers in electric vehicles tend to be series, switch mode, or bridge types, highlighting the importance of efficient energy transfer methods [2].

2.3.3 Charging Modes and Strategies

When it comes to charging electric vehicles, various modes have been established to standardize the connection between chargers and vehicles, guided by the International Electrotechnical Commission (IEC) standards. The IEC 62196 outlines four primary charging modes, each designed to meet different charging requirements and scenarios:

- Mode 1: This mode facilitates slow charging through a standard domestic outlet equipped with grounding. It limits the current to 16 A at 250 V for single-phase connections or up to 480 V for three-phase systems. This option is typically used for overnight charging when quick replenishment is not essential.

- Mode 2: Similar to Mode 1, this mode also uses a conventional outlet but incorporates protective equipment for the EV. This safety equipment must be grounded and positioned within a maximum distance of thirty centimeters from the outlet. Current is capped at 32 A for 250 V (single-phase) or 480 V (three-phase), ensuring safe operation during the charging process.

- Mode 3: This mode allows for either slow or rapid charging through dedicated EV chargers. It employs connectors defined by the IEC 61851-1 standard at each end of the cable or utilizes the SAE J1772 connection. Current limits are set to 32 A for slow charging and up to 250 A for rapid charging. This setup enables communication between the vehicle and charger, facilitating interaction with smart grid technologies.

- Mode 4: This mode is designed for fast charging using DC. It supports a maximum current of 400 A, utilizing connectors known as CHAdeMO, which are compatible with specific EV models. Mode 4 connections are generally limited to 500 V DC and 125 A, offering the unique capability to read the vehicle's Controller Area Network

(CAN) bus, allowing the charger to ascertain the battery's state of charge and optimize the charging process accordingly.

These standardized modes of charging not only enhance the compatibility of charging infrastructure with various electric vehicle models but also promote the safe and efficient use of electric energy during the charging process [2].

2.4 DC-DC Converters

2.4.1 Overview of DC-DC Converter Types

DC-DC converters are essential components in the conversion and control of direct current electrical energy, adjusting parameters such as voltage, current, and frequency. They use semiconductors like IGBT and MOSFET to operate cyclically through PWM signals, and they also incorporate passive elements such as inductors, diodes, and capacitors to ensure efficient energy conversion [32] [33].

One of the key characteristics of these converters is the duty cycle, which determines the fraction of the switching cycle during which the semiconductor is in conduction, thereby controlling the output voltage. This parameter is crucial for converter operation and is calculated by the ratio between the time the device is conducting and the total switching period [33] [34].

DC-DC converters are typically classified as isolated or non-isolated, depending on the presence of a transformer for galvanic isolation. While non-isolated converters are simpler, isolated converters use high-frequency transformers and require the integration of additional converters to ensure proper transformer operation [33] [34].

Additionally, converters can operate in continuous or discontinuous conduction modes. In continuous mode, part of the energy stored in the inductor is transferred to the load, while in discontinuous mode, all energy is released, causing the current to temporarily drop to zero [35] [36]. The choice of operating mode directly impacts system performance and efficiency.

Step-Down Converter (Buck)

The step-down converter, also known as a buck converter, is a type of DC-DC converter that generates an output voltage that is equal to or lower than the input voltage. Its operation is based on the storage and discharge of energy through an inductor L, which is controlled by the duty cycle *(δ)* of the PWM signal applied to the transistor (or switch) in the circuit [32].

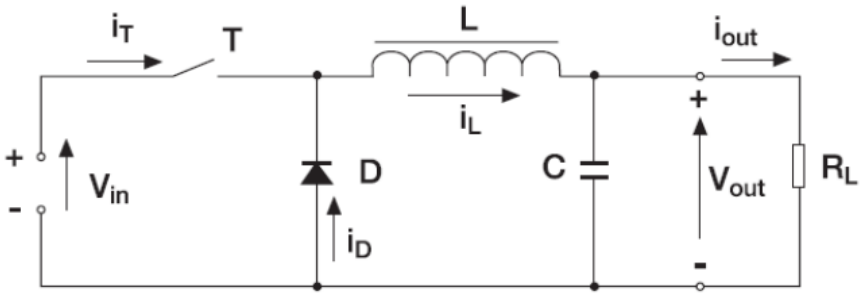

Figure 2.6: Step-Down Converter (Buck)

Source: [32]

The converter operates in two main stages:

- 1st Stage (Transistor Conducting): When the transistor is conducting, the current flows through the inductor L and the load connected to the output. During this phase, the inductor is magnetized, and energy is delivered to the output.
- 2nd Stage (Transistor Off): When the transistor is turned off, the diode starts conducting, allowing the inductor L to demagnetize, transferring its stored energy to the load.

The analysis of the circuit leads to the determination of the relationship between the input voltage (Vin), the output voltage ($Vout$), and the duty cycle (δ), expressed by the following equation:

$$(V_{in} - V_{out}) \cdot \delta \cdot T = -V_{out} \cdot (1 - \delta) \cdot T \tag{2.1}$$

Therefore, the static gain, under continuous operation conditions [32], is given by:

$$\frac{V_{out}}{V_{in}} = \delta \tag{2.2}$$

Thus, the static gain of the converter, for continuous mode operation, is defined by this relationship. Since the duty cycle (δ) ranges between 0 and 1, it can be concluded that the output voltage will always be lower or equal to the input voltage ($V_{in} \geq V_{out}$), fulfilling the purpose of the buck converter, which is to provide a reduced voltage at the output [32].

Step-Up or Boost Converter

This converter generates a DC output voltage that is equal to or higher than the input voltage. The electrical diagram of this type of converter can be seen in Figure 2.4.1.

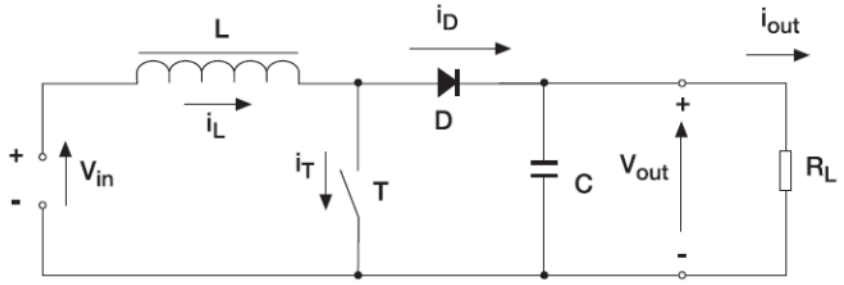

Figure 2.7: Step-Up or Boost Converter

Source: [32]

Like the previous converter, this one operates on the principles of energy storage and discharge in the inductor L, with its behavior controlled by the duty cycle of the PWM signal applied to the transistor (switch). The operation of this converter is also divided into two stages [32]:

- 1st Stage: Occurs when the transistor is conducting. Current flows through the inductor, during which the inductor L is magnetized.

- 2nd Stage: In this stage, the switch is open, meaning the transistor is not conducting. During this stage, the diode begins to conduct, and the inductor is demagnetized. The source (*Vin*) and the inductor supply energy to the load, resulting in an increase in output voltage.

By observing the circuit, the equation that represents it is as follows:

$$V_{in} \cdot \delta \cdot T = (V_{out} - V_{in}) \cdot (1 - \delta) \cdot T \tag{2.3}$$

Thus, the static gain of the boost converter, under continuous conduction mode, is [32]:

$$\frac{V_{out}}{V_{in}} = \frac{1}{1 - \delta} \tag{2.4}$$

Since it assumes values between 0 and 1, we can conclude that ($V_{out} \geq V_{in}$), fulfilling the purpose of this converter, which is to provide an output voltage higher than the input voltage.

In the context of converters, particularly those designed to produce an output voltage higher than the input voltage, there are other types that provide an even greater ratio between these voltages. This is influenced by the number of components used and their respective configurations. Examples include the Cascade boost, Interleaved boost, Multilevel boost, Hybrid boost, and Quadratic converters.

Step-Up/Down Converter or Buck-Boost

The buck-boost converter is designed to provide an output voltage that can either exceed or fall below the input voltage, depending on the requirements of the application. Figure 2.4.1 illustrates the electrical schematic of this type of converter.

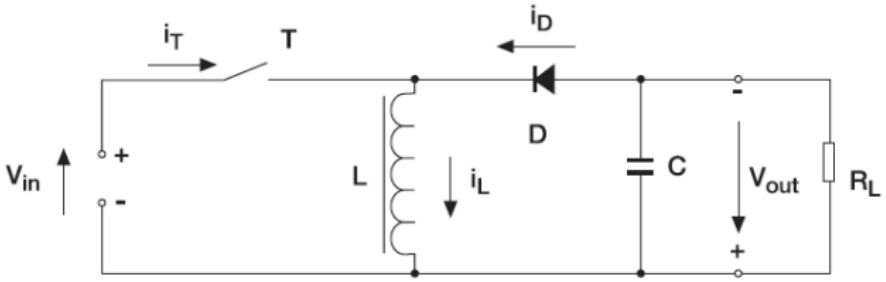

Figure 2.8: Step-Up/Down Converter (Buck-Boost)
Source: [32]

This converter effectively combines the functionalities of both step-up and step-down converters, and its operation is similarly based on controlling energy within the inductor (L). This control is achieved through the duty cycle of the PWM signal applied to the transistor. A notable feature of this converter is that the output voltage ($Vout$) can be negative relative to the ground. Its operation can be divided into two distinct phases:

- 1st Stage – This phase occurs when the transistor is in the conducting state. During this time, current flows through the inductor, resulting in the magnetization of inductor L.

- 2nd Stage – In this phase, the switch is open, indicating that the transistor is not conducting. The diode begins to conduct, and the energy stored in inductor L is delivered to the load (output), leading to the demagnetization of the inductor.

The governing equation for this circuit is represented as follows:

$$V_{in} \cdot \delta \cdot T = -V_{out} \cdot (1 - \delta) \cdot T \tag{2.5}$$

Thus, the static gain for non-latching operation can be expressed as:

$$\frac{V_{out}}{V_{in}} = \frac{-\delta}{1 - \delta} \tag{2.6}$$

Since δ can take values between 0 and 1, it follows that, depending on the desired outcome. It can be observed that the output voltage may be greater or lesser than the input voltage [32].

Flyback Converter

The Flyback converter is a type of isolated DC-DC converter, derived from the buck-boost topology, that allows the output voltage to be either higher or lower than the input voltage. Unlike non-isolated converters, isolated converters like the Flyback use a high-frequency transformer to provide electrical isolation between the input and output, which is critical in many applications. The control of this converter, as with other DC-DC converters, is achieved through a Pulse Width Modulation (PWM) signal with a variable duty cycle [37].

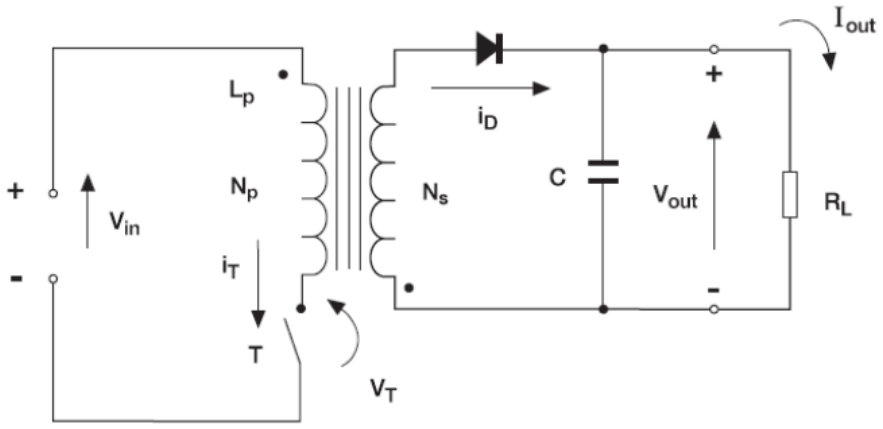

Figure 2.9: Flyback Converter

Source: [32]

In the Flyback converter, energy transfer occurs via the transformer's windings. When the transistor (switch) is turned on, energy is stored in the primary winding of the transformer. Once the transistor is turned off, this energy is transferred to the secondary winding, supplying the load. This operating mechanism provides both voltage isolation and a flexible conversion ratio, depending on the turns ratio of the transformer. The

static gain for the Flyback converter in continuous conduction mode can be described by:

$$\frac{V_{out}}{V_{in}} = \frac{N_s}{N_p} \cdot \frac{\delta}{1-\delta} \tag{2.7}$$

Where N_s and N_p represent the number of turns on the secondary and primary windings, respectively. Notably, when $N_s = N_p$, the equation resembles that of the buck-boost converter, showing the Flyback's roots in this topology [32].

One of the key challenges with Flyback converters is the high voltage spikes that occur when the transistor is switched off, due to the energy stored in the transformer's leakage inductance. To mitigate these voltage spikes and prevent damage to the switch, it is common to use a snubber circuit in parallel with the transistor [32].

In isolated step-up/down converters like the Flyback, the transformer serves not only to provide isolation but also to control the energy transfer. As described, when the transistor is closed, the input voltage magnetizes the transformer's primary winding. Once the switch opens, the stored energy is transferred to the secondary winding, which then supplies the output voltage. This process enables the Flyback converter to handle a wide range of input and output voltage ratios depending on the application [2] [37].

Forward Converter

The forward converter is a type of isolated DC-DC converter, derived from the buck (step-down) converter. The key difference from non-isolated converters lies in the inclusion of a transformer, which provides galvanic isolation between the input and output. This transformer also defines the turns ratio, allowing the forward converter to generate an output voltage either higher or lower than the input voltage, depending on the relationship between the primary (N_p) and secondary (N_s) windings. When $N_s = N_p$, the forward converter behaves similarly to the buck converter, producing an output voltage lower than the input [32].

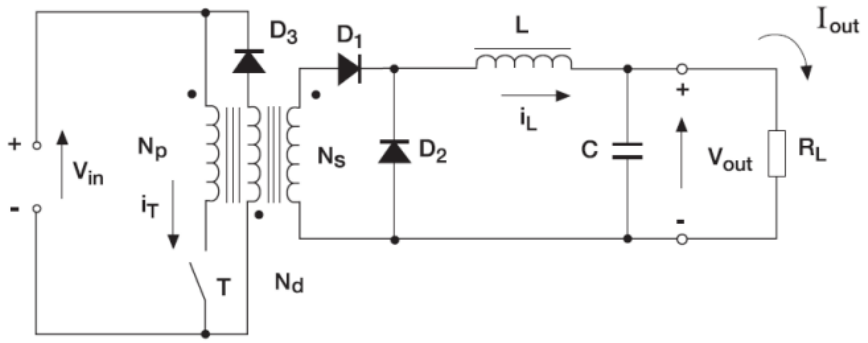

Figure 2.10: Forward Converter

Source: [32]

During its operation, the forward converter follows two main stages. In the first stage, when the switching transistor is closed, the input energy is directly transferred to the load through the primary winding of the transformer, while diode D_1 conducts, and diode D_2 remains off. At this point, energy is also stored in the inductor L. In the second stage, when the transistor opens, diode D_2 starts conducting, releasing the stored energy from the inductor L to the output, while diode D_1 turns off [2].

The static gain of the forward converter, in continuous conduction mode (CCM), can be expressed by the following equation:

$$\frac{V_{out}}{V_{in}} = \frac{N_s}{N_p} \cdot \delta \tag{2.8}$$

Where D represents the duty cycle of the PWM signal applied to the switching transistor [32]. This relationship shows that the output voltage can be adjusted by both the duty cycle and the transformer turns ratio. In cases where $N_s = N_p$, the equation closely resembles the buck converter's transfer function [2].

An important aspect of the forward converter is the need for demagnetization circuits for the transformer. Unlike the flyback converter, the magnetic flux in the transformer does not automatically reset at the end of each cycle. Therefore, a reset winding or energy recovery circuits are often required to prevent transformer saturation.

This converter is widely used in power supply systems, particularly where isolation between input and output is needed, along with precise output voltage control, such as in energy conversion systems for electric vehicles and solar panels [2].

Full Bridge Converter

The full bridge converter enables functionality akin to that of the half bridge converter. However, this converter achieves a gain that is double that of the half bridge converter and is characterized by a more complex circuit topology, as illustrated in the following figure 2.4.1.

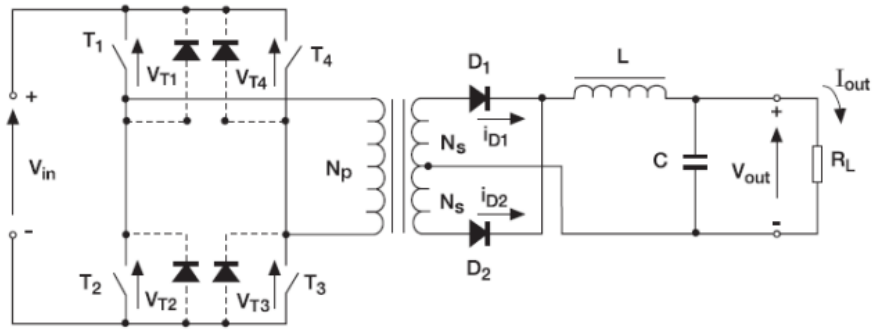

Figure 2.11: Full Bridge Converter

Source: [32]

This is due to the application of an alternating voltage of $\pm V_{in}$ at the primary winding. Thus, the static gain of the full bridge converter, in continuous conduction mode (CCM), is given by the following equation [32]:

$$\frac{V_{out}}{V_{in}} = 2 \cdot \left(\frac{N_s}{N_p}\right) \cdot \delta \quad (0 < \delta < 0.5) \tag{2.9}$$

Its operation consists of two distinct phases. The switches (T) are activated in pairs; for instance, when switches T_1 and T_2 are conducting, switches T_3 and T_4 are off. During the conduction of T_1 and T_2, diode D_1 conducts while diode D_2 remains off, and the opposite occurs when T_3 and T_4 are conducting. The transition between these two operational

phases includes a brief period when both diodes conduct simultaneously [2].

This method of operation allows for greater flexibility in controlling the output voltage, making the full bridge converter particularly suitable for applications requiring isolation between input and output, along with precise voltage regulation [2].

2.5 MPPT (Maximum Power Point Tracking)

In photovoltaic system installations, it is crucial to design a solar system to operate under optimal conditions and maximize efficiency. Early research aimed at extracting maximum power from a photovoltaic (PV) panel initially focused on mechanical systems that moved PV panels to capture the most solar radiation possible. These mechanical systems tracked the sun's movement across the sky, adjusting the panels accordingly. While effective, this method was later complemented by electrical tracking systems, known as Maximum Power Point Trackers (MPPT). MPPT systems are based on voltage and current variations during PV system operation, allowing for the extraction of maximum power by ensuring the system operates at its optimal point of efficiency [38].

In a typical scenario, when a PV generator is connected directly to a load, the operating point might be far from the maximum power point (MPP) of the system. This mismatch occurs due to the intersection of the voltage-current curve with the load line, which may not align with the MPP. To address this, an electronic converter is often introduced between the PV generator and the load. This converter not only searches for the MPP but also performs additional functions specific to these systems. The full system, as illustrated in Figure 2.5, consists of the PV generator, sensors, control device, MPPT algorithm, and the load.

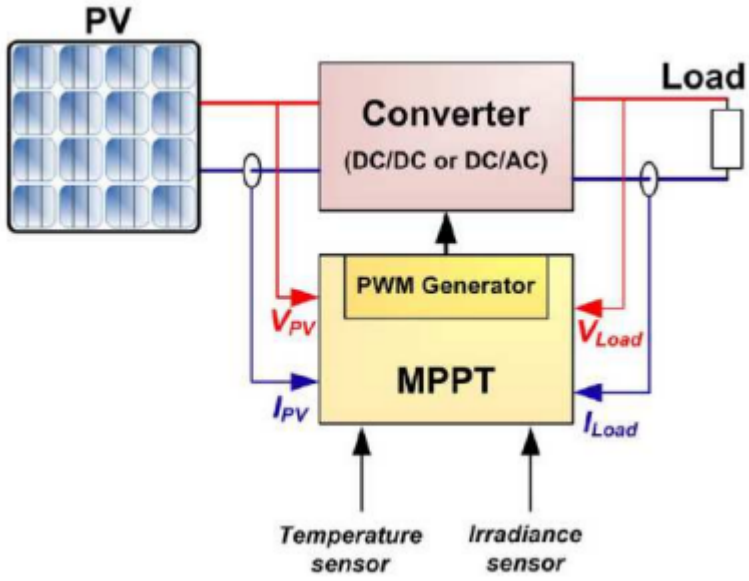

Figure 2.12: Block diagram of the PV system with MPPT

Source: [39]

The MPPT algorithm monitors the voltage and current at the input, and sometimes also accounts for climatic variations, adjusting the duty cycle to minimize any deviation from the optimal point. This adjustment occurs cyclically until the system reaches the MPP [39], [40].

The primary goal of using MPPT is to ensure that, regardless of environmental conditions—particularly solar radiation and temperature—the photovoltaic system operates at its maximum power output. These algorithms are designed to find the Maximum Power Point (MPP) under various operating conditions and adjust the system's operation accordingly.

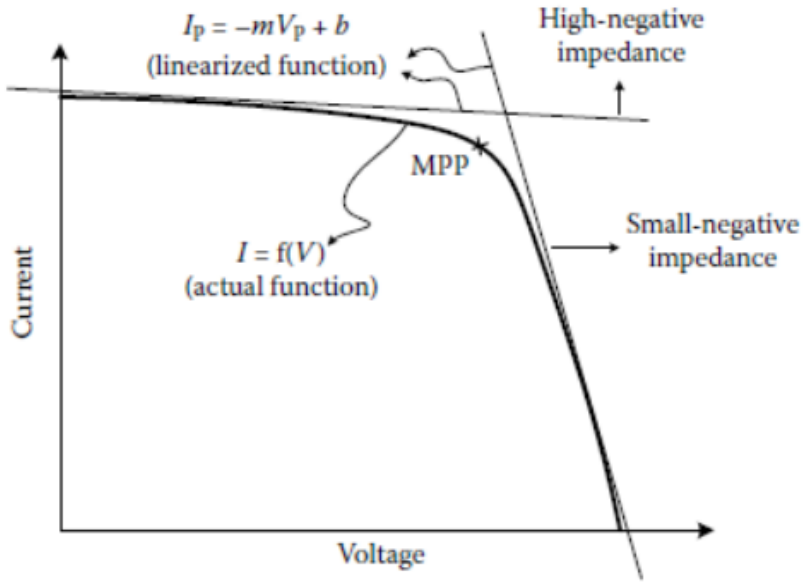

Figure 2.13: Characteristic curve of a photovoltaic panel

Source: [41]

Identifying the MPP involves analyzing the power/voltage equation, which is derived by taking the second derivative of the current/voltage equation. This mathematical process reveals the point at which the power output reaches its peak. At the MPP, the specific values of voltage and current ensure that the power output is maximized, thereby enabling the photovoltaic (PV) system to operate with optimal efficiency.

In this thesis, the MPPT algorithms under study are Constant Voltage, Perturb and Observe (P&O), Incremental Conductance (IC), and Fixed Duty Cycle.

Constant Voltage (Vcte): This method maintains the operating voltage of the photovoltaic module at a constant value, close to the maximum power point. While simple to implement, its effectiveness can be limited, especially under varying environmental conditions, as it does not adequately respond to changes in irradiance or temperature [42], [43].

Perturb and Observe (P&O): This algorithm introduces small perturbations to the system's voltage or current and observes the resulting power variation. If a perturbation leads to an increase in power, the system continues in that direction; otherwise, it

reverses the perturbation. Despite its popularity, P&O can exhibit oscillations around the maximum power point and reduced performance under rapidly changing environmental conditions [43], [39].

Incremental Conductance (IC): This method calculates the incremental conductance of the system and compares it with the instantaneous conductance to determine the necessary adjustment direction to reach the maximum power point. IC offers greater accuracy compared to P&O, particularly in rapidly changing conditions, but it is more complex to implement [44].

Fixed Duty Cycle (D): This method operates the converter with a fixed duty cycle, without considering variations in environmental conditions or load. While the simplest approach, it is also the least efficient, as it does not adjust the operating point to maximize the power extracted from the photovoltaic module [45], [42].

The choice of an appropriate MPPT algorithm is crucial to optimizing the efficiency of photovoltaic systems, considering the trade-offs between implementation complexity and performance under diverse operating conditions.

Chapter 3

Methodology

In this chapter, the focus is on the models related to the connections between the photovoltaic panel and the battery, exploring the ideal configuration for maximizing energy efficiency with the goal of optimizing battery charging. The methodology addresses key components of the photovoltaic system, including the principles of photovoltaic generation, the mathematical modeling of the system, and the design of the modules and converters.

Additionally, simulations of the current-voltage (I-V) curves are performed to assess system performance under various conditions. Different types of DC-DC converters, such as boost and quadratic converters, are explored, with a detailed analysis of their design and operation. The chapter also introduces the control strategies used in the system, such as Maximum Power Point Tracking (MPPT) and the design of controllers.

Lastly, the energy storage system is examined, with a particular focus on the mathematical models that describe the behavior of the battery, including its charge and discharge cycles, efficiency, and State of Charge (SoC). The battery used in this study, along with its technical specifications, is presented in detail.

3.1 Photovoltaic Generation

3.1.1 Operating Principle

Describes the fundamental process by which photovoltaic (PV) cells convert sunlight into electricity, based on the photoelectric effect.

3.1.2 Photovoltaic Module Under Study

The photovoltaic system analyzed in this dissertation consists of a solar panel manufactured by Wattstunde, and the model under study is the HG-L530-72CW. The catalog for this panel can be found in Appendix B.

Table 3.1: Photovoltaic Panel Specifications

Parameter	Value
Maximum Power (Pmax)	530 W
Length (C)	2282 mm
Width (L)	1137 mm
Reference Temperature (Tref)	25°C
Reference Irradiance (Gref)	1000 W/m^2
Max Power Current (Imp)	12.83 A
Max Power Voltage (Vmp)	41.35 V
Short Circuit Current (Isc)	13.76 A
Open Circuit Voltage (Vco)	49.90 V
Solar Cells	144 (6*24)

Parameters of the HG-L530-72CW panel

3.1.3 Mathematical Model

The photovoltaic panel consists of multiple interconnected photovoltaic cells that convert sunlight into electricity through the photovoltaic effect. Each cell, on its own, produces a small amount of energy and a low voltage. To increase energy output, these cells are

connected in series and parallel, forming the photovoltaic panels commonly used in solar energy systems.

The behavior of a photovoltaic module can be described using a mathematical model that establishes a relationship between the current, voltage, and power generated by the panel, considering its physical and environmental characteristics. This model is based on a single-diode equivalent circuit, where the output current is determined by the photo-generated current minus the internal losses of the system.

The equivalent circuit models for photovoltaic cells can range from simple to more complex. The simplest, the ideal model, includes only a current source and a diode. However, more accurate models account for real-world conditions by incorporating additional elements like series and parallel resistances and sometimes multiple diodes.

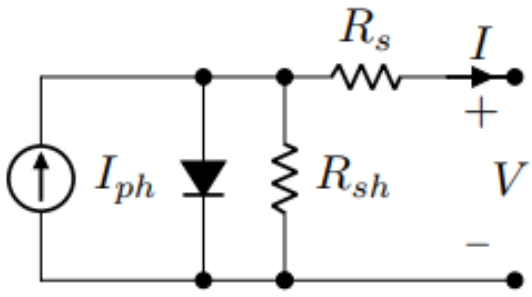

Figure 3.1: Real schematic of the photovoltaic cell

Source: [46]

For this study, the realistic single-diode model is used, which includes a current source, a diode, a series resistance, and a parallel resistance. This model better reflects the actual behavior of the photovoltaic cells under varying conditions, allowing for a more precise analysis of the system's performance.

The equation for the current in a photovoltaic module is derived using Kirchhoff's current law Kirchhoff's current law (KCL), which states that the sum of currents at any node in an electrical circuit must equal zero. In the context of the photovoltaic module's equivalent circuit, this law helps describe the flow of current through the different components of the system.

The resulting equation for the current of the photovoltaic module is expressed as:

$$I = I_{ph} - I_d - I_p \tag{3.1}$$

Where I_{ph} represents the photo-generated current, I_d is the diode current, and I_p denotes the leakage current through the parallel resistance.

The diode current can be expressed by the equation:

$$I_d = I_o \left(e^{\frac{V+R_s I}{mV_T}} - 1 \right) \tag{3.2}$$

Here, I_o is the diode saturation current, V is the panel voltage, R_s is the series resistance, m is the diode ideality factor, and V_T is the thermal voltage, given by:

$$V_T = \frac{kT_{FV}}{q} \tag{3.3}$$

Where k is the Boltzmann constant ($1.38 \times 10^{-23}\, J/K$), q is the electron charge ($1.6 \times 10^{-19}\, C$), and T_{FV} is the temperature of the photovoltaic cell in Kelvin (K).

The reference thermal voltage V_{Tref} is given by:

$$V_{Tref} = \frac{kT_{ref}}{q} \tag{3.4}$$

The leakage current through the parallel resistance I_p is written as:

$$I_p = \frac{V + R_s I}{R_{sh}} \tag{3.5}$$

Where R_{sh} is the parallel resistance. Thus, the complete equation for the current of the photovoltaic module is:

$$I = I_{ph} - I_o \left(e^{\frac{V+R_s I}{mV_T}} - 1 \right) - \frac{V + R_s I}{R_{sh}} \tag{3.6}$$

The voltage equation of the photovoltaic module can be expressed by:

$$V = mV_T \ln\left(\frac{I_{ph} - \left(\frac{V+R_sI}{R_{sh}} - I\right)}{I_o} + 1\right) \tag{3.7}$$

To account for the variation in cell temperature concerning the ambient temperature, we use the equation for the cell temperature T_{FV}:

$$T_{FV} = \theta_c + 273.15 \tag{3.8}$$

Where θ_c is calculated as:

$$\theta_c = \theta_{amb} + \frac{G \cdot (NOCT - 20)}{800} \tag{3.9}$$

Here, θ_c is the cell temperature in degrees Celsius [$^\circ C$], θ_{amb} is the ambient temperature in degrees Celsius [$^\circ C$], G is the irradiance incident on the cell in watts per square meter [W/m^2], and $NominalOperatingCellTemperature(NOCT)$ is the nominal operating cell temperature in degrees Celsius [$^\circ C$].

Continuing with the system sizing, it will be necessary to analyze the parameters associated with the diode's reverse saturation current (I_{or}). To do this, we need to calculate the ideality factor of the photovoltaic panel (m), the reverse saturation current under reference conditions, and the short-circuit current (I_{sc}), taking into account the incident solar radiation.

The process begins with determining the reverse saturation current of the diode under standard conditions (I_{or}). This calculation is based on the simplified diagram of the photovoltaic cell (as shown in Figure 3.2), which operates under open-circuit conditions ($I = 0$ and $I_{ph} = I_{sc}$).

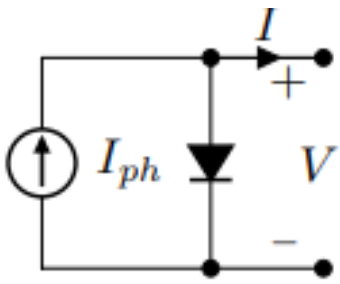

Figure 3.2: Simplified diagram of a photovoltaic cell

Source: [46]

By applying Kirchhoff's current law, we arrive at the following equation:

$$I = I_{ph} - I_{or}\left(e^{\frac{V_{co}}{mV \cdot T_{ref}}} - 1\right) \iff 0 = I_{sc} - I_{or}\left(e^{\frac{V_{co}}{mV \cdot T_{ref}}} - 1\right) \iff$$

$$I_{or} = \frac{I_{sc}}{e^{\frac{V_{co}}{mV \cdot T_{ref}}} - 1} \tag{3.10}$$

As for the ideality factor, it is also determined based on the simplified diagram of the photovoltaic cell (Figure 3.2), where we will apply Kirchhoff's current law and substitute the variables with values provided by the manufacturer, specifically assigning the values corresponding to the maximum power point operating conditions.

$$I = I_{ph} - I_d \iff I = I_{ph} - I_o\left(e^{\frac{V}{mV \cdot T}} - 1\right) \iff$$

$$I_{max} = I_{sc} - I_{or}\left(e^{\frac{V_{max}}{mV \cdot T_{ref}}} - 1\right) \tag{3.11}$$

By solving the previous equation for the ideality factor (m) and substituting the reverse saturation current of the diode under reference conditions (I_{or}) with equation 3.10, we have:

$$m = \frac{V_{max} - V_{co}}{V_{T_{ref}} \ln\left(1 - \frac{I_{max}}{I_{sc}}\right)} \tag{3.12}$$

$$m' = \frac{m}{NSM} \tag{3.13}$$

Where I_{max} is the current at the maximum power point (in amperes [A]), I_{or} is the reverse saturation current under reference conditions (in amperes [A]), I_{sc} is the short-circuit current (in amperes [A]), m' represents the ideality factor of the cell, NSM denotes the number of cells connected in series, V_{co} is the open circuit voltage (in volts [V]), and V_{max} is the voltage at the maximum power point (in volts [V]).

The determination of the diode's reverse saturation current will be carried out considering the characteristics of the material used in the photovoltaic cell [2], since we know that the cells in question are made of silicon. Therefore, we will use the following equations:

$$\left\{ \begin{array}{rcl} I_{or} & = & D \cdot T_{ref}^3 e^{-\frac{\epsilon}{mV \cdot T_{ref}}} \\ I_o & = & D \cdot T_{FV}^3 e^{-\frac{\epsilon}{mV \cdot T}} \end{array} \right\} \Rightarrow \frac{I_o}{I_{or}} = \frac{D \cdot T_{FV}^3 e^{-\frac{\epsilon}{mV \cdot T}}}{D \cdot T_{ref}^3 e^{-\frac{\epsilon}{mV \cdot T_{ref}}}} \Rightarrow$$

$$\Rightarrow I_o = I_{or} \left(\frac{T_{FV}}{T_{ref}} \right)^3 e^{\frac{\epsilon}{m'} \left(\frac{1}{V_{T_{ref}}} - \frac{1}{V_T} \right)} \tag{3.14}$$

Where I_{sc} is the short-circuit current under reference conditions (amperes [A]), and ϵ is the bandgap of silicon ($\epsilon = 1.12\,\text{eV}$).

Given that the short-circuit current of the photovoltaic cell remains almost constant with respect to temperature, unlike the incident solar radiation, the short-circuit current exhibits a linear variation with radiation. This allows the calculation of the short-circuit current using the following expression:

$$I_{sc} = I_{scr} \left(\frac{G}{G_{ref}} \right) \tag{3.15}$$

For sizing, it is essential to relate the parameters that still need to be determined with two operating states of the simplified photovoltaic cell scheme: the open-circuit state and the short-circuit state. Based on the operation in short-circuit, we can determine the source current (I_{ph}), taking into account the conditions of the variables for this state and

the current temperature coefficient (K_i):

$$I_{ph} = I_{scr}\frac{G}{G_{ref}} = [I_{sc} + K_i(T - T_{ref})]\frac{G}{G_{ref}} \tag{3.16}$$

When considering the operation in open circuit, where $I = 0$, the voltage that appears at the panel terminals, known as the open-circuit voltage (V_{co}), represents the maximum voltage generated. Thus, we have:

$$U = V_{co} = mV_T \ln\left(1 + \frac{I_{ph}}{I_o}\right) \tag{3.17}$$

The maximum power generated by a photovoltaic panel is reached at the maximum power point, where the product between the voltage (V_{max}) and the current (I_{max}) is maximized. This point depends on various electrical parameters, including series resistance (R_s) and parallel resistance (R_{sh}). The following equation expresses the maximum power as a function of these variables:

$$\begin{gathered} P_{max} = V_{max} \cdot I_{max} \iff \\ \iff P_{max} = V_{max}\left(I_{ph} - I_o\left[e^{\left(\frac{q}{kT}\cdot\frac{V_{max}+R_s\cdot I_{max}}{N_{sm}\cdot V_{Tm}}\right)} - 1\right] - \frac{V_{max} + R_s \cdot I_{max}}{R_{sh}}\right) \end{gathered} \tag{3.18}$$

In addition, to ensure efficient panel operation, it is important to consider the minimum parallel resistance ($R_{sh_{min}}$). This resistance directly influences the panel's performance, especially under low light conditions. The $R_{sh_{min}}$ can be determined by the following equation, which relates the short-circuit current (I_{sc}) and the maximum power current:

$$R_{sh_{min}} = \frac{V_{max}}{I_{sc} - I_{max}} - \frac{V_{co} - V_{max}}{I_{max}} \tag{3.19}$$

This equation reveals how parallel resistance affects the current and voltage at the

maximum power point, being crucial to minimize losses and optimize the efficiency of the photovoltaic system.

Knowing the minimum value of the parallel resistance, we can calculate the series resistance using the current divider rule. The equation for this relationship is:

$$I_{ph} = \left(\frac{R_{sh} + R_s}{R_{sh}}\right) \cdot I_{sc} \iff R_s = \left(\frac{I_{ph} \cdot R_{sh}}{I_{sc}}\right) - R_{sh} \tag{3.20}$$

If we use the method of the I-V curve slope, the parallel resistance is determined by the slope of the line between the short-circuit point and the maximum power point. The series resistance, on the other hand, is determined by the slope of the line between the maximum power point and the open-circuit point. This gives us the following expressions:

$$R_{sh} = \frac{V_{co}}{I_{sc} - I_{max}} \tag{3.21}$$

$$R_s = \frac{V_{co} - V_{max}}{I_{max}} \tag{3.22}$$

These equations allow us to calculate both the parallel and series resistances, providing a more complete understanding of the panel's electrical characteristics and optimizing its performance by minimizing losses.

3.2 DC-DC Converters

In photovoltaic systems, DC/DC converters play a key role in optimizing energy transfer between solar panels and batteries by adjusting input and output voltages based on system requirements. In this project, we focus on two topologies: the boost converter and the quadratic converter. These were selected for their efficiency in voltage elevation without isolation, which streamlines the system and reduces energy loss from transformers.

The boost converter is commonly used in renewable energy applications, as it raises the output voltage above the input, converting the energy from photovoltaic panels (usually at lower voltage) to a suitable level for battery charging. Techniques like MPPT (Maximum

Power Point Tracking) are applied to maximize energy capture, regulating the switching of transistors, such as MOSFETs or IGBTs, based on system requirements like switching frequency, power, and operating voltage.

The quadratic converter—a variant of the boost converter—offers even higher voltage gain, which is essential when there is a large difference between the panel input voltage and the battery's required voltage. This topology enhances stability and efficiency in high-voltage applications, preventing current fluctuations and ensuring a continuous power supply. As with the boost converter, control methods in the quadratic design allow for distinct operating modes based on current or voltage control, adjusting transistor switching as needed.

Using both converters enables various configurations, adapting to the photovoltaic and battery characteristics. The choice of these converters not only meets the need for voltage elevation but also provides a stable and efficient energy flow from panel to battery, with control adjustments that optimize power transfer based on irradiance and load conditions.

3.2.1 Boost Converter

To raise the low voltage provided by the photovoltaic panel to the necessary level for charging, a boost converter was chosen. This converter operates in two distinct phases.

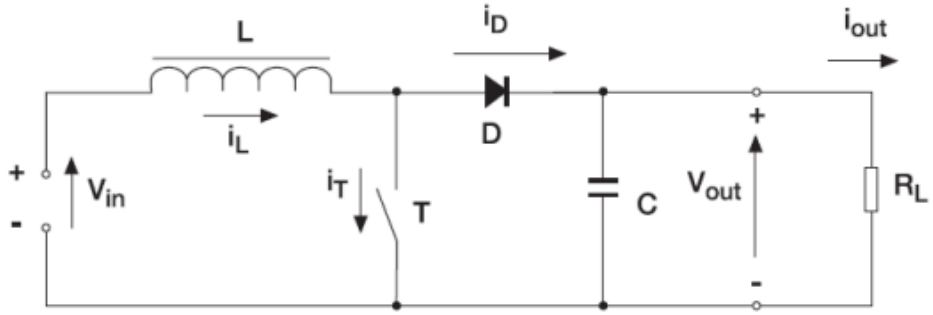

Figure 3.3: Boost Converter

Source: [32]

In the first phase, when the switch is closed and the transistor conducts, current flows

through the inductor, accumulating magnetic energy. The inductor thus temporarily stores energy in preparation for transfer to the load.

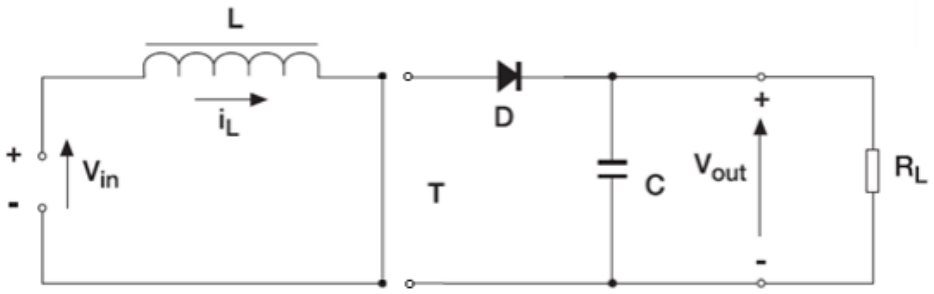

Figure 3.4: Circuit diagram of the boost converter when the switch is turned on

Source: [32]

In the second phase, the switch opens, stopping transistor conduction, and the energy stored in the inductor is transferred to the load via the diode and capacitor. At this point, the inductor pushes the output voltage to a level higher than the input to ensure adequate system power.

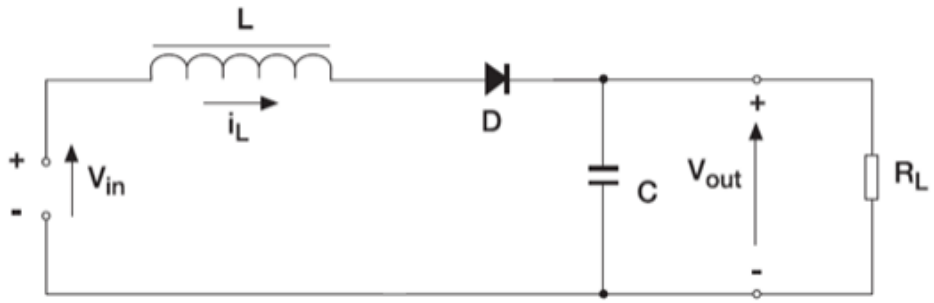

Figure 3.5: Circuit diagram of the boost converter when the switch is turned off

Source: [32]

A key feature of the *boost* converter is its voltage gain—the ratio between the output and input voltages. This gain is controlled by the duty cycle (δ), representing the portion of the switching period when the control signal keeps the switch closed. Typical duty

cycle values range from 0 to 1, providing flexibility in voltage regulation. By adjusting this duty cycle, the converter can increase or decrease output to match the system's power demands, optimizing energy transfer from the panel and supporting stable, reliable operation. This adjustable control over voltage gain is essential for optimizing energy use in photovoltaic applications, where available power fluctuates with sunlight conditions.

The figure 3.2.1 illustrates the behavior of current and voltage in the boost converter in relation to the conduction and cutoff times of the corresponding switch.

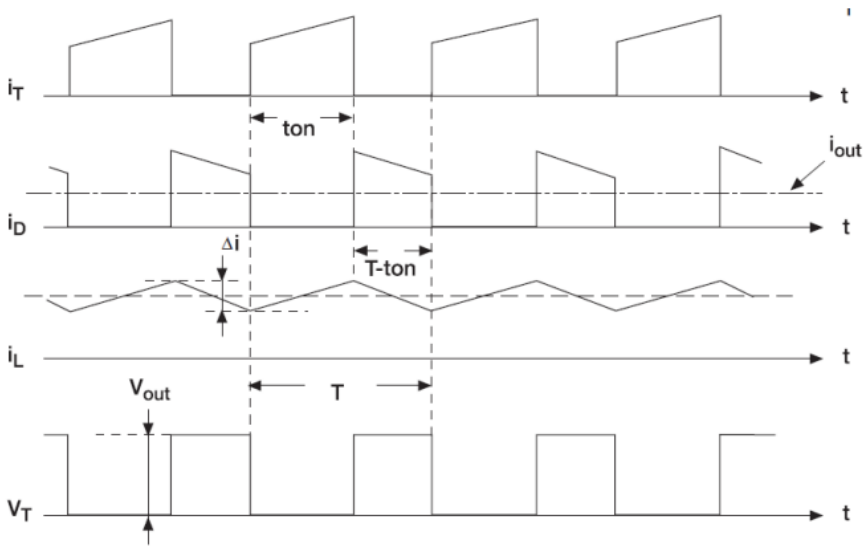

Figure 3.6: Waveforms of current and voltage of the boost converter in steady state

Source: [47]

By controlling the respective intervals of the two previously described phases, we can achieve the desired average output voltage according to the design specifications of the converter. The expression for the voltage across the inductor (V_L) will allow us to deduce the gain of the converter as a function of the duty cycle. This is important because, in steady state, we know that the average value of this voltage is zero ($V_L = 0$).

Here is the expression for $V_L(t)$:

$$V_L(t) = \begin{cases} +V_{in}, & 0 < t < t_{on} \\ +V_{in} - V_{out}, & t_{on} < t < T \end{cases} \tag{3.23}$$

The average value of V_L is determined as follows:

$$\begin{aligned} V_{L_{avg}} = 0 \Leftrightarrow 0 &= \frac{1}{T}\left[\int_0^{t_{on}} V_{in}\, dt + \int_{t_{on}}^{T} (V_{in} - V_{out})\, dt\right] \\ \Leftrightarrow 0 &= \frac{1}{T}\left[\int_0^{\delta T} V_{in}\, dt + \int_{\delta T}^{T} (V_{in} - V_{out})\, dt\right] \\ \Leftrightarrow 0 &= \frac{1}{T}\left[V_{in}\delta T + (V_{in} - V_{out})(T - \delta T)\right] \end{aligned}$$

From this, we can derive the gain of the boost converter:

$$\frac{V_{out}}{V_{in}} = \frac{1}{1-\delta} \tag{3.24}$$

Where the duty cycle (δ) is determined as follows:

$$\delta = \frac{t_{on}}{T} = \frac{t_{on}}{\left(\frac{1}{f}\right)} \tag{3.25}$$

The parameters utilized in the previous equations include the switching frequency f_s measured in hertz [Hz], the switching period T_s expressed in seconds [s], and the input voltage of the converter V_{in} in volts [V]. Additionally, the voltage across the inductor is denoted as V_L (volts [V]), while the average voltage across the inductor is represented as $V_{L_{avg}}$ (volts [V]). The output voltage of the converter is V_{out} (volts [V]), and the duty cycle is represented by δ.

Based on equation 3.24, the graph 3.2.1 illustrates the gain as a function of the duty cycle. This graph allows for a quantitative analysis of the desired output voltage levels of the converter, taking into account the input values.

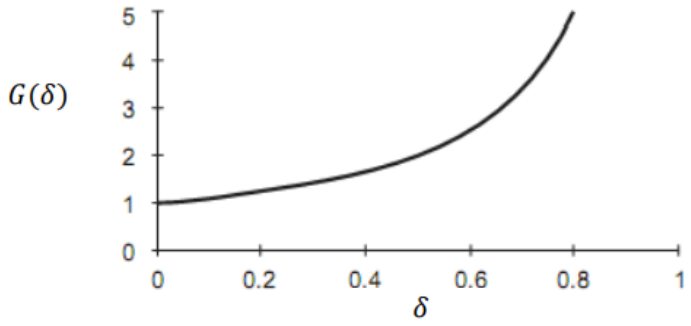

Figure 3.7: Gain of the boost converter as a function of the duty cycle

Source: [47]

In this study, the design of the boost converter will be conducted based on predetermined output voltage levels, with parameters established from nominal operating conditions. Initially, the duty cycle will be determined using the following equation:

$$\delta = 1 - \frac{V_{in}}{V_{out}} \tag{3.26}$$

The next step involves calculating the control voltage (U_c), which will be compared with a carrier wave of amplitude A and frequency f. The resultant signal will control the switch.

$$U_c = A \cdot \delta \tag{3.27}$$

Knowing the input current applied to the converter under reference conditions, we can then obtain the output current using the following equation, allowing us to subsequently determine the load resistance (R_L):

$$I_{out} = (1 - \delta) I_{in} \tag{3.28}$$

$$I_{out} = \frac{V_{out}}{R_L} = \frac{V_{in}}{R_L} \cdot \frac{1}{(1-\delta)} \Rightarrow R_L = \frac{V_{in}}{I_{in}(1-\delta)^2} \tag{3.29}$$

Where I_{in} is the input current of the converter (amperes [A]), I_{out} is the output current of the converter (amperes [A]), and R_L is the load resistance (ohms [Ω]).

Continuing with the design process, it is essential to specify acceptable values for the ripple in the input current (ΔI_{in}) and the output voltage ripple (ΔV_{out}), typically ranging between 10% and 20%. With the previously determined parameters in place, we can now proceed to calculate the remaining components of the converter, specifically the inductor and capacitor. To dimension the inductor, we introduce a variable representing the operating phase of the converter (γ), which allows for the implementation of the differential equation that describes the current behavior in the inductor over time. Assuming a constant output voltage ($V_{out} = V_{o_{av}}$), we can define γ as follows:

$$\gamma = \begin{cases} 0 & \text{for the switching state } D \text{ (when } t_{on} < t < T\text{)} \\ 1 & \text{for the conduction state } D \text{ (when } 0 < t < t_{on}\text{)} \end{cases} \tag{3.30}$$

The differential equation governing the inductor current can be expressed as:

$$\frac{di_L}{dt} = \frac{V_{in} - \gamma V_{out}}{L} \tag{3.31}$$

By integrating both sides of this equation and noting that γ is assigned a value of zero ($\gamma = 0$), we can establish the relationship for the inductor parameter (L), given that $i_L(\gamma \cdot t_{on})$ corresponds to the initial current value at each interval:

$$i_L(t) = \frac{V_{in}}{L}(t - \gamma \cdot \delta T) - \frac{V_{out}}{L}\gamma(t - \delta T) + i_L(t_{on}) \tag{3.32}$$

This can be simplified to:

$$i_L(t) - i_L(\gamma t_{on}) = \frac{V_{in}}{L}(t - \gamma \cdot \delta T) \Rightarrow \Delta i_L = \frac{V_{in}}{L}\delta T \Rightarrow L = \left(\frac{V_{in}}{\Delta i_L}\right)\delta T \tag{3.33}$$

The load resistance (R_o) is directly supplied by the capacitor (C) when the switch is closed, leading us to the following relationship:

$$I_{out} = \frac{V_{out}}{R_L} = -C\frac{d}{dt}V_{out} \tag{3.34}$$

Assuming that V_{out} varies linearly with an initial value of $V_o + \frac{\Delta V_o}{2}$ and that $t = \delta T$, the following expression is derived:

$$I_{out} = -C\frac{d}{dt}V_{out} \Rightarrow \frac{d}{dt}(V_{out}) = -\frac{I_{out}}{C} \Rightarrow V_{out} = \int -\frac{I_{out}}{C}dt \tag{3.35}$$

From this, the relationship becomes:

$$V_{out} = -\frac{I_{out}}{C}t + V_{out} + \frac{\Delta V_{out}}{2} \Rightarrow V_{out} - \frac{\Delta V_{out}}{2} = -\frac{I_{out}}{C}t + V_{out} + \frac{\Delta V_{out}}{2} \tag{3.36}$$

This results in:

$$\frac{I_{out}}{C}\delta T = \Delta V_{out} \Rightarrow C = \left(\frac{I_{out}}{\Delta V_{out}}\right)\delta T \tag{3.37}$$

3.2.2 Quadratic Converter

The quadratic boost converter shown in Figure 3.2.2 is a DC-DC step-up converter designed to amplify voltage, based on the series connection of two boost stages. A key advantage of this configuration is its ability to achieve a quadratic gain in comparison to a traditional single-stage boost converter, meaning it can reach significantly higher output voltages with the same duty cycle. Additionally, this topology simplifies control requirements by using only a single controlled semiconductor switch, enhancing efficiency and reducing the complexity of implementation.

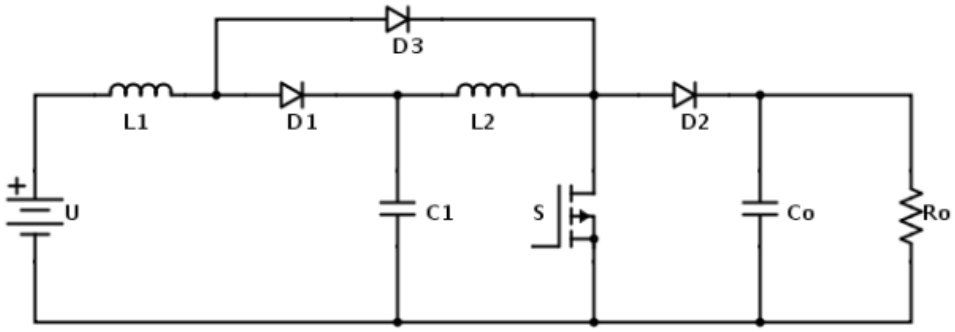

Figure 3.8: Quadratic Converter

Source: [48]

The quadratic boost converter operates through two primary modes based on the state of the MOSFET: conducting (*ON*) or not conducting (*OFF*). While the MOSFET is conducting for a period t_{on}, it remains off for the remainder of the cycle T, defining a duty cycle $\delta = \frac{t_{\text{on}}}{T}$ at a switching frequency $f_{\text{PWM}} = \frac{1}{T}$.

In the ON state, the diodes D_1 and D_2 are reverse-biased and do not conduct, whereas D_3 is forward-biased, allowing capacitor C_0 to supply power to the load, represented by resistance R. During this phase, energy transfer occurs as C_1 charges inductor L_2, and the current through inductor L_1 increases due to the positive applied voltage U. This configuration is illustrated in Figure 3.2.2, with the governing circuit equations detailed as follows:

$$-U + V_{L1} = 0 \Rightarrow V_{L1} = U \tag{3.38}$$

$$-V_{C1} + V_{L2} = 0 \Rightarrow V_{L2} = V_{C1}$$

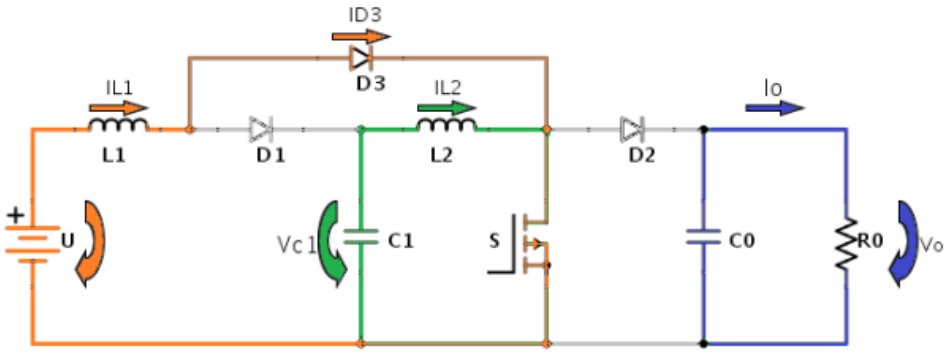

Figure 3.9: Quadratic converter with the MOSFET conducting

Source: [48]

In the OFF phase, the MOSFET is no longer conducting, while D_1 and D_2 now allow current flow, forcing D_3 to switch off. Here, L_1 maintains current flow through D_1, supporting continuous magnetic energy. This configuration, illustrated in Figure 3.2.2, allows the capacitors to recharge. The key equations for this mode are as follows:

$$-U + V_{L1} + V_{C1} = 0 \Rightarrow V_{L1} = U - V_{C1} \tag{3.39}$$

$$-V_{C1} + V_{L2} + V_0 = 0 \Rightarrow V_{L2} = V_{C1} - V_0$$

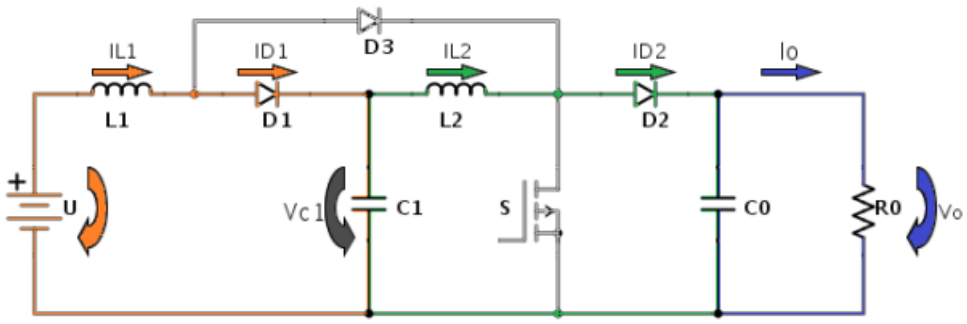

Figure 3.10: Quadratic converter with the MOSFET in cutoff mode

Source: [48]

These two states together describe how the converter's energy management between

inductors and capacitors yields a quadratic voltage gain, achieving high efficiency with only a single controlled switch.

To define the two operational phases of the converter, we introduce a binary variable, γ, which denotes each phase based on the fraction of the switching period T as follows:

$$\gamma = \begin{cases} 1, & 0 < t < T_{\text{on}} \\ 0, & T_{\text{on}} < t < T \end{cases}$$

By associating γ with the previous voltage equations, we obtain:

$$V_{L1} = \begin{cases} U, & \gamma = 1 \\ U - V_{C1}, & \gamma = 0 \end{cases}$$

$$V_{L2} = \begin{cases} V_{C1}, & \gamma = 1 \\ V_{C1} - V_0, & \gamma = 0 \end{cases}$$

To derive the quadratic converter's voltage gain, $\frac{V_0}{U}$, we analyze the circuit in steady-state operation, where the average inductor voltages over a switching period must be zero. This steady-state assumption leads to the following integrals:

$$V_{L1_{\text{avg}}} = \frac{1}{T}\left[\int_0^{\delta T} U\,dt + \int_{\delta T}^{T} (U - V_{C1})\,dt\right] = 0 \tag{3.40}$$

$$V_{L2_{\text{avg}}} = \frac{1}{T}\left[\int_0^{\delta T} V_{C1}\,dt + \int_{\delta T}^{T} (V_{C1} - V_0)\,dt\right] = 0 \tag{3.41}$$

Solving these equations for the input voltage U and output voltage V_0, we find:

$$0 = \frac{1}{T}\left[U\delta T + (U - V_{C1})(T - \delta T)\right] \Rightarrow U = (1 - \delta)V_{C1} \tag{3.42}$$

$$0 = \frac{1}{T}\left[V_{C1}\delta T + (V_{C1} - V_0)(T - \delta T)\right] \Rightarrow V_0 = \frac{V_{C1}}{1 - \delta} \tag{3.43}$$

From these, the voltage gain $\frac{V_0}{U}$ for the quadratic converter is:

$$\frac{V_0}{U} = \frac{\frac{V_{C1}}{1-\delta}}{(1-\delta)V_{C1}} = \frac{1}{(1-\delta)^2} \tag{3.44}$$

where T represents the switching period in seconds, U denotes the input voltage in volts, and V_{C1} is the voltage across capacitor $C1$, also in volts. The terms V_{L1} and V_{L2} indicate the voltages across inductors $L1$ and $L2$, respectively, while V_0 is the output voltage of the converter in volts, and δ is the duty cycle, which characterizes the proportion of time the MOSFET is conducting within each cycle.

Continuing with the quadratic boost converter design, the next step is to calculate the duty cycle (δ) based on predetermined input and output voltage levels. Using equation 3.44, the expression is:

$$\frac{V_o}{U} = \frac{1}{(1-\delta)^2} \Rightarrow \delta = 1 - \sqrt{\frac{U}{V_o}} \tag{3.45}$$

Since this converter is connected directly to a photovoltaic panel, we know the input current I. Using this input, the output current I_o can be found based on the converter's current gain:

$$I_o = I(1-\delta)^2 \tag{3.46}$$

The load resistance R_o is determined with:

$$R_o = \frac{1}{(1-\delta)^2} \cdot \frac{U}{I_o} \tag{3.47}$$

Next, the values for inductors L_1 and L_2 are calculated, factoring in the slight current ripple due to the reactive elements in the circuit. This change is expressed by the differential equations for inductor currents:

$$\frac{di_{L1}}{dt} = \frac{v_{L1}}{L_1}, \quad \frac{di_{L2}}{dt} = \frac{v_{L2}}{L_2} \tag{3.48}$$

During the ON phase (δT_s), where $v_{L1} = U$ and $v_{L2} = \frac{U}{1-\delta}$, the inductor ripple currents

are:

$$\Delta i_{L1} = \frac{U \cdot \delta T}{L_1}, \quad \Delta i_{L2} = \frac{U \cdot \delta T}{(1-\delta)L_2} \tag{3.49}$$

Finally, we can determine values for inductances L_1 and L_2:

$$L_1 = \frac{U\delta}{\Delta i_{L1} f}, \quad L_2 = \frac{U\delta}{(1-\delta)\Delta i_{L2} f} \tag{3.50}$$

These expressions provide the necessary parameters to achieve efficient operation in the converter's reactive components.

In the process of determining the capacitive elements, we start by calculating the output capacitor C_o, which directly supplies the load resistance R_o when the switch (S) is closed. The relationship is given by the following expressions:

$$I_o = \frac{V_o}{R_o} \tag{3.51}$$

$$I_{C_o} = C_o \frac{d}{dt} v_o \quad \Rightarrow \quad I_o = I_{C_o} \quad \Rightarrow \quad \frac{V_o}{R_o} = C_o \frac{d}{dt} v_o \tag{3.52}$$

Assuming that v_o changes slowly over the period T, we can approximate the variation of v_o as linear around its average value, yielding:

$$\frac{V_o}{R_o} = C_o \frac{\Delta v_o}{\Delta t} \quad \Rightarrow \quad C_o = \frac{V_o \Delta t}{R_o \Delta v_o} \quad \Rightarrow \quad C_o = \frac{V_o \delta T}{R_o \Delta v_o} \tag{3.53}$$

This results in:

$$C_o = \frac{U\delta}{(1-\delta)^2 R_o \Delta v_o f} \tag{3.54}$$

Next, for the capacitor C_1, we base our calculation on the differential equation describing the current behavior in the capacitor, which is identical to that in inductor L_2 when the switch (S) is closed:

$$i_{C_1} = i_{L_2} = C_1 \frac{dV_{C_1}}{dt} = C_1 \frac{\Delta v_{C_1}}{\Delta t} \tag{3.55}$$

Using this equation and considering the current through inductor L_2 in terms of output current I_o, we obtain the equation for calculating the capacitance of C_1. The average current in inductor L_2, considering that the switch is open ($\gamma = 0$, $t = (1-\delta)T$), leads to the following relationship:

$$I_{L_2} = \begin{cases} I_{C_1} & \text{for } 0 < t < T_{on} \\ I_{L_1} - I_{C_1} & \text{for } T_{on} < t < T_s \end{cases} \tag{3.56}$$

From this relationship, the following expression is obtained:

$$I_{L_2} = (1-\delta) I_{L_1} \quad \Rightarrow \quad I_{L_2} = (1-\delta) I \quad \Rightarrow \quad I_{L_2} = \frac{1}{(1-\delta)} I_o \tag{3.57}$$

Thus, the current in capacitor C_1 is:

$$i_{C_1} = i_{L_2} \quad \Rightarrow \quad C_1 \frac{\Delta v_{C_1}}{\Delta t} = \frac{1}{(1-\delta)} I_o \quad \Rightarrow \quad C_1 \frac{\Delta v_{C_1}}{\Delta t} = \frac{V_o}{R_o}(1-\delta) \tag{3.58}$$

This leads to:

$$C_1 = \frac{\delta U}{(1-\delta)\Delta v_{C_1} R_o f} \tag{3.59}$$

3.3 Maximum Power Point Tracking (MPPT)

This section outlines the control strategies employed to optimize the performance of the converters, with a focus on the techniques used for Maximum Power Point Tracking (MPPT). To ensure the system operates efficiently and stably under varying environmental conditions, four primary MPPT methods are utilized. These methods are essential for adjusting the system's operation, ensuring that it consistently performs at its best

and maximizes energy extraction. Each control method addresses specific aspects of the converter's behavior, contributing to the overall optimization of the system.

In scientific literature, various MPPT techniques have been proposed, all of which are influenced by fluctuations in solar irradiance throughout the day. The dynamic performance of these algorithms can be simulated and evaluated using mathematical models of photovoltaic (PV) panels implemented in specialized software. These models provide valuable insights into the behavior of PV systems under different environmental conditions, enabling further optimization of energy extraction.

This study focuses on four distinct MPPT methods, which are explored in detail: Fixed Duty Cycle (Fixed Duty Cycle (D)), Constant Voltage (Constant Voltage (Vcte)), Perturb and Observe (Perturb and Observe (P&O)), and Incremental Conductance (Incremental Conductance (IC)). Each method plays a crucial role in improving the performance and efficiency of the system by adapting to the changing conditions of the solar environment.

All MPPT algorithms are modeled using the computational tool Matlab/Simulink®. These models are then discussed and presented in the following section.

3.3.1 Fixed Duty Cycle (D)

The Fixed Duty Cycle method is the simplest MPPT technique, as it does not require any feedback or real-time adjustments. This method sets the load impedance to match the Maximum Power Point (MPP) at a single predetermined value. Once configured, the duty cycle remains constant, with no consideration for variations in environmental conditions such as temperature or solar irradiance.

Due to its inherent inefficiency and inability to adapt to changing conditions, the Fixed Duty Cycle method is not commonly used in practical applications. However, it is often employed as a baseline or reference for comparison, representing the worst-case scenario against which the performance of other, more advanced MPPT methods can be evaluated.

3.3.2 Constant Voltage (Vcte)

The Constant Voltage (Vcte) method was implemented in Matlab/Simulink to track the Maximum Power Point (MPP) of the photovoltaic (PV) panel. The Vcte technique operates by maintaining the panel's operating voltage close to a predefined reference voltage, typically the voltage at the Maximum Power Point (Vmpp), under standard test conditions.

The PV panel's voltage (Vpv) was used as the input to a custom function implemented in MATLAB code. The function computes the duty cycle (Duty) based on the difference between the measured voltage (Vpv) and the reference voltage (Vref).

By analyzing the circuit corresponding to the converter's output (Figure 3.11), regardless of the converter type, the capacitor current (i_{Co}) is obtained:

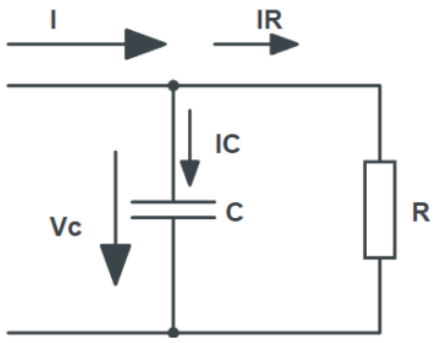

Figure 3.11: Converter output circuit

Source: [49]

The switched converters, designed to meet specific sizing requirements and supply a load with the desired voltage and current, require closed-loop control. This control is managed through the operation of the switches, which open and close based on the input current, regardless of the load conditions. This method, often called voltage control, leverages the output voltage's slower dynamics compared to the input current. Consequently, output voltage control is adjusted through input current variations. Analyzing the output circuit of the converter, shown in Figure 3.14, yields the capacitor current (i_{co}):

$$i_{co} = C_o \frac{dv_{\text{out}}}{dt} = I - I_o \tag{3.60}$$

By substituting I with the inductor current i_L, which is controlled according to the converter's gain $\left(\frac{V_{\text{out}}}{V_{\text{in}}}\right)$, the resulting expression is:

$$C_o \frac{dv_{\text{out}}}{dt} = \frac{V_{\text{in}}}{V_{\text{out}}} i_L - I_o \tag{3.61}$$

Applying the Laplace transform to the equation above and rearranging for the output voltage v_{out}, the following expression is derived:

$$sC_o v_{\text{out}} = \frac{V_{\text{in}}}{V_{\text{out}}} i_L - i_o \Rightarrow v_{\text{out}} = \frac{\left(\frac{V_{\text{in}}}{V_{\text{out}}}\right) i_L - i_o}{sC_o} \tag{3.62}$$

Considering that v_{out} changes very slowly over time, as it is a DC voltage that is intended to remain nearly constant, it follows that the gain must also remain almost constant. By analogy with equation 3.62, the block diagram of the voltage control system can be represented, taking into account the compensator in the closed-loop configuration and the unitary feedback gain (H), as follows:

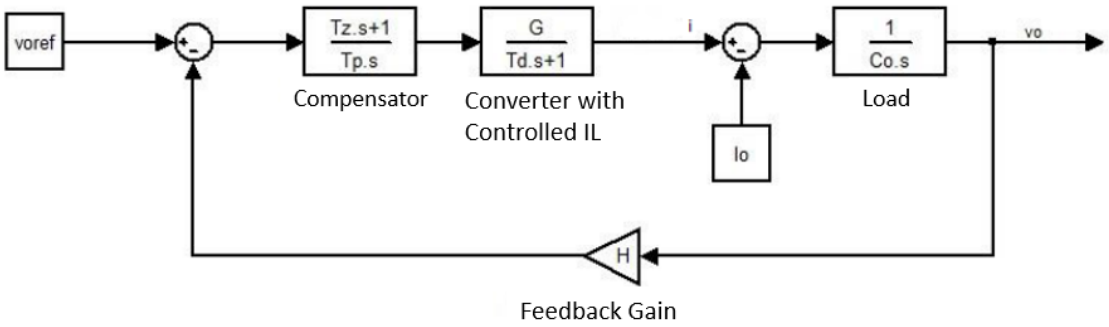

Figure 3.12: Block diagram with a proportional-integral controller for voltage control

Source: adapted from [48]

As can be observed in a closed-loop system, the output signal is used to determine the control signal to be applied at a specific moment, where the output signal is compared to a reference signal, resulting in an error signal. This error signal is then processed to

provide an accurate response to external disturbances. The error signal will be fed into a PI compensator, which in turn will provide the effective value of the reference current (i_{Lref}).

The primary advantage of the Constant Voltage method lies in its simplicity and minimal sensor requirements. It only requires voltage sensing at the output of the PV module, significantly reducing hardware complexity and cost. Furthermore, its computational requirements are low, making it well-suited for systems with limited processing power.

However, the Vcte method operates on the assumption that the Vmpp remains relatively constant, regardless of environmental variations such as changes in temperature and solar irradiance. This simplification means that the method does not dynamically adapt to these factors, which can result in suboptimal performance in rapidly changing conditions. While this limitation does not affect the method significantly in stable environments, it can lead to efficiency losses in systems subjected to frequent or significant environmental fluctuations.

3.3.3 Perturb and Observe (P&O)

The Perturb and Observe (P&O) method is one of the most widely used techniques for Maximum Power Point Tracking (MPPT) due to its simplicity and ease of implementation. This method operates by periodically perturbing the voltage of the photovoltaic (PV) panel and observing the resulting changes in power. Based on these observations, the system adjusts the operating point of the panel to maximize power extraction.

The P&O algorithm works by analyzing the power-voltage (P-V) curve of the PV system. According to the behavior of the curve, if the panel is operating to the right of the Maximum Power Point (MPP), decreasing the voltage will increase the power. Conversely, if the panel is operating to the left of the MPP, increasing the voltage will increase the power. Starting from a given operating point, the algorithm perturbs the voltage (increases or decreases it by a fixed step size, ΔV) and compares the resulting power (P)

to the previous power measurement. If the power increases, the perturbation continues in the same direction; otherwise, the algorithm reverses the direction of perturbation [50].

The mathematical representation of the process is expressed as:

$$\Delta V = V_t - V(t - \Delta t) \tag{3.63}$$

$$\Delta P = P_t - P(t - \Delta t) \tag{3.64}$$

Based on these variations:

- If $\Delta V > 0$ and $\Delta P > 0$, or $\Delta V < 0$ and $\Delta P < 0$, the algorithm perturbs the voltage in the same direction, indicating operation to the left of the MPP.
- If $\Delta V > 0$ and $\Delta P < 0$, or $\Delta V < 0$ and $\Delta P > 0$, the algorithm reverses the perturbation direction, indicating operation to the right of the MPP [51].

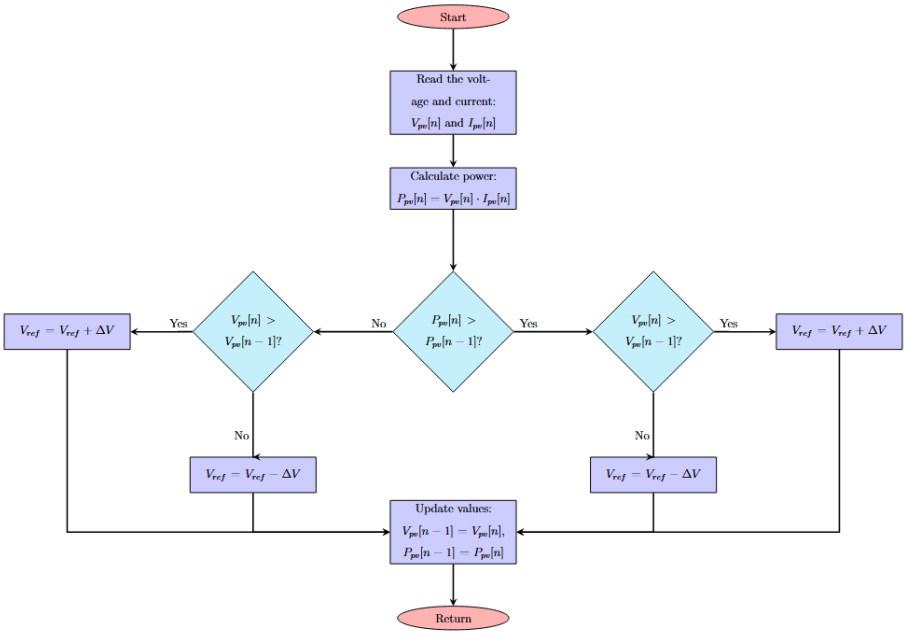

Figure 3.13: Flowchart of the Perturb and Observe (P&O) algorithm, which adjusts the reference voltage (V_{ref}) by observing changes in power (P_{pv}) and voltage (V_{pv}) to track the Maximum Power Point (MPP)

This method is popular due to its simplicity, as it only requires measurements of the PV panel's voltage and current, with no additional parameters or complex control structures. However, it does present certain limitations. Under conditions of low irradiance, the algorithm may cause significant oscillations around the MPP, reducing system efficiency. Furthermore, in scenarios where irradiance changes rapidly, the algorithm may initially select the incorrect direction, leading to slower convergence to the true MPP. The step size ΔV plays a crucial role in the algorithm's performance: smaller steps reduce oscillations but increase the time required for tracking, while larger steps improve response time at the cost of higher oscillations [50], [51].

Despite its limitations, the P&O method remains a benchmark MPPT technique due to its straightforward implementation and reliable performance under stable environmental conditions. It continues to be a key reference point for comparing the efficiency and responsiveness of more advanced MPPT algorithms.

3.3.4 Incremental Conductance (IC)

The primary goal of the MPPT technique is to continuously extract and deliver the maximum possible power from the photovoltaic panel to the load. This is achieved by identifying the voltage and current values that correspond to the maximum power point at any given time. Among various MPPT algorithms, the Incremental Conductance method calculates the derivative of power with respect to voltage, adjusting the duty cycle accordingly. If the derivative is positive, the system is below the maximum power point, so the duty cycle is increased. Conversely, if the derivative is negative, the system is beyond the maximum power point, prompting a reduction in the duty cycle. The maximum power point corresponds to the point where the power vs. current curve reaches its peak, with the derivative at that point being zero.

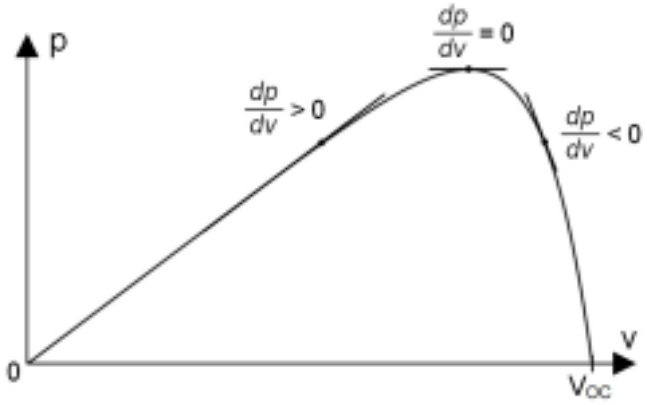

Figure 3.14: Variation of the $\frac{dp}{dv}$ signal as a function of power and voltage

Source: [52]

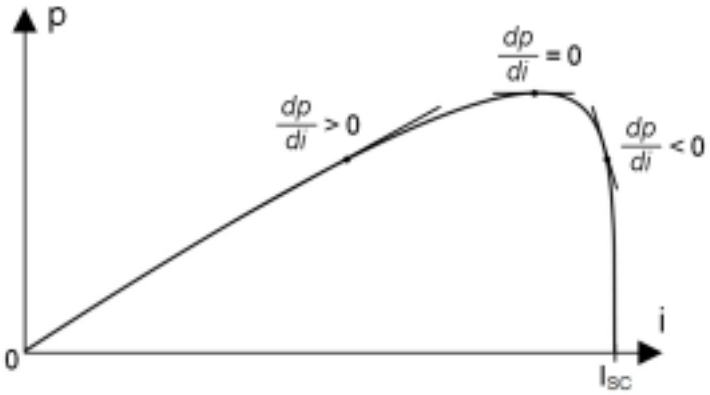

Figure 3.15: Variation of the $\frac{dp}{di}$ signal as a function of power and current

Source: [52]

In the Incremental Conductance method, the goal is to adjust the duty cycle such that the derivative of power with respect to voltage approaches zero. The derivative of power can be expressed as:

$$\frac{dP}{dV} = \frac{d(VI)}{dV} = I\frac{dV}{dV} + V\frac{dI}{dV} = I + V\frac{dI}{dV} \tag{3.65}$$

By simplifying this expression, we get:

$$\frac{dP}{dV} = I + V\frac{(i(t) - i(t-1))}{(v(t) - v(t-1))} \tag{3.66}$$

The maximum power point is determined by setting this derivative equal to zero:

$$\frac{dP}{dV} = 0 \quad \Rightarrow \quad I + V\frac{(i(t) - i(t-1))}{(v(t) - v(t-1))} = 0 \quad \Rightarrow \quad I = -V\frac{(i(t) - i(t-1))}{(v(t) - v(t-1))} \tag{3.67}$$

The variables $v(t-1)$ and $i(t-1)$ represent the voltage and current values measured at the previous time instant. The derivative of power with respect to voltage is positive when the operating point is to the left of the maximum power point. This indicates that the power at that instant is less than the maximum power the photovoltaic panel can generate. Conversely, when the derivative is negative, the operating point is to the right of the maximum power point. Ideally, the derivative of power with respect to voltage should be zero, which corresponds to the maximum power point.

To achieve this, current control in the inductor is performed by adjusting the duty cycle of the switch. If the derivative of power is positive, the MPPT will need to increase the current in the inductor, which means increasing the duty cycle (i.e., the switch is closed for a longer period, $\gamma = 1$). The control conditions are governed by the following rules:

$$\frac{dP}{dV} > 0 \Rightarrow I < I_{\text{mp}} \Rightarrow I \text{ needs to increase} \Rightarrow \gamma = 1 \tag{3.68}$$

$$\frac{dP}{dV} < 0 \Rightarrow I > I_{\text{mp}} \Rightarrow I \text{ needs to decrease} \Rightarrow \gamma = 0 \tag{3.69}$$

$$\frac{dP}{dV} = 0 \Rightarrow I \approx I_{\text{mp}} \Rightarrow I \text{ remains constant} \Rightarrow \gamma = \gamma(t-1) \tag{3.70}$$

The operation of the MPPT can be outlined through the following flowchart:

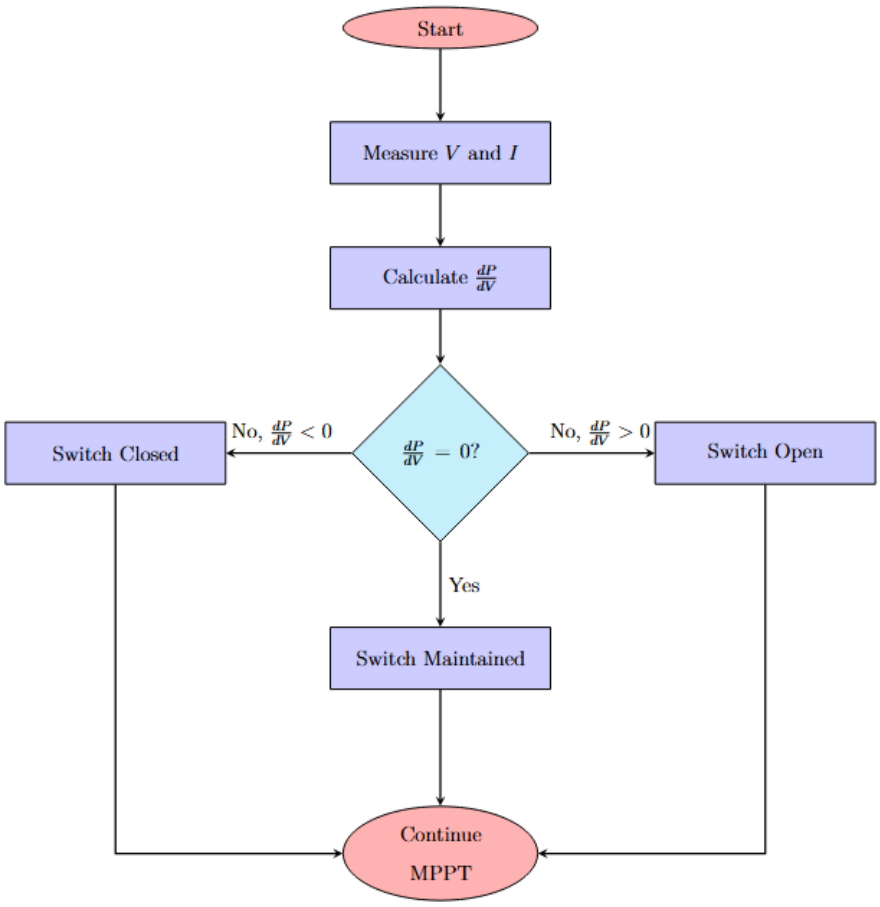

Figure 3.16: Flowchart illustrating the MPPT algorithm, where the system adjusts the switch based on the derivative of power with respect to voltage to maximize power output.

3.4 Energy Storage System

For the analysis of the battery system in this dissertation, the Lithium-Ion HE341440 NCA cell from EAS Batteries GmbH was chosen, as the technical specifications of the Volvo BZL Electric, the bus under study, indicate that the batteries in the system use NCA (Nickel Cobalt Aluminum) chemistry. This choice was made to approximate the real-world conditions of the vehicle, as the NCA chemistry is consistent with that used in the bus's battery system. However, it is important to note that the HE341440 NCA cell

is not the exact cell used in the Volvo BZL Electric, but rather a representative model selected for its similar chemistry. This allows for a more detailed and relevant analysis of the battery behavior in the context of the electric bus system.

3.4.1 Mathematical Model

In the literature, battery modeling is commonly divided into three primary approaches: experimental, electrochemical, and electrical circuit-based models. While experimental and electrochemical models offer valuable insights, they are often not the best choice for accurately estimating the state-of-charge (SOC) of battery packs. On the other hand, electrical circuit-based models have proven to be effective in capturing the electrical behaviors of batteries. The simplest of these models typically includes an ideal voltage source connected in series with an internal resistance, providing a straightforward representation of battery dynamics for practical applications [53].

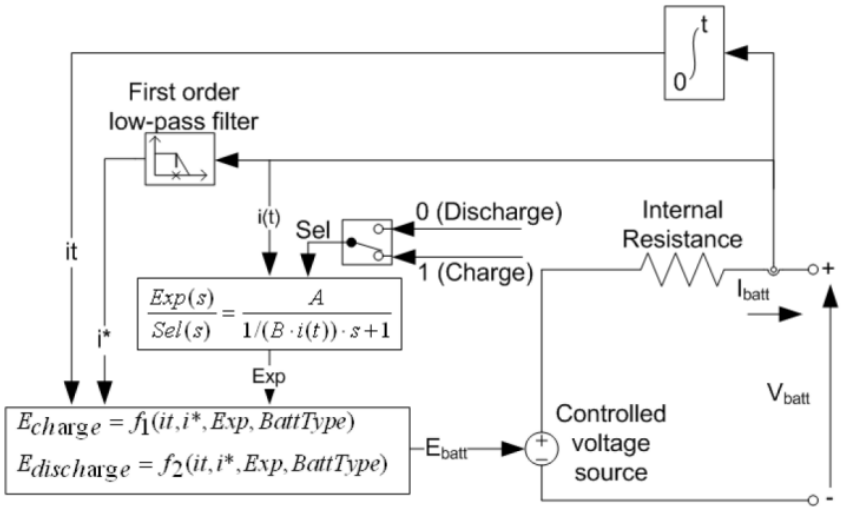

Figure 3.17: Simple model of a lithium-ion battery

Source: [53]

The voltage source is determined by nonlinear equations based on the actual state of charge (SOC) of the batteries, where the following applies:

For the discharge model ($i^* > 0$):

$$f_1(it, i^*, i) = E_0 - K\left(\frac{Q}{Q - it}\right)i^* - K\left(\frac{Q}{Q - it}\right)it + A^{-Bit} - Bit \tag{3.71}$$

For the charge model ($i^* < 0$):

$$f_2(it, i^*, i) = E_0 - K\left(\frac{Q}{it + 0.1 \cdot Q}\right)i^* - K\left(\frac{Q}{Q - it}\right)it + A^{-Bit} - Bit \tag{3.72}$$

The parameters used in the equations are as follows: A represents the exponential voltage, measured in volts (V); B refers to the exponential capacity, with units of Ampere-hour inverse (Ah^{-1}); E_0 is the constant voltage, also in volts (V); E_{bat} denotes the non-linear source voltage, measured in volts (V); i is the battery current, given in amperes (A); i^* represents the low-frequency dynamic current, measured in amperes (A); it is the extracted capacity, measured in Ampere-hours (Ah); K is the polarization constant, measured in Ampere-hour inverse (Ah^{-1}) or the polarization resistance in ohms (Ω); Q is the maximum battery capacity, given in Ampere-hours (Ah); and Sel represents the mode of the battery, where $Sel(s) = 0$ during discharge and $Sel(s) = 1$ during charge.

The internal resistance, as depicted in the model (Figure 3.17), represents the resistance along the metallic path within the battery. This includes the cell terminals, electrodes, and connections, while also considering the resistance of the electrolyte and separator path. Depending on the type of battery, the parameters of the equivalent circuit can be adjusted, and this requires a clear understanding of the discharge characteristics. These characteristics are typically represented by a discharge curve, which can be divided into three distinct sections, as shown in the figure below:

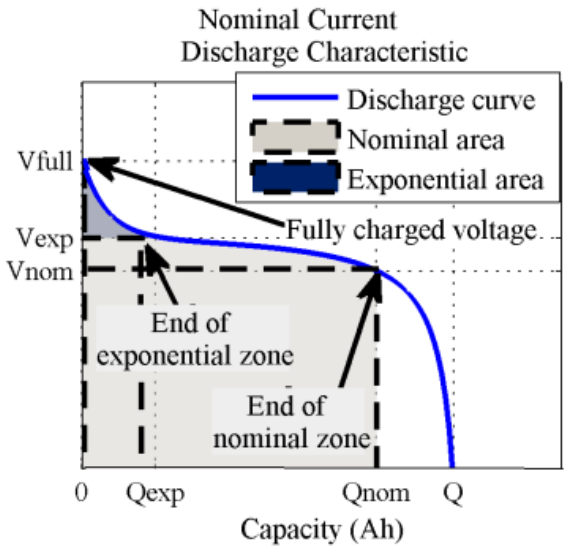

Figure 3.18: Typical discharge curve

Source: [54]

The first section of the curve represents the exponential voltage drop that occurs when the battery is initially charged. The second section describes the battery's ability to deliver charge until the voltage reaches its nominal value. The third section shows the final stage of discharge, characterized by a rapid voltage decline as the battery is drained. The extent of each section can vary depending on the specific type of battery being used.

It is important to highlight that the model parameters are derived from the discharge characteristics and are applicable to the charging process as well.

The following tables present the nominal and pack characteristics of the NCA cells and their configurations used in the battery system under analysis. These characteristics are essential for understanding the performance and energy capacity of the system. The calculations for these tables were derived from the specifications of the NCA cell and its configuration in series and parallel, which are key parameters for determining the overall voltage, capacity, and energy storage. The values presented here are based on the nominal parameters of the individual cells, the configuration of the cells within the modules, and the arrangement of modules within the pack. The data provides a comprehensive overview

of the battery system's performance and will serve as the foundation for further analyses.

Table 3.2: Nominal Characteristics of NCA Cell

Parameter	Value
Nominal Voltage	3.6 V
Nominal Capacity	10 Ah
Nominal Current	5 A

The 181s14p configuration was chosen to closely match the battery used in the real Volvo BZL Electric model. This electric bus model features a battery with the following characteristics, as described in the datasheet for the Volvo BZL (available in the appendix): the available storage energy (battery capacity) is 94 kWh, the battery chemistry type is Lithium-ion, NCA, and the voltage is 600V. The available storage energy for 3 to 5 batteries is between 282 kWh and 470 kWh. Based on this information, the 181s14p configuration (181 cells in series and 14 cells in parallel) was selected to meet the voltage and energy storage requirements similar to those of the real battery used in the Volvo BZL Electric model.

Table 3.3: Pack Characteristics of NCA Modules (181s14p)

Parameter	Value
Pack Configuration	181s14p (181 cells in series, 14 cells in parallel)
Nominal Voltage	651,60 V
Nominal Capacity	140 Ah
Energy Storage	91,22 kWh
Total Number of Cells	2534 cells

This configuration was chosen to provide a nominal voltage of 651.60 V, which aligns with the operational needs of large electric vehicles like the Volvo BZL. The nominal capacity of 140 Ah and the stored energy of 91.22 kWh are also suitable for simulating a performance compatible with the battery specifications of the Volvo BZL.

A key advantage of the chosen mathematical model is the simplicity with which dynamic parameters can be extracted and calculated directly from the discharge curve provided by the manufacturer, eliminating the need for additional experimental testing on the battery. Only three fixed points on the steady-state discharge curve are required to configure the model, allowing the calculation of parameters such as fully charged voltage V_{full}, the exponential zone limits V_{exp} and Q_{exp}, nominal voltage V_{nom}, nominal capacity Q_{nom}, and total capacity Q. These parameters, extracted from the EAS Batteries discharge curve for the selected cell, are identified according to the x and y axes and are illustrated in Figure 3.19, in alignment with Lopes (2016) [53].

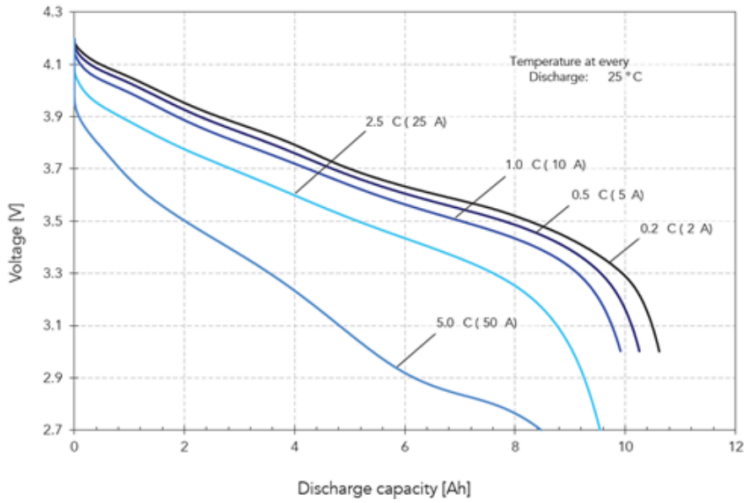

Figure 3.19: Characteristic discharge curve of the selected battery, manufactured by EAS Batteries

Source: [55]

To determine the parameters of the model for the selected battery, values were extracted from the discharge curve provided by EAS Batteries. These extracted values are presented in Table 3.4 [53].

Table 3.4: Battery Discharge Curve Parameters

Parameter	Value
V_{full}	4.2 V
V_{exp}	3.9 V
Q_{exp}	2 Ah
V_{nom}	3.6 V
Q_{nom}	10 Ah
Q	10.8 Ah

First, the amplitude of the exponential zone, A, can be calculated as follows:

$$A = V_{\text{full}} - V_{\text{exp}} \tag{3.73}$$

Next, the exponential capacity, B, is calculated with:

$$B = \frac{3}{Q_{\text{exp}}} \tag{3.74}$$

The polarization voltage, K, is derived from V_{full}, V_{nom}, and Q_{nom}:

$$K = \frac{V_{\text{full}} - V_{\text{exp}} + A(e^{-BQ_{\text{nom}}} - 1)(Q - Q_{\text{nom}})}{Q_{\text{nom}}} \tag{3.75}$$

The nominal current, I_{nom}, for which the discharge curve was measured, is approximately 43.5% of the nominal capacity:

$$I_{\text{nom}} = Q \times 0.435 \tag{3.76}$$

The internal resistance, R, is estimated at 1% of the nominal power:

$$P_{\text{nom}} = V_{\text{nom}} \times Q_{\text{nom}} \tag{3.77}$$

$$R = 0.01 \times \frac{V_{\text{nom}}^2}{P_{\text{nom}}} \tag{3.78}$$

Lastly, the constant voltage of the battery, E_0, is calculated as:

$$E_0 = V_{\text{full}} + K + R \cdot I_{\text{nom}} - A \tag{3.79}$$

The parameters calculated provide an approximate model, with accuracy dependent on the precision of the values obtained from the discharge curve.

Given the configuration of cells in series and parallel, the calculated parameters need to be adjusted for the full battery pack, the global parameters for the battery rack are obtained as follows:

$$V_{\text{nom\_pack}} = N_{\text{ser}} \times V_{\text{nom}} \tag{3.80}$$

For internal resistance R, considering that there are N_{par} cells in parallel:

$$R_{\text{pack}} = R \times \frac{N_{\text{ser}}}{N_{\text{par}}} \tag{3.81}$$

The nominal current $I_{\text{nom\_pack}}$, scaled for the parallel configuration, is:

$$I_{\text{nom\_pack}} = N_{\text{par}} \times I_{\text{nom}} \tag{3.82}$$

The constant voltage E_{0_pack}, for the entire series configuration:

$$E_{0\_\text{pack}} = N_{\text{ser}} \times E_0 \tag{3.83}$$

These values provide the necessary parameters for modeling the battery pack's performance. Table 3.3 summarizes the global characteristics, confirming the power and energy storage capacities of the battery pack.

3.4.2 Limitations and Assumptions

The mathematical model presented is valid under specific conditions and assumptions, which are outlined as follows [54]:

Limitations

- The minimum no-load battery voltage is set to 0 V, and the maximum battery voltage is limited to $2 \times E_0$. This ensures the voltage stays within realistic operational bounds.

- The minimum capacity of the battery is 0 Ah, and the maximum capacity is $Q_{\max}$. As a result, the maximum State of Charge (SOC) cannot exceed 100% if the battery is overcharged, reflecting the practical limits of battery operation.

Assumptions

- The internal resistance of the battery is assumed to be constant during both charge and discharge cycles, and does not vary with the amplitude of the current. This simplification ensures that the model remains manageable while avoiding the complexity of variable resistance.

- The model parameters are derived from the discharge characteristics provided by the manufacturer. It is assumed that these parameters are applicable during both charging and discharging, simplifying the analysis by treating both processes as equivalent.

- The battery's capacity is assumed to remain constant regardless of the amplitude of the current, implying no Peukert effect. In this model, the capacity does not decrease with higher discharge rates, which is a typical assumption for ideal battery models.

- The self-discharge of the battery is not represented in the model. This effect can

be modeled separately by adding a large resistance in parallel with the battery terminals, but is neglected for simplicity in this context.

- The battery is assumed to have no memory effect, meaning that its capacity does not degrade based on previous charge/discharge cycles. This assumption holds for modern lithium-ion batteries, which do not exhibit significant memory effects.

These assumptions and limitations are made to simplify the model and provide a more tractable approach for simulating the battery's performance. However, they may not fully capture the complexities of real-world battery behavior, and deviations from these idealized conditions should be considered in practical applications.

Chapter 4

Development

This chapter presents the development process of the photovoltaic system, covering the design and simulation of its main components. The study includes the sizing and analysis of the photovoltaic module, the design and implementation of power converters, and the selection of the battery pack.

Initially, the characteristics and mathematical modeling of the photovoltaic module are discussed, followed by the simulation of its current-voltage (I-V) and power-voltage (P-V) curves under standard test conditions. Subsequently, the design of DC-DC converters is introduced, focusing on both boost and quadratic converter topologies, with calculations for key electrical parameters. Finally, the characteristics of the selected battery pack are presented, including essential parameters for energy storage and system efficiency.

To complement the development process, the MATLAB code used for simulations and calculations is provided in the appendix B. This ensures transparency and reproducibility of the results obtained throughout the study.

4.1 Photovoltaic Module

4.1.1 Module Design

The sizing of the photovoltaic module utilized in this study is presented herein. Building upon the previously established theoretical model, the calculations necessary to determine the relevant quantities and parameters associated with the module's performance will be conducted. For the purpose of these calculations, a solar irradiance (G) of 1000 $\mathrm{W/m^2}$ and an ambient temperature (θ_{amb}) of 25 $^\circ C$ will be considered. These values are essential for ensuring the accuracy of the results and the appropriateness of the analyses performed. Subsequently, the calculation spreadsheet detailing the sizing process and the results obtained will be presented.

Table 4.1: Calculated Parameters for the HG-L530-72CW Panel

Parameter	Equation	Value
G	—	1000 $\mathrm{W/m^2}$
G_{ref}	—	1000 $\mathrm{W/m^2}$
T_{ref}	3.8;3.9	298.15 K
T_{FV}	3.8	304.40 K
V_{T}	3.3	0.026 V
V_{Tref}	3.4	0.0257 V
m	3.12	123.56
m'	3.13	5.15
I_{or}	3.10	2.039×10^{-6} A
I_{o}	3.14	2.169×10^{-6} A
R_{sh}	3.19	45.84 Ω
R_{s}	3.20	0.98 Ω
I_{sc}	3.15	13.76 A
I_{ph}	3.16	14.05 A

4.1.2 Simulation of Photovoltaic Panel Characteristics (I-V and P-V Curves)

The following simulation illustrates the characteristic current-voltage (I-V) and power-voltage (P-V) curves of a photovoltaic panel, generated using MATLAB. The simulation provides insights into the panel's performance under standard test conditions, with irradiance $G = G_{\text{ref}} = 1000\,\text{W/m}^2$ and temperature $T = T_{\text{ref}} = 25°\text{C}$.

The plots of the I-V and P-V curves were generated based on the panel's physical parameters and standard environmental conditions. These plots illustrate the expected performance of the panel by considering factors such as temperature and irradiance, which influence its voltage and current characteristics.

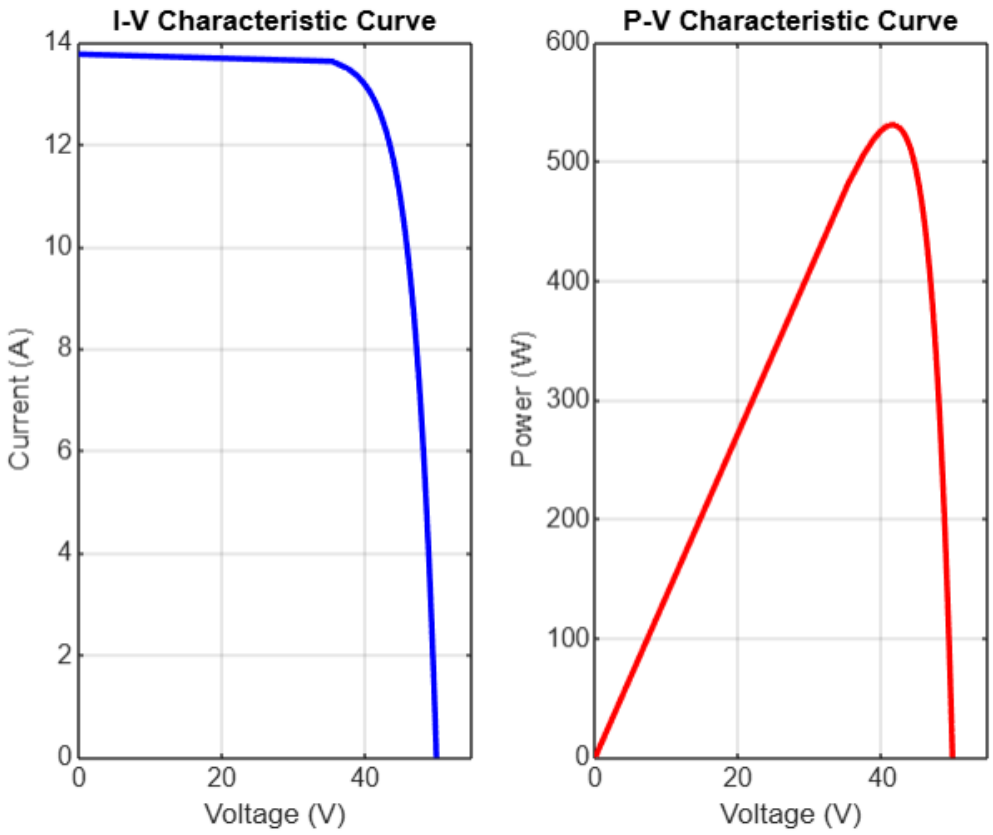

Figure 4.1: Simulation of Photovoltaic Panel (I-V and P-V Curves)

4.2 Converters

4.2.1 Boost converter Design

In this section, we present the results from the design calculations for the boost converter. These results reflect the key parameters necessary for the converter's effective operation, derived from the specified input and output requirements. The calculations encompass essential elements such as input voltage, output voltage, duty cycle, and other related electrical characteristics. By analyzing these parameters, we can ensure that the converter will perform efficiently under the desired operational conditions, ultimately achieving the targeted performance goals.

Table 4.2: Results of the Boost Converter Sizing

Parameter	Equation	Value
V_{in}	—	41.35 V
V_{out}	—	700 V
δ	3.26	0.9409
I_{in}	—	12.83 A
I_{out}	3.28	0.76 A
R_L	3.29	923.62 Ω
L	3.33	38.9 mH
C	3.37	0.7 mF

4.2.2 Quadratic converter Design

The design of the quadratic converter involves selecting key components based on voltage, current, and efficiency requirements. The following table summarizes the calculated values for the primary parameters, including the input voltage (U), output voltage (V_o), inductances (L_1 and L_2), and capacitances (C_o and C_1), which are essential for achieving optimal converter performance and stability.

The inductive elements were calculated assuming a switching frequency (f_s) of 10 kHz, leading to a switching period (T_s) of 0.1 ms and a current ripple ($\Delta i_{L_{in}}$) of 0.1 A. Similarly, for the capacitive elements, the same switching frequency was used, resulting in a period of 0.1 ms and a voltage ripple (Δv_{out}) of 0.1 V.

Table 4.3: Results of the Quadratic Converter Sizing

Parameter	Equation	Value
U	—	41.35 V
V_o	—	700 V
δ	3.45	0.757
I	—	12.83 A
I_o	3.46	0.758 A
R_o	3.47	923.62 Ω
L_1	3.50	31.3 mH
L_2	3.50	128.78 mH
C_o	3.54	0.573 mF
C_1	3.59	0.139 mF

4.3 Battery Used in the Study

The table presented below summarizes the calculated parameters for the selected battery pack. These values were derived from the discharge curve and the configuration of the battery cells. The parameters include key characteristics such as nominal voltage, internal resistance, nominal current, and constant voltage, both for individual cells and the complete pack. The table serves to provide a comprehensive overview of the battery's performance characteristics, essential for modeling its behavior and assessing its overall efficiency and energy storage capacity.

Table 4.4: Calculation of Parameters for the Battery Pack

Cell Parameters		
Parameter	Equation Number	Calculated Value
A	3.73	0.3 V
B	3.74	1.5 Ah^{-1}
K	3.75	0.0060 V
I_{nom}	3.76	4.70 A
R	3.78	0.0036 Ω
E_0	3.79	3.92 V
Pack Parameters		
$V_{\text{nom\_pack}}$	3.80	651.60 V
R_{pack}	3.81	0.046 Ω
$I_{\text{nom\_pack}}$	3.82	65.77 A
E_{0_pack}	3.83	710.05 V

Chapter 5

Tests and Results

This chapter presents and analyzes the results of simulations conducted to evaluate the performance of Boost and Quadratic converters in photovoltaic systems, employing various Maximum Power Point Tracking (MPPT) techniques. The comparative analysis considers four MPPT methods: incremental conductance, perturb and observe, constant voltage, and duty cycle control, with the latter serving as the baseline to assess the worst-case performance scenario.

To ensure practical applicability, the system design and simulation parameters were tailored to the operational constraints of an electric bus, specifically the Volvo BZL Electric. This included configuring the photovoltaic system to maximize energy capture within the limited rooftop area, using an arrangement of 11 modules connected in series to achieve a nominal voltage of approximately 454.85 V. The system was paired with a 600 V battery, aligning with the specifications needed for high-efficiency electric bus operations.

The environmental performance of the system was evaluated using irradiance and temperature profiles sourced from PVGIS for Curitiba, Brazil. Two representative periods were chosen: June, which marks the lowest solar incidence, and December, the peak of solar availability. This seasonal contrast provided valuable insights into the operational reliability and energy generation capabilities of the photovoltaic array, enabling a comprehensive assessment of the system under realistic conditions.

Initial tests were performed with a single photovoltaic module under Standard Test

Conditions (STC) to benchmark the system. Subsequently, the complete system, including the 600 V battery and the rooftop module configuration, was analyzed to evaluate the interplay between different converters and MPPT techniques. Key metrics examined include the state of charge (SOC) of the battery, system efficiency, and the time required to initiate and complete the charging process.

These simulations aim to identify the optimal combination of converters and MPPT techniques to ensure maximum efficiency, stability, and effective charging of high-voltage batteries. By tailoring the setup to realistic conditions and the operational needs of the Volvo BZL Electric, this study provides actionable insights into the feasibility and performance of integrating photovoltaic systems into electric bus operations.

5.1 Photovoltaic Module Analysis

The presented graph highlights the electrical behavior of the photovoltaic module under standard test conditions (STC) with constant irradiance and temperature. It shows the voltage (V), current (A), and power (W) output characteristics of the module during the initial simulation phase.

This analysis is crucial as it establishes the baseline performance of the photovoltaic module. The voltage plot confirms the stability of the module's output voltage over time, while the current and power graphs illustrate the module's ability to supply energy efficiently. The power curve, in particular, reflects the module's capacity to deliver consistent power, which is fundamental for ensuring reliable energy input to the subsequent stages of the system, such as the MPPT and DC-DC converter circuits.

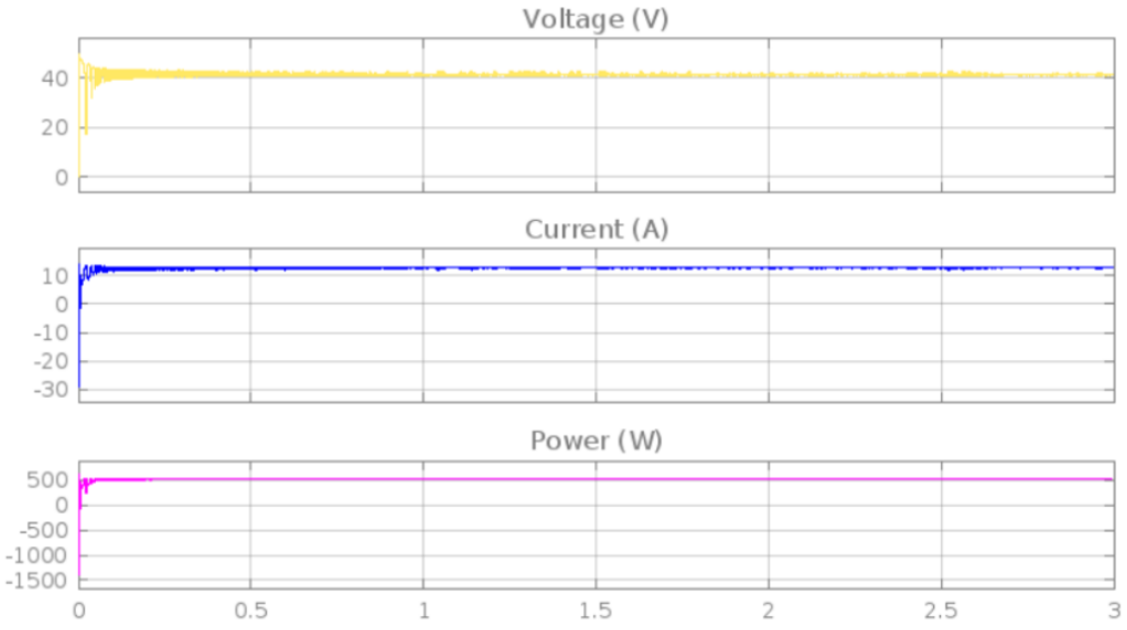

Figure 5.1: Simulation of Photovoltaic module

By interpreting these parameters, we can verify the operational stability of the photovoltaic module and identify the expected input conditions for further system analyses, ensuring compatibility with the converters and MPPT algorithms employed in the study.

5.2 Comparative Analysis of MPPT Techniques with DC-DC Converters

To evaluate the effectiveness of different Maximum Power Point Tracking (MPPT) techniques, simulations were conducted for both the boost and quadratic DC-DC converters. The goal was to compare the power extracted from a photovoltaic (PV) module under Standard Test Conditions (STC), focusing on stability, response time, and efficiency. The MPPT methods analyzed were Incremental Conductance (IC), Perturb and Observe (P&O), Constant Voltage (Vcte), and Fixed Duty Cycle (D).

The diagram illustrates the implementation of a Boost Converter in Simulink, used

to evaluate the performance of different Maximum Power Point Tracking (MPPT) techniques. The boost converter increases the voltage from the photovoltaic (PV) module to match the system requirements, ensuring efficient energy transfer to the load. The design includes essential components such as inductors, capacitors, diodes, and a switching mechanism, which work together to regulate the output voltage according to the MPPT algorithm in use.

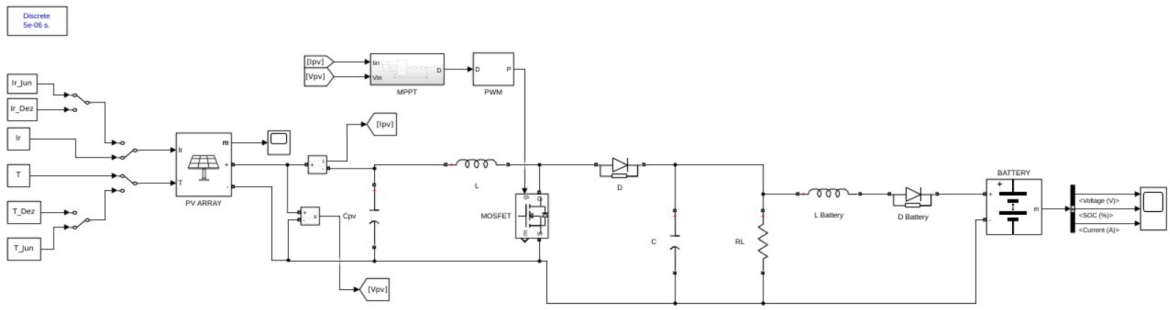

Figure 5.2: Schematic implemented in Simulink for the Boost Converter

The diagram depicts the implementation of a Quadratic Converter in Simulink. This converter topology further steps up the voltage from the PV module. The quadratic converter employs two stages of voltage conversion, involving additional components and control complexity. This configuration is particularly beneficial in scenarios where substantial voltage boosting is required, and its performance was analyzed under the same MPPT techniques for comparison with the boost converter.

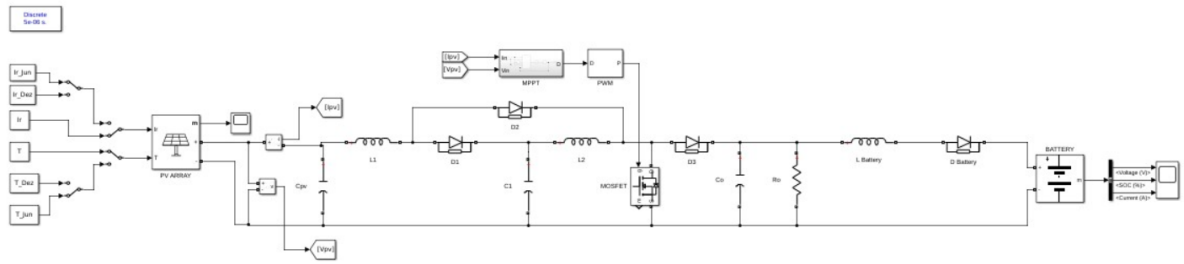

Figure 5.3: Schematic implemented in Simulink for the Quadratic Converter

The output of the simulations was analyzed in terms of the power extracted from the PV module and delivered to the load. This performance is visually represented in the comparison graphs presented in Figures 5.2 and 5.3.

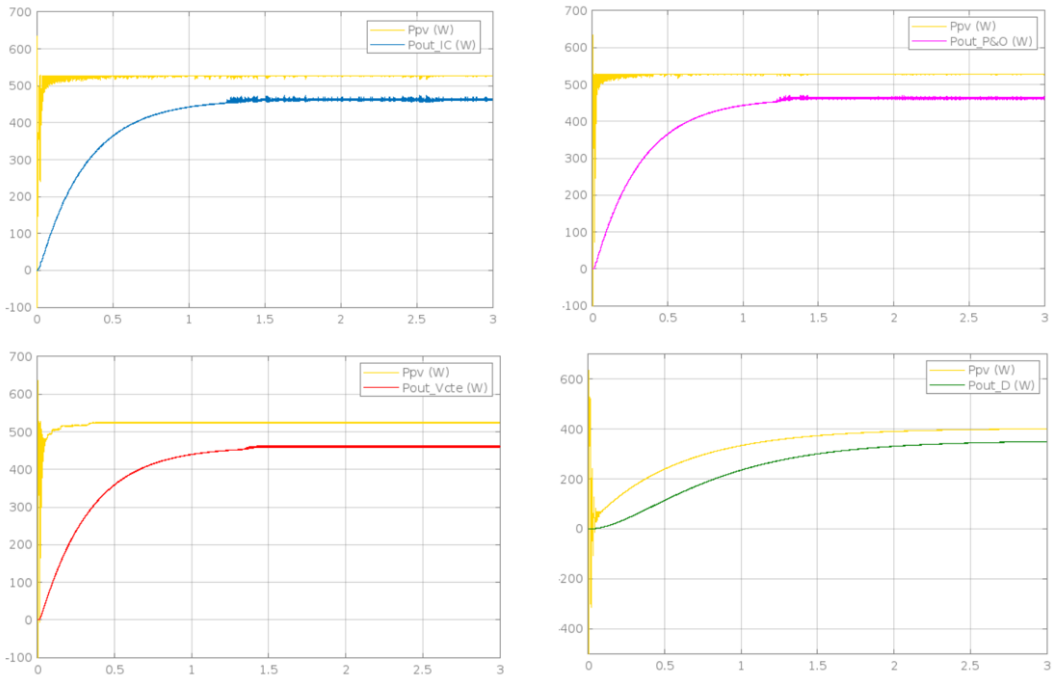

Figure 5.4: MPPT Analysis for boost converter

As depicted in these figures, the graphs highlight the ability of the MPPT techniques to maintain the PV module's operating point near the Maximum Power Point (MPP). Figure

5.4 illustrates the results for the boost converter, while Figure 5.5 shows the corresponding analysis for the quadratic converter.

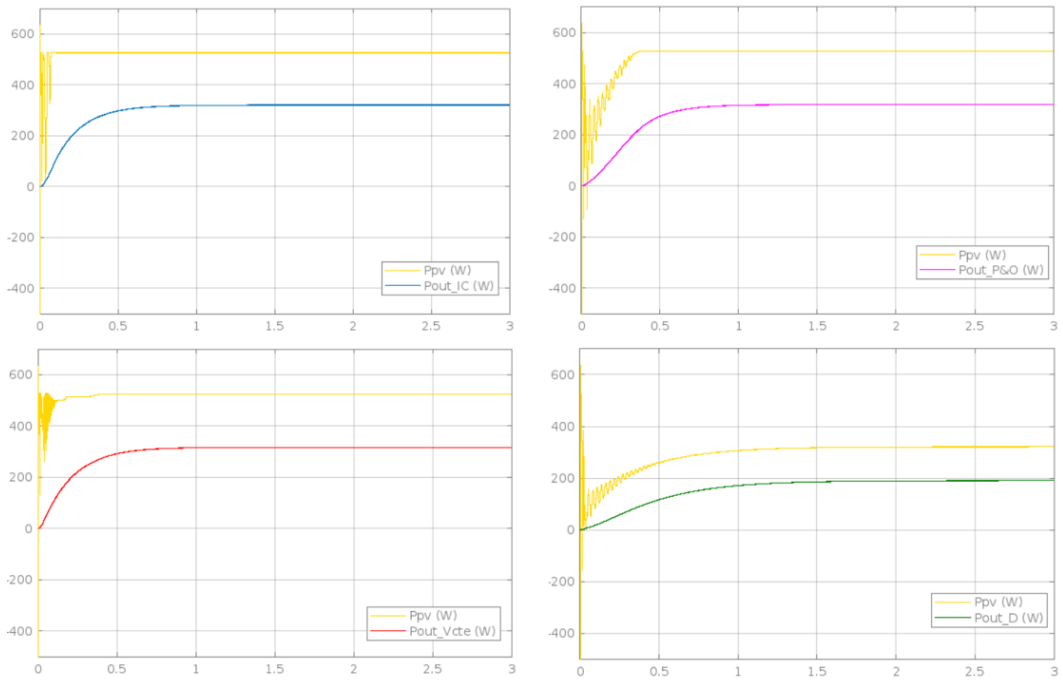

Figure 5.5: MPPT Analysis for quadratic converter

Incremental Conductance (IC)

Boost Converter: Demonstrated high stability with minimal oscillations. The power output quickly settled near the MPP, reflecting the method's precision. Quadratic Converter: Achieved similar results, though slightly more oscillatory. Its ability to reach the target voltage relied on careful load tuning, highlighting its sensitivity to system parameters.

Perturb and Observe (P&O)

Boost Converter: Performed well but exhibited slightly larger oscillations around the MPP compared to IC. The method's iterative nature caused marginal instability. Quadratic Converter: Similar behavior to the boost converter but required a longer stabilization period, especially at higher output voltages.

Constant Voltage (Vcte)

Boost Converter: Achieved satisfactory results with a straightforward implementation. However, the power extraction efficiency was slightly lower than IC and P&O due to a lack of dynamic adjustment. Quadratic Converter: The method struggled to fine-tune to the exact MPP, showing a slight performance gap compared to adaptive techniques.

Fixed Duty Cycle (D)

Boost Converter: While simple to implement, this method showed the lowest efficiency due to its inability to adapt to varying environmental conditions. Quadratic Converter: Similarly, the fixed duty cycle resulted in suboptimal performance, reflecting the limitations of static control strategies.

The IC method emerged as the most robust technique for both converters, offering precise MPP tracking and rapid stabilization. The quadratic converter demonstrated potential for higher output voltages but required careful parameter tuning, particularly with P&O and Vcte methods. Overall, while the boost converter provided more consistent performance, the quadratic converter's ability to achieve higher voltages could be advantageous in specific applications.

5.3 Evaluation of Converter Efficiency for Single and Panel Configurations

The analysis of the tables demonstrates clear trends in the efficiency of both the Boost and Quadratic converters when applied to a single module (41.35V, 530W) and an array of 11 modules in series (454.85V, 5830W), which aligns with the system design constraints of an electric bus.

Table 5.1: Efficiency Results for 1 Module with Boost and Quadratic Converters (With Calculated Resistance)

MPPT Method	**Boost Converter Efficiency**	**Quadratic Converter Efficiency**
Incremental Conductance	0.8735	0.6073
Perturb and Observe	0.8796	0.6040
Constant Voltage	0.8769	0.6038
Duty Cycle	0.8738	0.5924

The Boost converter achieves higher efficiencies (above 87%) compared to the Quadratic converter (around 60%) for the single module scenario. The lower efficiency of the Quadratic converter at this power level is consistent with findings in the literature that suggest it performs less effectively at lower power outputs. This highlights that the Quadratic converter may not be the ideal choice for single-module implementations.

Table 5.2: Efficiency Results for the Panel with Boost and Quadratic Converters (With Calculated Resistance)

MPPT Method	**Boost Converter Efficiency**	**Quadratic Converter Efficiency**
Incremental Conductance	0.9794	0.9647
Perturb and Observe	0.9630	0.9632
Constant Voltage	0.9670	0.9552
Duty Cycle	0.9628	0.9541

For the Boost converter, the efficiency improves to nearly 97%, demonstrating robust performance at higher power levels. The Quadratic converter shows a dramatic improvement in efficiency for the panel configuration, reaching values above 95%. This significant increase underscores the advantage of the Quadratic converter at higher power levels, as supported by the literature, which suggests that its topology and design are better suited for higher power densities and outputs.

The 11-module panel configuration is a direct result of the spatial constraints imposed by the electric bus. With a maximum of 11 modules, the system achieves a nominal

voltage of 454.85V, suitable for efficient energy storage and delivery in electric bus systems. The significant efficiency gains of the Quadratic converter at panel-level power outputs (5830W) validate its application in such scenarios. Despite its lower performance for single modules, the Quadratic converter becomes competitive with the Boost converter at higher power levels, offering a viable alternative depending on specific system requirements.

5.4 State of Charge Dynamics: MPPT Methods and Converter Analysis

The following discussion provide a detailed discussion of the results, supported by graphs that show the SoC behavior for each MPPT strategy, highlighting their specific features and the efficiency of the converters in this application context.

The primary goal of this analysis was to examine the battery's State of Charge (SoC) over time, which is a critical metric for determining how effectively the energy generated by the photovoltaic module is transferred to the battery.

Four MPPT techniques were considered: Incremental Conductance (IC), Perturb and Observe (P&O), Constant Voltage (Vcte), and Duty Cycle (D). These methods were selected for their relevance and widespread usage in renewable energy systems. The aim was to identify variations in performance and analyze how each strategy influences the charging process, particularly in light of the different topological characteristics of the converters.

The simulation results revealed notable differences in the battery's State of Charge (SoC) depending on the MPPT strategy and converter topology employed.

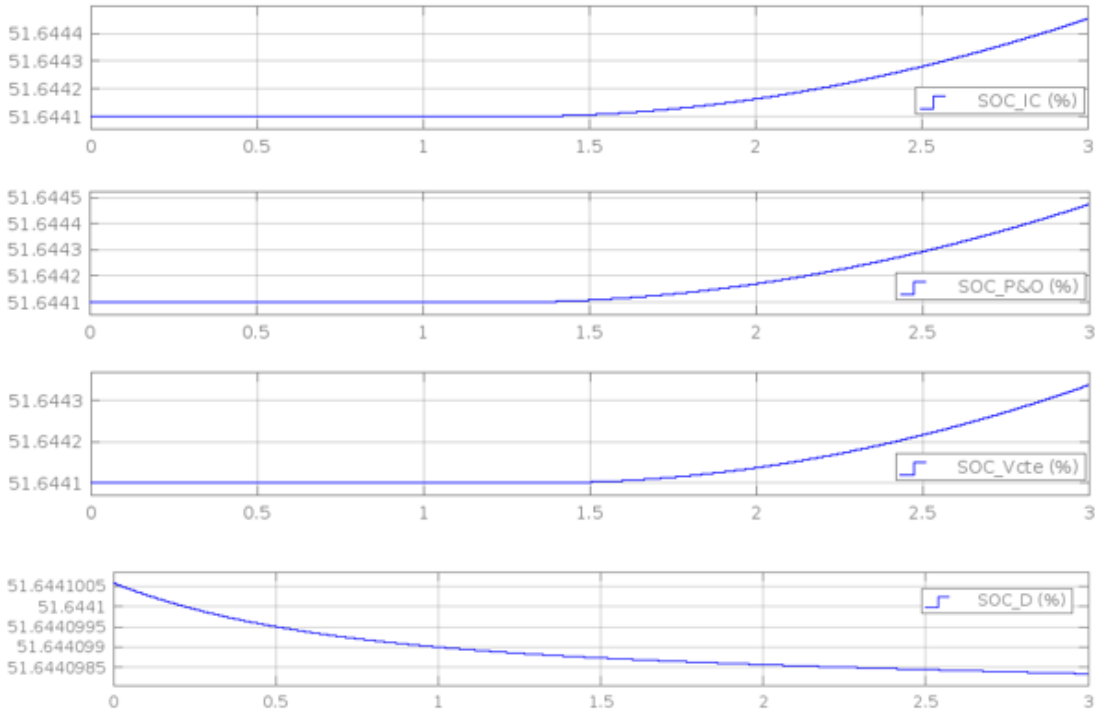

Figure 5.6: SOC for differente MPPTs approach - Boost Converter

For the Boost Converter:

The Incremental Conductance (IC) and Perturb and Observe (P&O) methods exhibited similar trends, with a steady increase in SoC over time. This indicates efficient energy harvesting and proper functioning of the MPPT algorithms. The Constant Voltage (Vcte) method also showed a consistent rise in SoC, although its rate of increase was slightly lower compared to IC and P&O, suggesting a more conservative but stable energy transfer approach. The Duty Cycle (D) method demonstrated almost no significant variation in SoC over time, reflecting poor energy transfer efficiency and inadequate performance in this configuration.

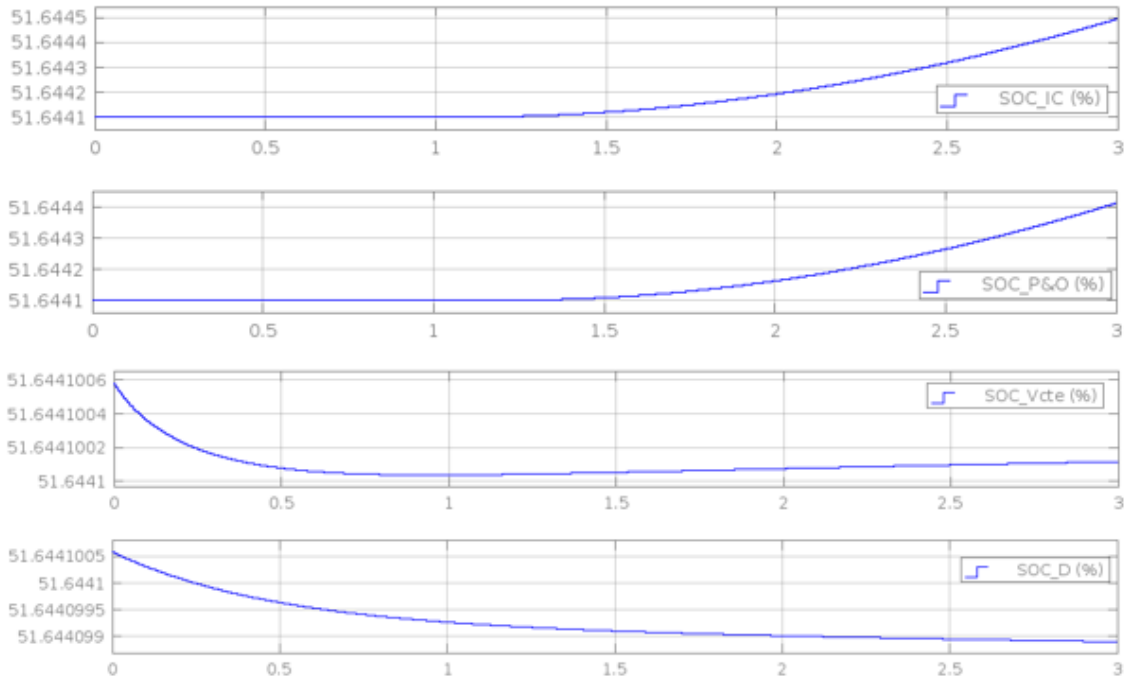

Figure 5.7: SOC for differente MPPTs approach - Quadratic Converter

For the Quadratic Converter:

The Incremental Conductance (IC) and Perturb and Observe (P&O) methods again achieved similar results, with a steady and consistent increase in SoC. This demonstrates that these techniques are effective irrespective of the converter topology. The Constant Voltage (Vcte) method displayed negligible variations in SoC, with performance slightly inferior to that observed in the boost converter. This suggests reduced efficiency in energy transfer with the quadratic topology. The Duty Cycle (D) method showed a slight decrease in SoC over time, indicating substantial inefficiencies in energy harvesting and utilization under this configuration.

These findings underline the significance of selecting the appropriate MPPT strategy based on system requirements and converter topology. The choice of strategy has a direct impact on energy transfer efficiency and the overall performance of the battery.

5.5 System Validation: Photovoltaic Performance Under Seasonal Variations

The choice of the Boost converter combined with the incremental conductance (IC) method for further analysis under variable irradiation and temperature conditions is supported by several key factors derived from the earlier findings and system constraints.

Superior Efficiency Across Power Levels:

The Boost converter demonstrated consistently high efficiency in both single-module (87.35%) and panel (97.94%) configurations. This superior performance aligns well with the requirements of maintaining high energy conversion efficiency, which is crucial for an electric bus application where energy optimization directly impacts operational range and reliability.

Robustness of Incremental Conductance (IC) Method:

Among the MPPT (Maximum Power Point Tracking) techniques analyzed, the incremental conductance method outperformed others, achieving the highest efficiency in all scenarios. The IC method's ability to dynamically and accurately track the maximum power point under variable environmental conditions makes it a reliable choice for real-world applications involving fluctuating irradiation and temperature.

Alignment with System Constraints:

The 11-module panel configuration, determined by the space available on the electric bus, results in a nominal voltage of 454.85V. The Boost converter's capability to step up voltage efficiently makes it a natural fit for this design, ensuring compatibility with the battery charging requirements and the operational constraints of the bus.

Practical Feasibility and Reliability:

The Boost converter's simpler topology and lower component count compared to the Quadratic converter make it a more practical choice for large-scale implementation. Its proven reliability and performance stability under diverse operating conditions add to its appeal for long-term deployment.

The combination of the Boost converter and the incremental conductance method offers a balanced solution, maximizing efficiency while ensuring robustness and adaptability under variable irradiation and temperature conditions. This choice is aligned with the system's design constraints and operational requirements, making it ideal for further exploration and implementation in the electric bus application.

To further analyze the behavior of the photovoltaic system under realistic operating conditions, simulations were conducted considering the variable irradiance and temperature profiles from Curitiba. These profiles represent June, the month with the lowest solar incidence, and December, the month with the highest solar incidence, as shown in Figure.

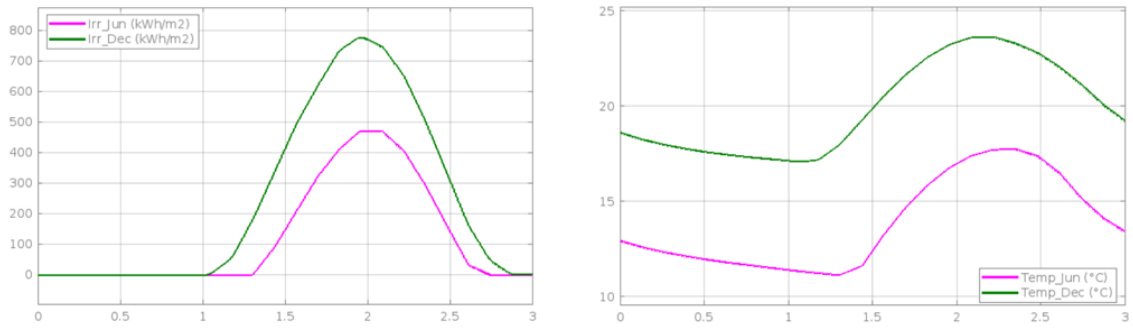

Figure 5.8: Irradiation and Temperature Patterns in Curitiba: Comparison Between the Month of Lowest and Highest Solar Incidence

The chosen combination of the Boost converter and Incremental Conductance (IC) MPPT method was applied to study the system's performance across these contrasting scenarios. This approach provides a detailed understanding of how seasonal variations

influence energy generation, efficiency, and battery charging dynamics, ensuring the robustness of the proposed solution for electric bus applications.

The analysis of Figure below shows the data for the photovoltaic (PV) panel under irradiation and temperature conditions during June in Curitiba. The figure highlights the voltage, current, and power output of the panel over time.

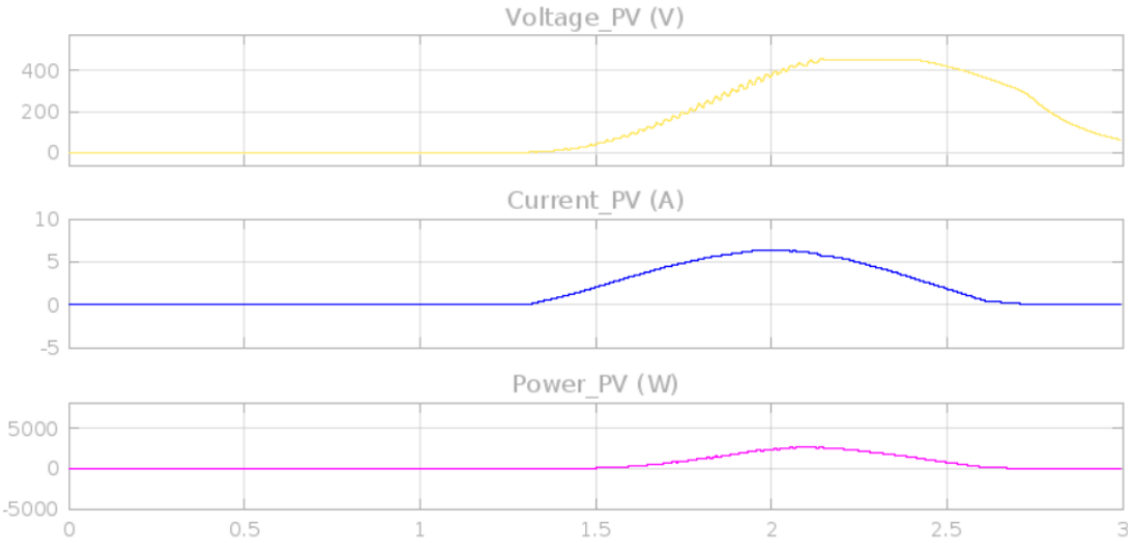

Figure 5.9: Photovoltaic Panel Data for Irradiation and Temperature Conditions During June in Curitiba

This pattern of data is typical for regions with clear skies and moderate temperatures, such as Curitiba in June, when solar irradiance is lower than in summer months but still sufficient to generate power. The trends observed in this figure provide insight into how the photovoltaic panel performs under real-world conditions, reflecting the seasonal variations in solar energy availability. This data is valuable for understanding the energy potential from solar panels and how different factors like temperature and irradiance levels affect their efficiency.

In summary, Figure 5.9 provides a detailed visual of the photovoltaic panel's performance during the month of June in Curitiba, demonstrating the inherent fluctuations in power generation due to environmental factors. This data can serve as a foundation for

further analysis, especially when integrating the panel with other components such as converters and MPPT systems, as shown in subsequent figures.

Figure 5.10 provides a detailed analysis of the Boost Converter Output Data integrated with the photovoltaic panel under irradiation and temperature conditions during June in Curitiba. This figure illustrates how the converter responds to the fluctuations in voltage, current, and power from the solar panel data previously shown in Figure 5.9.

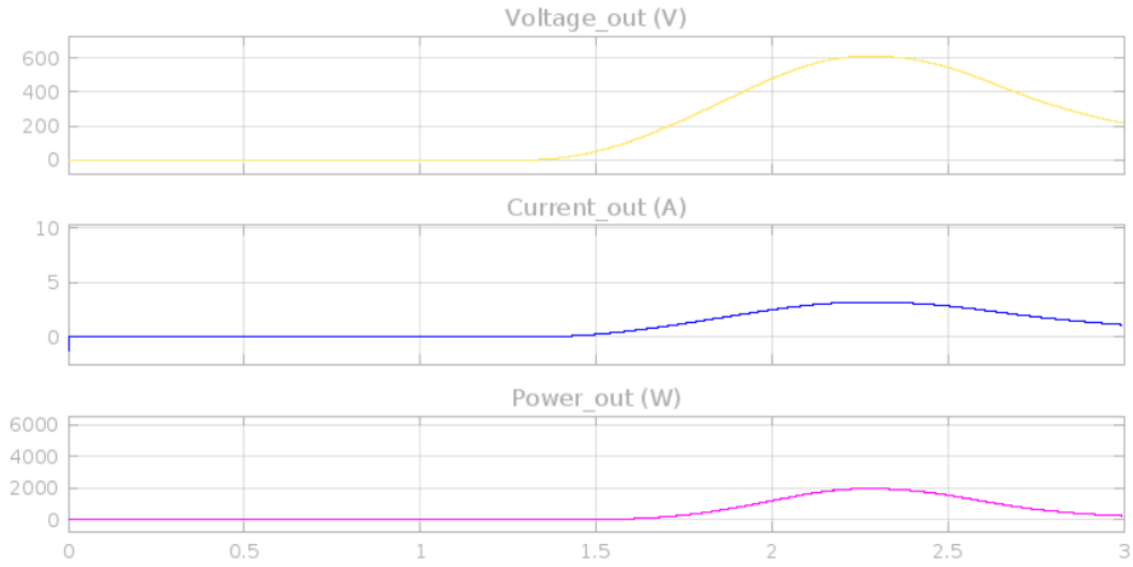

Figure 5.10: Boost Converter Output Data Integrated with the Panel Under Irradiation and Temperature Conditions during June in Curitiba

In essence, Figure 5.10 illustrates the critical role of the boost converter in optimizing energy conversion. By stepping up the voltage and maintaining efficient current flow, the converter ensures that the power output remains more stable and suitable for battery charging, even during periods of variable solar irradiance and temperature. This is particularly important in real-world applications like electric bus charging, where a reliable and efficient power supply is necessary to ensure the vehicle's operational viability.

This figure also highlights how the boost converter helps mitigate power losses that occur due to environmental factors, making it an ideal component in photovoltaic systems that need to operate effectively under varying weather conditions, as is the case in Curitiba

during June. The converter maximizes the usable energy from the solar panel, ensuring the system's reliability and performance.

For the data presented in Figures 5.11 and 5.12, which represent the photovoltaic panel and Boost converter outputs under the irradiance and temperature conditions of December in Curitiba, we observe several key trends.

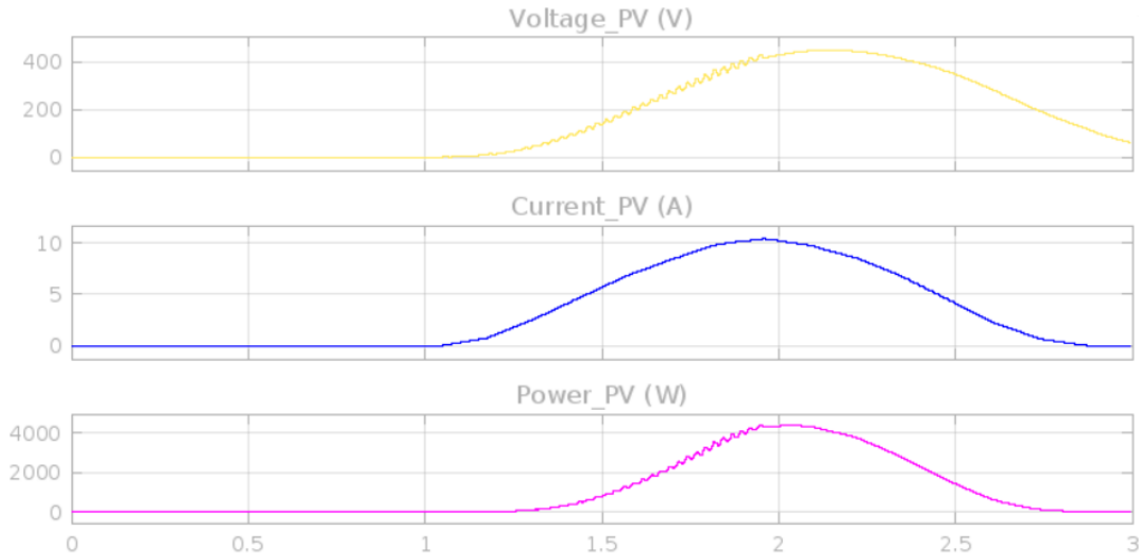

Figure 5.11: Photovoltaic Panel Data for Irradiation and Temperature Conditions During December in Curitiba

During December, the panel shows significantly higher power output compared to June, reflecting the increase in solar irradiance typical of summer months in Curitiba. As seen in the voltage and current graphs, the panel operates at higher voltages and currents, corresponding to the peak power generation in December. The power graph follows this pattern, peaking around midday and gradually decreasing as the sun moves across the sky.

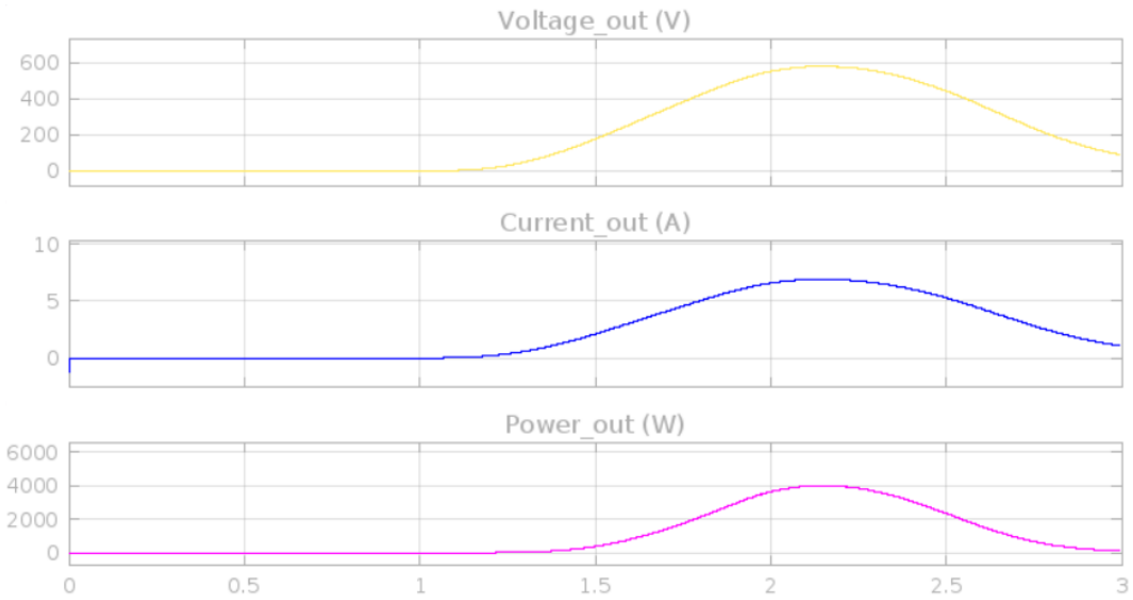

Figure 5.12: Boost Converter Output Data Integrated with the Panel Under Irradiation and Temperature Conditions during December in Curitiba

In line with the panel's increased performance in December, the Boost converter output also shows an improvement in voltage, current, and power compared to June. The higher power generation from the panel is efficiently captured by the Boost converter, which adjusts its output to ensure stable and optimal voltage levels suitable for the electric bus's battery system. The converter operates efficiently with higher power, ensuring the system remains robust under the more favorable environmental conditions of December.

This combination of higher solar irradiance and the Boost converter's effectiveness demonstrates the improved system performance during periods of higher sunlight, with clear implications for the overall energy efficiency of the electric bus in real-world conditions.

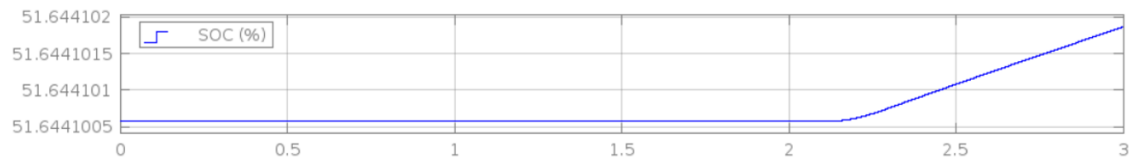

Figure 5.13: State of Charge (SOC) Behavior during June

Figure 5.14: State of Charge (SOC) Behavior during december

In conclusion, this chapter explored the performance of Boost and Quadratic converters in a photovoltaic system designed for integration with an electric bus, analyzing the effectiveness of different Maximum Power Point Tracking (MPPT) methods under varying environmental conditions. The combination of the Boost converter and the Incremental Conductance (IC) MPPT method demonstrated superior efficiency in both single-module and array configurations. This solution offered a balanced approach, ensuring robust performance while optimizing power extraction across fluctuating solar irradiance and temperature profiles.

Ultimately, the combination of the Boost converter with the IC MPPT method presents a promising approach for photovoltaic systems in electric vehicles, contributing to the growing body of knowledge on sustainable energy solutions for transportation. Future research could explore additional environmental scenarios and alternative converter technologies to further optimize the system's performance and adaptability across a wider range of conditions.

Chapter 6

Conclusion and Future Work

This work presented a comprehensive analysis of the performance of different Maximum Power Point Tracking (MPPT) techniques applied to Boost and Quadratic converters in a photovoltaic system designed for integration into electric buses. Through detailed simulations, the study evaluated energy efficiency, stability, and response under real operating conditions, including variations in solar irradiance and temperature.

The findings of this research demonstrated that the combination of the Boost converter with the Incremental Conductance (IC) method is the most suitable configuration for the proposed system. This setup exhibited superior performance in terms of efficiency, achieving 87.35% for a single module and 97.94% for an 11-module array. These results validate its application in larger-scale systems, making it an optimal choice for scenarios requiring robust energy conversion and stability.

The system was further tested under the climatic conditions of Curitiba, focusing on two distinct scenarios: June, representing the month with the lowest solar incidence, and December, characterized by the highest solar incidence. These tests confirmed the robustness of the Boost converter and the IC method, even under low irradiance conditions. The configuration consistently delivered efficient energy transfer to the battery, maintaining a desirable State of Charge (SoC) behavior across the analyzed periods.

The comparison of MPPT techniques highlighted the Incremental Conductance method as the most effective due to its adaptability and precision, particularly in environments

with fluctuating solar conditions. Other methods, such as Perturb and Observe (P&O) and Constant Voltage (Vcte), displayed slightly lower efficiency, while the fixed Duty Cycle approach proved inadequate for dynamic applications.

The proposed solution aligns with the design constraints of an electric bus, meeting spatial limitations, voltage requirements, and energy demands. Its implementation offers a viable and sustainable alternative, contributing to the advancement of renewable energy integration in transportation.

While the results of this study are promising, some limitations were identified that provide opportunities for future research. The integration of the proposed system with advanced battery technologies, such as solid-state or lithium-sulfur batteries, could be explored to assess their influence on overall performance. Additionally, scaling the system to larger configurations with more photovoltaic modules or buses of varying dimensions would provide further insights into its scalability.

Future studies could also focus on experimental validation of the system under real-world conditions, enabling a direct comparison between simulated results and field data. Extending the analysis to include global climate models would allow for the evaluation of system performance in regions with more extreme irradiance and temperature patterns. Moreover, the exploration of innovative MPPT algorithms, particularly those leveraging artificial intelligence techniques such as neural networks or machine learning, could further enhance the system's efficiency and adaptability.

In conclusion, the results of this research underscore the feasibility and efficiency of using Boost converters in conjunction with the Incremental Conductance MPPT method for photovoltaic systems in electric buses. The proposed solution not only optimizes energy conversion but also demonstrates a high degree of adaptability to variable climatic conditions, fulfilling the requirements of a sector increasingly reliant on sustainable and innovative solutions. By combining technical rigor with practical relevance, this study contributes to the advancement of renewable energy technologies in transportation, offering a promising pathway toward reducing dependence on fossil fuels and fostering a more sustainable future.

Bibliography

[1] J. Pinho and M. Galdino, *Manual de Engenharia para Sistemas Fotovoltaicos*. CEPEL-CRESESB, 2014.

[2] N. R. d. S. Sá, "Sistema de conversão de energia solar fotovoltaica para carregamento de um veículo elétrico," Ph.D. dissertation, Instituto Superior de Engenharia de Lisboa, 2017.

[3] National Renewable Energy Laboratory, *Best research-cell efficiency chart*, `https://www.nrel.gov/pv/cell-efficiency.html`, Accessed in 2023.

[4] International Energy Agency, "Trends in photovoltaic applications 2022," Report, 2022.

[5] E. B. Pereira *et al.*, "Atlas brasileiro de energia solar," *São josé dos campos: Inpe*, vol. 1, 2017.

[6] C. S. Solanki, *Solar photovoltaics: fundamentals, technologies and applications*. Phi learning pvt. Ltd., 2015.

[7] Empresa de Pesquisa Energética, "Plano decenal de expansão de energia 2029," Report, 2029.

[8] A. Jäger-Waldau, "Pv status report 2018," European Commission, Tech. Rep., 2018.

[9] M. Z. Jacobson *et al.*, "100% clean and renewable wind, water, and sunlight all-sector energy roadmaps for 139 countries of the world," *Joule*, vol. 1, no. 1, pp. 108–121, 2017.

[10] Renewable Energy Policy Network for the 21st Century, "Renewables 2023 global status report," Report, 2023.

[11] Universidade Tecnológica Federal do Paraná (UTFPR), *Atlas de energia solar do estado do paraná*, 2022.

[12] G. Tiepolo, O. Canciglieri, J. Urbanetz, T. Viana, and E. B. Pereira, "Comparação entre o potencial de geração fotovoltaica no estado do paraná com alemanha, itália e espanha," in *V Congresso Brasileiro de Energia Solar – V CBENS*, Recife, 2014.

[13] L. M. Fraas, *Low-Cost Solar Electric Power*. Springer, 2014.

[14] I. E. Agency, *Renewables 2021: Analysis and Forecast to 2026*. IEA Publications, 2021.

[15] M. Kumar and A. Kumar, "Performance assessment and degradation analysis of solar photovoltaic technologies: A review," *Renewable and Sustainable Energy Reviews*, vol. 78, pp. 554–587, 2017.

[16] M. A. Green, *Solar Cells: Operating Principles, Technology, and System Applications*. Prentice-Hall, 1982.

[17] J. A. Mathews, *Renewable Energy and the Path to Sustainable Development*. Palgrave Macmillan, 2015.

[18] R. C. Perez, "Comparação entre diferentes tecnologias de módulos fotovoltaicos," B.S. thesis, 2022.

[19] S. Hutyria, V. Yahlinskyi, A. Chanchin, Y. Khomiak, and V. Popov, "Evolution of trolleybus: Directions, indicators, trends," *Diagnostyka*, vol. 21, no. 1, pp. 11–26, 2020. DOI: 10.29354/diag/116080.

[20] Y. Boquet, "The renaissance of tramways and urban redevelopment in france," *Miscellanea Geographica*, vol. 21, no. 1, pp. 5–18, 2017.

[21] T. Boonraksa, P. Boonraksa, G. Sakulphaisan, and B. Marungsri, "Strategic planning of charging stations for electric public transportation bus systems: A case study," *Int Rev Electr Eng (IREE)*, vol. 15, no. 6, pp. 512–522, 2020.

[22] G. A. d. O. Rugeri, "Análise de custos e de emissões na substituição de ônibus à combustão interna por elétricos no transporte público de porto alegre," 2022.

[23] D. Göhlich, T.-A. Fay, D. Jefferies, E. Lauth, A. Kunith, and X. Zhang, "Design of urban electric bus systems," *Design Science*, vol. 4, e15, 2018.

[24] P. R. GUENTHER and T. D. PADILHA, "Estudo de viabilidade para substituição de veículos a combustão por veículos de tração elétrica em uma linha de ônibus de curitiba," *TCC (Engenharia elétrica). Universidade Federal do Paraná, Curitiba*, 2016.

[25] C. A. L. dos Santos, "Baterias de íons li para veículos elétricos," *Revista IPT: Tecnologia e Inovação*, vol. 2, no. 9, 2018.

[26] B. Wu, Y. Ren, and N. Li, "Lifepo4 cathode material," *Electric Vehicles-The Benefits and Barriers*, vol. 3, pp. 199–216, 2011.

[27] S. De Breucker, "Impact of dc-dc converters on li-ion batteries," *KU Leuven: Leuven, Belgium*, 2012.

[28] B. Scrosati and J. Garche, "Lithium batteries: Status, prospects and future," *Journal of power sources*, vol. 195, no. 9, pp. 2419–2430, 2010.

[29] J. da Luz Ferro and I. Barbi, "Carregador de baterias de íon-lítio para veículos elétricos integrado a geração fotovoltaica," in *Anais Congresso Brasileiro de Energia Solar-CBENS*, 2018.

[30] C. Mikolajczak, M. Kahn, K. White, and R. T. Long, *Lithium-ion batteries hazard and use assessment*. Springer Science & Business Media, 2012.

[31] T. Geist, H. Kamath, S. F. Porter, and P. May-Ostendorp, "Designing battery charger systems for improved energy efficiency," *Technical Primer, EPRI SOLUTIONS*, 2006.

[32] J. M. A. Aniceto, "Conversor dc-dc com busca de ponto de potência máxima (mppt) para painéis solares," M.S. thesis, Universidade NOVA de Lisboa (Portugal), 2010.

[33] D. F. C. Moniz, "Conversor dc-dc bidirecional isolado ressonante aplicado a veículos elétricos," M.S. thesis, 2015.

[34] Y. V. Sampaio, "Análise comparativa do desempenho de conversores dc-dc aplicados ao carregamento de veículos elétricos," M.S. thesis, Universidade da Beira Interior (Portugal), 2021.

[35] R. Crews, "An-1820 lm5032 interleaved boost converter," *Texas Instruments Inc., Dallas, TX, App. Rep. SNVA335A*, 2013.

[36] A. Thiyagarajan, S. P. Kumar, and A. Nandini, "Analysis and comparison of conventional and interleaved dc/dc boost converter," in *Second international conference on current trends in engineering and technology-ICCTET 2014*, IEEE, 2014, pp. 198–205.

[37] N. Mohan, T. M. Undeland, and W. P. Robbins, *Power electronics: converters, applications, and design*. John wiley & sons, 2003.

[38] P. R. M. Costa, L. T. Medeiros, I. R. MACHADO, and M. R. De Castro, "Técnica de seguimento do ponto de potência máxima global baseado em estimativa para arranjos fv submetidos à sombreamento parcial," in *Anais Congresso Brasileiro de Energia Solar-CBENS*, 2020.

[39] N. Karami, N. Moubayed, and R. Outbib, "General review and classification of different mppt techniques," *Renewable and Sustainable Energy Reviews*, vol. 68, pp. 1–18, 2017.

[40] N. Onat, "Recent developments in maximum power point tracking technologies for photovoltaic systems," *International Journal of Photoenergy*, vol. 2010, no. 1, p. 245 316, 2010.

[41] S.-I. Go, S.-J. Ahn, J.-H. Choi, W.-W. Jung, S.-Y. Yun, and I.-K. Song, "Simulation and analysis of existing mppt control methods in a pv generation system," *Journal of International Council on Electrical Engineering*, vol. 1, no. 4, pp. 446–451, 2011.

[42] M. A. G. De Brito, L. Galotto, L. P. Sampaio, G. d. A. e Melo, and C. A. Canesin, "Evaluation of the main mppt techniques for photovoltaic applications," *IEEE transactions on industrial electronics*, vol. 60, no. 3, pp. 1156–1167, 2012.

[43] R. Faranda, S. Leva, *et al.*, "Energy comparison of mppt techniques for pv systems," *WSEAS transactions on power systems*, vol. 3, no. 6, pp. 446–455, 2008.

[44] K. Hussein, I. Muta, T. Hoshino, and M. Osakada, "Maximum photovoltaic power tracking: An algorithm for rapidly changing atmospheric conditions," *IEE Proceedings-Generation, Transmission and Distribution*, vol. 142, no. 1, pp. 59–64, 1995.

[45] M. A. G. d. Brito, "Inversores integrados monofásicos e trifásicos para aplicações fotovoltaicas: Técnicas para obtenção de mppt, detecção e proteção de ilhamento, sincronização e paralelismo com a rede de distribuição de energia elétrica," 2013.

[46] L. F. Sauthier, A. T. Diefenthäler, P. S. Sausen, A. T. Z. R. Sausen, M. d. Campos, and G. Walker, "Modelagem matemática de módulos fotovoltaicos empregados em ambientes de simulação de geração distribuída," in *11th Seminar on Power Electronics and Control (SEPOC 2018)*, Brasil, 2023.

[47] L. Wuidart, "Topologies for switched mode power supplies," *Application Note AN*, vol. 513, p. 0393, 1999.

[48] N. Brás, "Conversor Elevador Quadrático e Geradores Termoelétricos para Recolha de Energia Térmica," Dissertação para obtenção de Grau Mestre em Engenharia Eletrotécnica e de Computadores, Master's Thesis, Instituto Superior Técnico, Lisbon, Portugal, Oct. 2014.

[49] D. J. M. Fernandes, "Carregamento de um veículo elétrico através de energia solar fotovoltaica.," Ph.D. dissertation, 2023.

[50] C. G. da Silva Moraes, "Projeto e implementação de um microinversor grid-tied com boost quadrático para,"

[51] P. Pereira, A. Souza, and I. Santos, "Modelagem e avaliação de desempenho das principais técnicas de controle de mppt empregadas na geração fotovoltaica," *Universidade Federal de Uberlandia-UFU*, 2016.

[52] D. Lemos, "Algoritmo mppt para conversor cc-cc para aplicação em painéis fotovoltaicos," M.S. thesis, Instituto Superior Técnico (IST), Lisbon, Portugal, Nov. 2015.

[53] F. J. d. S. Lopes, "Utilização de baterias de iões de lítio em sistemas de armazenamento de energia," Ph.D. dissertation, Instituto Superior de Engenharia de Lisboa, 2016.

[54] O. Tremblay, "Experimental validation of a battery dynamic model for ev application," *World Electric Vehicle Journal*, vol. 3, pp. 1–10, 2009.

[55] E. B. GmbH, *He 341440 nca lithium ion cell - high energy (10 ah)*, Online datasheet, Accessed: 2024-11-13, 2021. [Online]. Available: `https://eas-batteries.com/system/files/attachments/Data%20sheet%20HE%20341440%20NCA%2010%20Ah_1.pdf`.

Appendix A

Solar Irradiation and Productivity Data

Table A.1: Values of average annual irradiation and estimated productivity on an inclined plane at latitude, with a performance rate of 75%, found in Paraná and European countries [11]

Paraná / European Country	Irradiation (kWh/m².year)	Productivity (kWh/kWp.year)	Percentage Difference (%)
Paraná	1,789	1,342	—
Cyprus	2,217	1,663	-19.31
Malta	2,155	1,617	-17.00
Portugal	1,996	1,497	-10.38
Spain	1,948	1,461	-8.14
Greece	1,897	1,423	-5.68
Turkey	1,873	1,405	-4.47
Italy	1,750	1,313	2.22
Macedonia	1,696	1,272	5.47
Bulgaria	1,631	1,223	9.71
Croatia	1,570	1,178	13.93
Montenegro	1,563	1,172	14.54
Serbia	1,531	1,148	16.83
France	1,513	1,135	18.25
Romania	1,496	1,122	19.60
Hungary	1,490	1,117	20.10
Slovenia	1,444	1,083	23.90
Slovakia	1,333	1,000	34.17
Austria	1,325	994	35.00
Czech Republic	1,256	944	42.44
Poland	1,252	939	42.85
Germany	1,251	938	43.00
Luxembourg	1,243	932	43.94
Netherlands	1,242	931	44.06
Belgium	1,238	928	44.54
Denmark	1,211	908	47.73
Lithuania	1,183	887	50.52
Latvia	1,175	881	51.22
Ireland	1,174	880	51.34
United Kingdom	1,153	865	55.11
Estonia	1,151	864	55.36
Sweden	1,084	813	61.43
Finland	1,054	790	69.81
Iceland	949	712	88.43

Source: Adapted from [11]

Appendix B

Other Appendices

Appendix 1 - Matlab Code

```
Tr = 25 + 273.15;          % Reference temperature in Kelvin
tamb = 25;                 % Ambient temperature in °C
NOCT = 25;                 % Nominal operating cell temperature
Gr = 1000;                 % Reference irradiance in W/m²
G = 1000;
T = 273.15 + tamb;

Ir_Jun=xlsread("Ir_Jun.xlsx");
T_Jun=xlsread("T_Jun.xlsx");
Ir_Dez=xlsread("Ir_Dez.xlsx");
T_Dez=xlsread("T_Dez.xlsx");


%%%%%%%%%%%%%%%%%%%%%%%%%%%%%%%%%%%%%%%%%%%%%%%%%%%%%%%%%%%%%%%%%%%%%%%%%%%%

% Characteristics of the HG-L530-72CW photovoltaic module
 Vmpr = 41.35;              % Maximum power voltage in V
 Vcar = 49.90;              % Open circuit voltage in V
 Impr = 12.83;              % Maximum power current in A
 Iccr = 13.76;              % Short circuit current in A
 Ns = 144;                  % Number of cells
 Ki = 0.03;                 % Temperature coefficient for current (A/°C)
 Kv = -0.38;                % Temperature coefficient for voltage (V/°C)

 % Panel model constants
 q = 1.602 * 10^(-19);      % Electron charge in C
 K = 1.38 * 10^(-23);       % Boltzmann constant in J/K
 E = 1.12 * q;              % Energy gap of the cell (approx. for Si)

 % Mathematical model of the panel
 Vtr = K * Tr / q;                              % Reference thermal voltage
 m = (Vmpr - Vcar) / (Vtr * log(1 - (Impr / Iccr)));  % Ideality factor

 %data for plotting the characteristic curve
 Vt = K * T / q;
 Ior = Iccr / (exp(Vcar / (m * Vtr)) - 1);
 Io = Ior * (T / Tr)^3 * exp((Ns * E / m) * (1 / Vtr - 1 / Vt));
 Ipv = (Iccr + Ki * (T - Tr)) * (G / Gr);

 I=0:0.1:13.76;
 V=m*Vt*log(1+((Ipv-I)/Io));
 P=V.*I;

 %Resistance sizing
 Rcarga=Vmpr/Impr;
 Rs=0.98;
 Rp=(Rs*Impr+Vmpr)/(Iccr-Impr);
```

```
%BOOST converter sizing (MPPT/Input voltage Uin=41.35 => Uo=700)
F=10*10^3;
T=1/F;
Uo=700; %Converter output voltage
delta_i=0.10;
delta_vout=0.10;


D=1-(Vmpr/Uo);
A=10;
Uc=D*A;
Iout=Impr*(1-D);
RL=Vmpr/(Impr*(1-D)^2);
L=Vmpr*D*T/delta_i;
C=D*T*Iout/delta_vout;

%%%%%%%%%%%%%%%%%%%%%%%%%%%%%%%%%%%%%%%%%%%%%%%%%%%%%%%%%%%%%%%%%%%%%%%%%%%%%%%

D3=1-sqrt(Vmpr/Uo);
Io3=Impr*(1-D3)^2;
Ro3=Vmpr/(Io3*(1-D3)^2);
L13=(Vmpr*D3)/(delta_i*F);
L23=(Vmpr*D3)/((1-D3)*delta_i*F);
Co3=(Vmpr*D3)/(Ro3*F*delta_vo*(1-D3)^2);
C13=(Vmpr*D3)/(Ro3*F*delta_vo*(1-D3));
```

Appendix 2 - Catalog of photovoltaic panels under study

HG-L Lightweight & Flexible Series

Greatly decreased the product weight, far less cost to install.

500W–530W

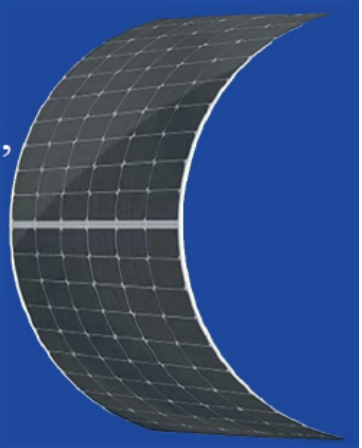

- **Products Features**
  - Lightweight, Ultra-high flexibility, Easy to install.
  - Reducing the adaptive loss to get higher power.
  - Competitive weak light tolerance performance.
  - Minimizing the shading affection to reduce power loss.
  - The superior reliability has been proven through rigorous weathering test:
    - Sand and dust resistance, acid and alkali-resistance, salt mist resistance
    - Anti- PID
    - Hail shock resistence

- **Quality System**

  IS09001
  IS014001
  IS045001

- **Product Warranty**

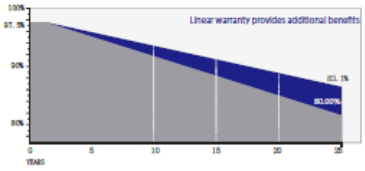

12 YEARS Quality and process performance Assurance

Address: No.633 ChengnanAvenue, Banqiao Industrial Park, RongchangDistrict, Chongqing, China

Wepsite: www.hg-energy-group.cn

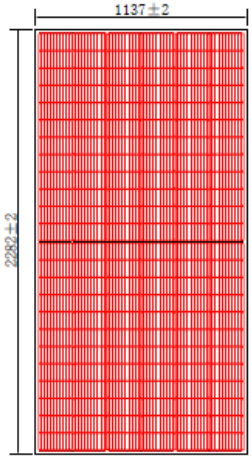

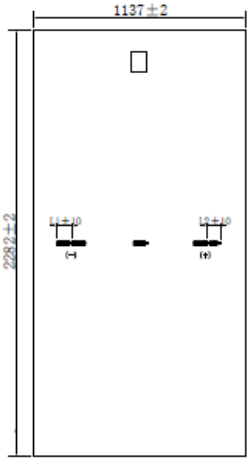

Electrical Parameters

Module Type	HG-L500-72CW		HG-L505-72CW		HG-L520-72CW		HG-L525-72CW		HG-L530-72CW	
	STC	NMOT	STC	NMOT	STC	NMOT	STC	NMOT	STC	NMOT
Maximum Power (P_{max})	500W	372W	505W	376W	520W	387W	525W	391W	530W	394W
Open Circuit Voltage (V_{oc})	49.00V	45.78V	49.15V	45.92V	49.60V	46.35V	49.75V	46.49V	49.90V	46.63V
Short Circuit Current (I_{sc})	13.35A	10.77A	13.42A	10.83A	13.63A	11.00A	13.70A	11.06A	13.76A	11.11A
Max Power Voltage (V_{mp})	40.45V	38.34V	40.60V	38.48V	41.05V	38.91V	41.20V	39.05V	41.35V	39.19V
Max Power Current (I_{mp})	12.37A	9.70A	12.45A	9.77A	12.68A	9.95A	12.75A	10.01A	12.83A	10.05A
Module Efficiency STC (η_m)	19.3%		19.5%		20.0%		20.2%		20.4%	
Power Tolerance	0~+5W									
Maximum System Voltage	1500V DC									
Max Serise Fuse Rating	25A									

STC:irradiance 1000W/m² module temperature 25℃ AM=1.5
NMOT: irradiance of 800W / m², ambient temperature 20℃, and wind speed 1m / s
The uncertainty of Pmax, Voc, Isc testing is ± 3%

Mechanical Specifications

Extermal Dimension	2282mm*1137mm	
Version	Enhanced Version	High Performance Version
Thickness	3.4±0.2mm	3.6±0.2mm
Weight	10.5±0.5kg	11.5±0.5kg
Solar Cell	Mono crystalline182*91mm, 144 (6*24)	
Frame	/	
GLASS	/	
Junction Box	IP68,3diodes, MC4 compatible	
Output Cables	4.0mm²(IEC),250~300mm(+)/250~300mm(-)or Customized Length	

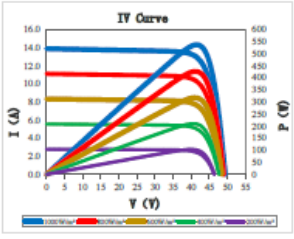

Temperature characteristic

Pmax Temperature Coefficient	-0.35 %/° C
Voc Temperature Coefficient	-0.26 %/° C
Isc Temperature Coefficient	+0.047 %/° C
Operating Temperature	-40 ~+85 ° C
Nominal module operation temperature	45 ± 2 ° C

Package

Packing Unit	40HQ	17.5m platform truck
PCS/CTNS	68	68
Qty of Package	18	28
PCS/Packages	1224	1904

Appendix 3 – Battery Catalog Under Study

HE341440 NCA

Lithium Ion Cell - High Energy

3.6 V / 10 Ah / 36 Wh

Physical and Mechanical Characteristics

Diameter	34 mm
Length	174 mm (144 mm without terminals)
Weight	0.32 kg
Volume	0.13 l
Material	Stainless steel housing Positive terminal: Al M8 length: 10 mm Negative terminal: Cu M8 length: 10 mm

Chemical Characteristics

Cathode	Lithium Nickel Cobalt Aluminium Oxide (NCA)
Anode	Graphite

Electrical Characteristics

Reference Temperature 23°C +/- 3°C

Nominal operating voltage	3.6 V
Nominal capacity at 0.2 C	10 Ah
AC Impedance (1 kHz)	≤ 2 mOhm
DC Resistance (ESR) 2s pulse discharge @ 20°C / 50% SOC	≤ 6.5 mOhm
Specific energy at 0.2 C	113 Wh/kg
Energy density at 0.2 C	275 Wh/l
Specific power 2s pulse discharge @ 50% SOC, 60C	2,000 W/kg
Power density 2s pulse discharge @ 50% SOC, 60C	4,910 W/l

Operating Conditions

Reference Temperature 23°C +/- 3°C

Recommended charge method	Constant current / Constant voltage
End of charge	I ≤ C/100
Maximum charge voltage	4.2 V
Recommended charge current	Up to 5 A (0.5 C)
Maximum continuous charge current	Up to 20 A (2 C)
Maximum pulse charge current (15 s) (Max SOC 70%, average current <88 A)	50 A (5 C)
Recommended voltage limit for discharge	3.0 V
Lower voltage limit for discharge	2.7 V (at high current or low temperature)
Lower voltage limit for pulse discharge	2.0 V
Recommended discharge current	Up to 10 A (1 C)
Maximum continuous discharge current	Up to 50 A (5 C)
Maximum pulse discharge current (2 s)	Up to 300 A (30 C)
Operating temperature	-30 °C to +60 °C
Recommended charge temperature	0 °C to +40 °C
Storage and transport temperature	-40 °C to +60 °C
Recommended storage	+10 °C to +25 °C, 30-50 % SOC
Cycle life at 20°C and 100% DoD, 0.5 C	> 1,000 cycles to 80 % of nominal capacity
Cycle life at 20°C and 80% DoD, 0.5 C	> 2,000 cycles to 80 % of nominal capacity

Voltage vs discharge capacity
for various discharge currents

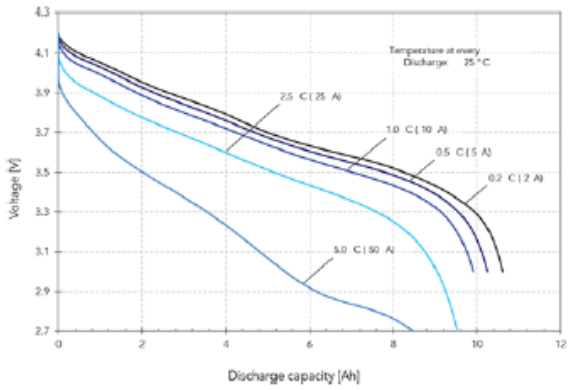

Voltage vs discharge capacity
for various temperatures

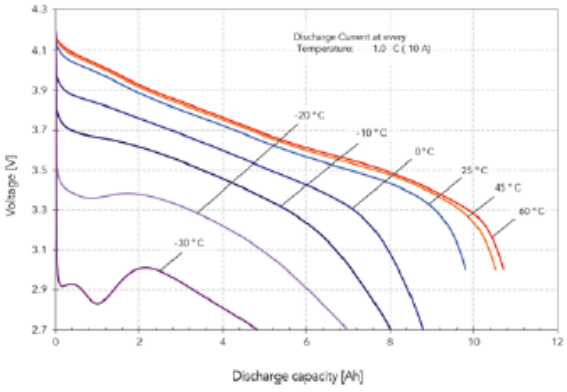

Appendix 4 – Volvo BZL Electric Catalog

Volvo Buses. Driving quality of life

VOLVO BZL ELECTRIC

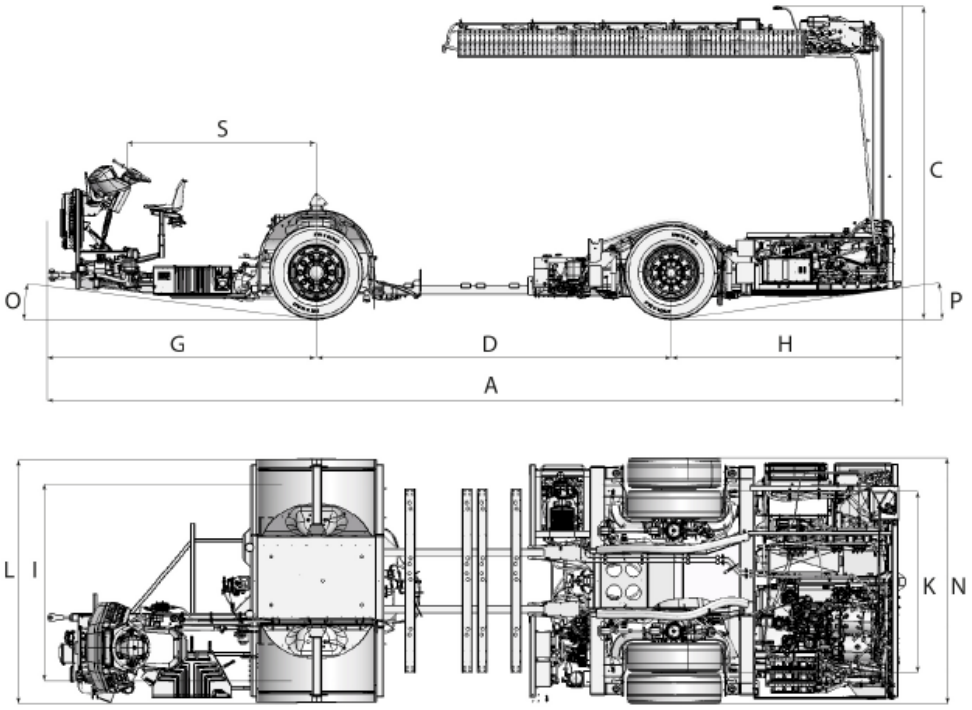

Model		BZL Electric
Overall dimensions		
A	Overall chassis length, depending on body, up to (mm)	11815
C	Frame height at rear structure (mm)	935
D	Transport wheelbase	3700
G	Front overhang (mm)	2500
H	Rear overhang (mm)	2315
S	Steering wheel position (mm)	1980
I	Track, front (mm)*	2107
K	Track, rear (mm)*	1885
L	Overall width front wheels or housing (mm)*	2500
N	Overall width rear wheels (mm)*	2500
O	Approach angle (°)	7
P	Departure angle (°)	7
	*) Overall height, approach and departure angles with tyres:	275/70 R22.5

VOLVO BZL ELECTRIC

Model	BZL Electric
Weights	
Permitted front axle load (kg)	7500
Permitted drive axle load (kg)	12000
Permitted GVW (kg)	19500
Electrical motor	
EPT 402 (1 motor)	
Output, max (kW)	R85 max 200
Continuous power (kW)	R85 30 min 167
Max torque (Nm)	425
Max wheel torque (Nm)	19000
EPT802 (2 motors)	
Output, max (kW)	R85 max 400
Continuous power (kW)	R85 30 min 334
Max torque (Nm)	850
Max wheel torque (Nm)	31000
Transmission and axles	
Gearbox	Volvo 2-speed Automated Manual Transmission
Front axle	Volvo RFS-L
Rear axle	ZF AV133
Differential lock	No
Suspension and steering	
Air bellows, front	2
Air bellows, rear	4
Kneeling	Optional
Max wheel angle	53
Power steering	Electric driven hydraulic steering
Steering wheel side	LHD/RHD

VOLVO BZL ELECTRIC

Energy storage system
- Lithium-ion battery
- Chassis including ESS module to be roof mounted
- Automatic temperature controlling of batteries

ESS (Energy Storage System)

Available storage energy (battery capacity)
94 kWh

Available storage energy (3–5 batteries)
282, 376, 470 kWh

Battery chemistry type
Lithium-ion, NCA

Energy density (Wh/kg)
159 Wh/kg (incl. brackets)

C Rating (maximum charge/discharge rate)
0.9

Voltage
600 V

Mass (kg)
590 kg incl. brackets

Charging system
CCS2 DC
- Industry standard solution
- Maximum charge power 150 kW
- Rear right or rear left charging

OppCharge
- Industry standard solution
- Maximum charge power 300 kW
- Customer decision of position of rails

Volvo Ready to run
- The bus will keep the batteries in working temperature, to ensure that the bus can be started directly when needed without pre-heating period
- 24 V batteries will be charged from 600 V battery
- Pre-heating/cooling of interior can be done when supported by HVAC supplier

Cooling system
- Coolant level warning in instrument cluster
- Automated control of battery temperature with active cooling/heating
- Electric driveline and auxiliaries cooling circuit
- No coolant filter

Climate system
- Chassis prepared for various roof-mounted HVAC units from different suppliers (heating, ventilation and air conditioning, including heat pump functionality)
- High-voltage heaters come pre-assembled on chassis (0–24 kW)

Tyres and rims
Steel and aluminium rims available

Rims	Tyres
7.5 x 22.5"	275/70 R22.5

Air and brake system
- Volvo disc brakes
- Electronic Braking System (EBS 5)
- Anti-lock Braking System (ABS)
- Acceleration Slip Regulation (ASR)
- Brake blending
- Hill Start Aid
- Brake temperature warning
- Poor brake performance warning
- Door brake
- Brake Assistant
- Lining wear sensing and analysis
- Automatic calibration after brake pad change
- Pneumatic system, easily filled from external circuit

Driver's station
Volvo dashboard or Limited dashboard, completed by body builder. Dashboard moves with the steering column in height and tilt (Volvo dashboard)
- Instrument cluster
  - speedometer
  - power meter
  - 4.3" display
  - SOC gauge
  - brake pressure gauge
  - indicators
  - warning lamps
- Tachograph
- Data logging
- Volvo Alcolock
- Outdoor temperature meter

Electrical system
Automatic shut off of main switch at low voltage level

Number of batteries
2 x 12 V

Battery capacity
2 x 105 Ah

VOLVO

Volvo Bus Corporation
volvobuses.com

Appendix 5 – AZURE PADRON Low Floor CityBus Higer Catalog

HIGER 海格客车 Electric Bus 100% Electric

TEVX Motors Group Ltda

AZURE PADRON- Bateria

AZURE PADRON Low Floor CityBus(Electric Version)	
Total dimension (mm)	12500*2530*3335
Wheelbase (mm)	5930
Wheel Track (mm)	Front 2103 / Rear 1833
Front / Rear Overhang (mm)	Front 2700 / Rear 3570
Approach / Departure Angle	≥8 / ≥7
Minimum Ground Clearance (mm)	≥370
Bus Interior Height (mm)	≥2100
Maximum Passenger Capacity	Seats 33, maximum capacity of 80 passengers
Total Running Weight / Front / Rear (kg)	1400
Maximum Allowable Bus Weight Total / Front / Rear (kg)	21000 (8.500/12.500)
Parking Capacity On Slope (%)	18%
Stopping Distance (m)	≤10 (Initial Speed 30km / h, Full Load)
Maximum speed (km / h)	≥80
Maximum speed in case of full load (km / h)	≥70
Ability to climb slope in case of full load (%)	≥20
Bus Autonomy (km)	250-270 KMS
Electric System	
Motor	
Brand and model	DANA TM4 SUMO HD
Type	Permanent Magnet Synchronous Motor
Position	Rear
Peak Power (kw)	370 Kw
Continuous Power KW	260 KW
Peak Torque Nm	3445 Nm
Continuous Torque Nm	1970 Nm
Max Operating Speed	3400 Rpm
Engine Weight	340 Kgs
Battery	
Brand	CATL
Battery Type	Lithium Iron Phosphate
Nominal Capacity (AH)	271
Nominal Voltage (V)	637.56
Working Voltage Range	495 ~ 722.7V
Density (wh / kg)	141
Pack Quantity	12
Storage Capacity (kWh)	385 Kwh
Battery Weight (kg)	1400
Site	7 Packs
Type of load	Plug
Warranty	8 years or 500,000km
Charge Station of 160 Kwh	less than 3 hours to recharge

BODY	
Air Conditioned	Valeo Air Conditioning CC 355- E REVO®-E 110.000 BTU/h (32 Kw)
Player	Hard Drive Player With Radio Function
Digital clock	With sample of temperature and humidity
WIFI Equipment	Equipped
USB Charging Interfaces	Equipped With USB Interfaces, Installed To Side Wall Next To Seats And Wheelchair Area
Monitoring system	Front Camera Of The Bus For The Streets Front And Medium Door Cameras Camera For Passenger Area (Equipped In The Central Interior Of The Roof To The Back) Reverse Camera With 500 G Memory Hard Drive
Megaphone	Equipped
Destination Sign	4 units, one front, one rear and one side on the right side
Reverse Buzzer	Equipped
Side Window Type	The Top With Sliding Window And Closed Back
Side And Rear Window Color	Light Gray, With Light Transmittance Between 50% - 70%
Driver Window Type And Color	Sliding Window, Transparent Color
Driver's seat	Grammer Air Suspension Seat With 3-Point Seat Belt
Passenger Seat	33 Urban Nylon Split Type Seats, 1 Wide Urban Seat, 1 Folding Seat In Wheelchair Area
Bus Interior Light	LED Lights With Two Rows
Front light	Round LED Split Headlights, Daytime Running Light
Rear headlight	Round LED Split Headlights, High Position Brake Light
Handrails And Bars	Aluminum Alloy, yellow Color
Bus Down Button	A Warning Light To Remind The Driver In Case There Is A Passenger Take The Down Button. On Each Vertical Bar Equip A Button. Special button for wheelchair area with different sound than others to remind the driver
Hatch	2 Units With Fan Function
Safety Hammer	Equipped Beside Side Window
Rear-view mirror	Electric
Doors	Front, Medium and Rear, With Two Door Doors, Open Inward ; Prevent Being Trapped By Passengers; The bus cannot be driven when the door is open; The door cannot be opened when the bus is in operation
Wheelchair Area	With Folding Seat, Handrail, Wheelchair Zone Symbol (Seat Belt Utility Introduction), Special Chime For Disabled To Get Off The Bus, USB Interfaces
Complete Separation For Driving Zone	With door
Floor	anti rolling lether old
Manual Plate for Wheelchair Disabled	Equipped In The Medium Door
Medicine Box	Equipped Behind The Driver Zone
Chassis Information	
Front Axle	ZF GERMAN
Rear axle	ZF GERMAN
Suspension	WABCO De Aire, Con ECAS
Corridor type	Low Floor Total
Direction system	Bosch
Steering Pump	Asistida Electrica
ABS	Wabco Disc Brake, Wabco EBS, ABS and ESC
Tires	295/80R22.5
Spare tire	No Hay
Brake Recovery System	SI - Equipado

DANA BOSCH ACTIA Prestolite SIEMENS WABCO MICHELIN CATL ZF Spheros Valeo kiel

TEVX – Motors Group Ltda – Official Distributor of Higer Bus Limited in Brazil
Av. das Américas, 3.434 - Bloco 5 - Grupo 520 - Barra da Tijuca, Rio de Janeiro – RJ – Brasil – www.tevx.com.br – comercial@tevx.com.br
Higer Bus Company Limited - 金龙联合汽车工业（苏州）有限公司 - Address: No. 288 Suhong Road Suzhou Industrial Park, Suzhou P.R.ChinaP.C.:215026 –
Tel: 0086 512 62584266 Fax: 0086 512 62582150 -中国 江苏省 苏州市 苏州工业园区 苏虹东路288

Appendix 6 – BYD D9W 20.410 Catalog

PRINCIPAIS CARACTERÍSTICAS:

- 100% elétrico;
- ZERO emissão de CO_2;
- Silencioso;
- Certificados ISO 9001/2015 e ISO 14001/2015;
- Baixo custo de manutenção;
- Até 250 km de autonomia*;
- 5 anos de garantia para o trem de força**;
- Credenciado no FINAME.

ESPECIFICAÇÕES TÉCNICAS

MOTOR	
Tipo	Motor síncrono de ímãs permanentes
Modelo	BYD - 2912TZ-XY-A
Potência máxima	2 x 150 kW (2 x 201 cv)
Potência nominal	2 x 110 kW (2 x 148 cv)
Torque máximo	2 x 550 Nm (2 x 56 kgf.m)
Torque nominal	2 x 400 Nm (2 x 41 kgf.m)
Rotação máxima	10.000 rpm
Relação de transmissão	Redução 1:22

SUSPENSÃO DIANTEIRA	
Tipo	Pneumática, com 2 bolsões de ar
Amortecedores	2 unidades
Barra estabilizadora	Sim

SUSPENSÃO TRASEIRA	
Tipo	Pneumática, com 4 bolsões de ar
Amortecedores	4 unidades
Barra estabilizadora	Sim

SISTEMA ELÉTRICO DE ALTA TENSÃO	
Modelo da bateria	BYD LiFePO4
Capacidade da bateria	344 kWh
Potência máxima de carregamento	DC até 160 kW (2 x 80kW)
Tomada para carregamento	CCS2 - Padrão europeu
Tempo de carregamento	2 a 3 horas
Tensão	380 V
Frequência de carregamento	60 Hz

EIXO DIANTEIRO	
Marca	ZF

EIXO TRASEIRO	
Marca	BYD

QUADRO DO CHASSI	
Tipo	Estrutura tubular em aço de alta resistência

SISTEMA DE DIREÇÃO	
Tipo	EHPS (Electric Hydraulic Power Steering)

SISTEMA DE FREIOS DE SERVIÇO	
Tipo	Freio a disco
ABS (sistema antitravamento)	Sim
EBS (sistema de controle eletrônico de frenagem)	Sim
Freio regenerativo	Sim

SISTEMA DE FREIO ESTACIONÁRIO	
Tipo	Câmara de mola acumuladora acionada pneumaticamente

RODAS E PNEUS	
Aros das rodas	8,25 x 22,5" em alumínio
Pneus	295/80 R22,5 (radiais, sem câmara)

PESOS ADMISSÍVEIS (PBT)	
Eixo dianteiro	7.500 kg
Eixo traseiro	13.000 kg
Total	20.500 kg

DESEMPENHO	Torque máximo (550 Nm x 2)	Torque nominal (400 Nm x 2)
Partida em rampa no PBT (Start Ability)	17%	11%
Subida em rampa no PBT (Grade Ability)	20%	15%

DIMENSÕES	
Comprimento (A)	12.265 mm
Balanço dianteiro (B)	2.590 mm
Entre eixos (C)	6.350 mm
Balanço traseiro (D)	3.330 mm
Altura estrutura (E)	3.070 mm
Largura estrutura (F)	2.320 mm
Ângulo de entrada (G)	8°
Ângulo de saída (H)	8°
Raio de giro	12.000 mm

Appendix 7 – Mercedes-Benz eO500 U 2134/59 Catalog

eO500 U 2134/59

Chassi elétrico 4x2 de entrada baixa para ônibus urbano

Dados Básicos

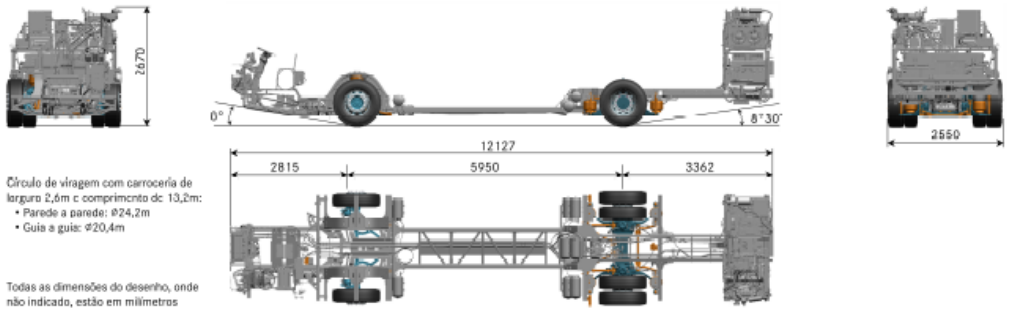

Círculo de viragem com carroceria de largura 2,6m e comprimento de 13,2m:
- Parede a parede: Ø24,2m
- Guia a guia: Ø20,4m

Todas as dimensões do desenho, onde não indicado, estão em milímetros

Carroceria *			
Comprimento encarroçado [m]	até 13,2		
Capacidade de passageiros	80		
Quantidade de assentos	27		
Pesos			
	Dianteiro	Traseiro	Total (PBT)
Cargas máximas por eixo [kg]	8.200	13.000	21.200

Trem de força

Motor Elétrico	
Modelo	ZF AVE 130, montados no eixo traseiro próximos aos cubos de roda
Potência de pico	250 kW (340 cv)
Torque máximo	2x 485 Nm (2x 49,4 mkgf)
Torque na roda	2x 11.000 Nm
Eixos	
Dianteiro	ZF 82 RL EC
Traseiro	ZF AVE 130
Desempenho	
Velocidade máxima	60 km/h (controlado eletronicamente)

Mercedes-Benz

Referência em Ônibus

Chassis

Suspensão	
Dianteira	Independente, pneumática, com 2 bolsas e barra estabilizadora
Traseira	Pneumática, com 4 bolsas e barra estabilizadora
Amortecedores	2x dianteiros, 4x traseiros
Suspensão com controle eletrônico e ajoelhamento bilateral - ECAS	Sim
Freios	
Freio de serviço	Disco
Indicador de desgaste das pastilhas	Sim
Sistema de gerenciamento eletrônico de frenagem - EBS	Sim
Frenagem regenerativa	Sim
Sistema anti-patinação - ASR	Sim
Freios auxiliares	
Antitravamento das rodas - ABS	Sim
Controle eletrônico de estabilidade - ESP	Sim
Sistema Elétrico de Alta Tensão	
Tensão nominal	665 V
Baterias tipo	Íons de lítio, NMC
Quantidade de pacotes de bateria	Configurável de 3 a 6
Energia nominal por pacote	98 kWh
Energia total	até 588 kWh
Carregamento	
Tipo de tomada	CCS tipo 2 - DC
Potência máxima	até 150 kW
Tempo	até 3 horas
Sistema Elétrico de Baixa Tensão	
Tensão nominal	24 V
Baterias	2 x 12V /100 Ah, livre de manutenção
Rodas e pneus	
Rodas de alumínio	9.00 x 22.5 no eixo dianteiro e 8.25 x 22.5 no eixo traseiro
Pneus	295/80 R

Posto de Condução

Computador de bordo	
Leitura direta	Velocidade, pressão dos circuitos de freio, carga da bateria
Informação de viagem	Distância, velocidade média, tempo de viagem
Luzes de advertência	Sim, em combinação com mensagens de falha
Telemetria	
Monitoramento das condições de funcionamento e localização	Sob consulta
Tacógrafo	
Modelo	Digital BVDR com impressora térmica
Sistema de direção	
Acionamento	Eletro-hidráulico
Coluna de direção regulável	Sim, altura e ângulo
Volante	de 4 raios, com teclas de navegação do computador de bordo
Climatização	
Sistema de ventilação e ar-condicionado com unidades condensadora e evaporadora de teto	Valeo "REVO 400"
Caixa de ventilação dianteira com desembaçador	Sim

Principais Opcionais

Opcionais **
Sistema de extinção de incêndio
Notas/Observações
* Consulte o encarroçador sobre o número de assentos e layout. O número total de passageiros mais o peso da carroceria não deve ultrapassar a capacidade de carga individual dos eixos. Valores correspondentes a configuração com 5 pacotes de bateria.
** Esta não é a lista completa de opcionais, consulte nosso pessoal de vendas para mais opções.

Julho 2022